QATAR UNIVERSITY

COLLEGE OF ENGINEERING

DEVELOPMENT OF HYBRID AND NON-HYBRID COMPOSITE BODY ARMOR

PLATE FOR BALLISTIC PROTECTION

BY

FARAH SAMIH ALKHATIB

A Thesis Submitted to the Faculty of

the College of Engineering

in Partial

Fulfillment of the

Requirements for

the Degree of

Masters of Science in Mechanical Engineering

January, 2017

The members of the Committee approve the Thesis of Farah S. Alkhatib defended on 9th of January 2017.

_____

Professor Elsadig Mahdi Saad

Thesis Supervisor

_____

Professor Abdelmagid Hammuda

Committee Member

_____

Dr. Mohammad Roshun Paurobally

Committee Member

_____

Professor Josep Costa

Committee Member

Approved:

_____

Khalifa Al-Khalifa, Dean, College of Engineering

ABSTRACT

Alkhatib, Farah, Masters: January: 2017, Master of Science in Mechanical Engineering

Title: Development of Hybrid and Non-Hybrid Composite Body Armor Plate for Ballistic Protection

Supervisor of Thesis: Professor Elsadig Mahdi Saad

In this work, a new Bullet Guiding Pocket Armor Plate (BGPAP) was developed, with a target to maximize the ballistic protection by containing the bullet between the layers. To this end, experimental and numerical programs have been carried out. Accordingly, the study has been divided into three phases concerning the problem solution to improve the energy absorption capability of the body armor plate without complete penetration. In phase-I, the effects of material stacking sequence and geometrical configuration on the ballistic behavior of hybrid and non-hybrid body armor plates were studied. Three different materials have been used, carbon fiber, Kevlar and date palm fiber. In phase-II, the effect of conical angles on the quasi-static crushing behavior of bullet guiding pockets was studied, in which five conical angles were tested, ranged between 35° and 55° with an increment of 5°. Two filament materials have been employed to fabricate the specimens. These are carbon fiber and Kevlar. The findings of the preceding phases were used as input for phase III, in which the new Bullet Guiding Pocket Armor Plate (BGPAP) has been developed. Finite Element software package, namely ANSYS/LS-DYNA has been used to simulate the ballistic behavior of tested body armors.

Material stacking sequence has affected significantly the energy dissipation mechanism, energy absorption capability of hybrid composite body armor. Body armor

with [CFRP$_{10}$/KFRP$_{30}$] material sequence displayed the highest energy absorption capability and passed the ballistic real shooting test. On the other hand, body armors with [CFRP$_4$/KFRP$_6$]$_4$ had displayed poor energy dissipation mechanism and didn't pass the ballistic real shooting. Incorporating the untreated date palm natural fiber composites in the material sequence of body armor displayed promising ballistic behavior, although didn't pass all the three-trial real shooting test. Introducing bullet guiding pockets in the design of body armors has a significantly effect on their sliding crush behavior. Similar sliding crush behavior trends have been observed for both CFRP and KFRP bullet guiding pockets have been found similar. Designing the bullet guiding pockets within the CFRP layers displayed the highest energy absorption capability compared with KFRP layers. Bullet guiding pocket conical angles has been optimized, and specimens with 50° had the highest specific energy absorption capability in both CFRP and KFRP. The newly developed BGPAP showed an excellent ballistic performance against 9 mm bullet with BFS 19.6 mm. The newly developed BGPAP showed 16% reduction in weight compared to the hybrid [CFRP$_{10}$/KFRP$_{30}$] armor plate.

Keywords: body armor, FEM, composite material, hybrid material, optimization, energy absorption, conical angle, tubes.

DEDICATION

This thesis is dedicated to the beloved people of mine.

To my mother, Manal, for her never ending care and advices especially now that I will become a mother myself.

To my father, Samih, the first man that encouraged me to chase my dreams and try for the best.

To my brother and sister, Zaid and Zain, who have trusted in my ambition.

And last but not least, to my partner in life, my dear husband, Othman. Very special thanks for your emotional support to the competing demands of our family, our study, and our personal development.

ACKNOLEDGMENT

This project was carried out in the Mechanical and Industrial Department of Qatar University. The author is grateful to the university and all faculty member who supported the project by their great ideas.

Table of Contents

List of Tables

List of Figures

CHAPTER 1

INTRODUCTION

1.0 Background

After World War II, the military and defense industries tended to develop the heavy and mobility-restricting body armors into more efficient protective structures. Nowadays, with the increase of terrorism attacks and wars; the need for high level of ballistic protection for military and defense sectors as well as the personal protection for law enforcement and corrections officers, has been one of the major challenges for engineers and researchers in the ballistic protection field against bullets and shrapnel [1, 2]. This is because wearing these body armors has played a considerable role in saving countless lives of armies and warriors in war fighting and counter terrorism operations. As stated by a study in 2003 in the Iraq war, they found that 58% of the wounds were in eyes, legs or hands, while 9% of the wounds were in torso [3]. In addition, body armors are widely used in peace keeping support missions and public security missions. Based on the statistical studies from international law enforcement agencies, ballistic resistant body armors have saved more than 3,000 police officers in the past years [4, 5]. However, deaths and disabilities from penetrating projectiles are not the main problems in ballistic-resistant soft body armors; the huge amount of energy delivered to the chest tissues by a non-penetrating projectile can cause fatal injuries, which is called the "Blunt trauma"[6-9].

At present, the military industry defines the term personnel armors as any protective clothing used to absorb impact energy resulted from gun fired or explosions, which includes; ballistic shields, vests that cover the torso, helmets that cover the skull, masks and goggles for face and eye protection [10]. The personnel armors are designed for small

caliber projectiles; fragments and bullets [11]. The level of ballistic protection for these armors is taken according to the kinetic energy received from the projectiles and can be stopped by the armor itself [12]. The National Institute of Justice (NIJ) has provided a fully described ballistic threats standards for each level of protection and the projectile type.

1.1 Problem Statement

The importance of body armors in saving lives, makes it a major subject for the military protection. The challenges for protective structure developers; are to ensure that their ballistic resistance product has a light weight, to provide the comfort during the soldiers' mission, at the same time, to ensure that these protection products can absorb the maximum energy delivered from shrapnel and bullets. Many parameters control the efficiency and function of composite body armor; such as the fiber ballistic property, the fiber structures (woven fabric, unidirectional filament), friction between the projectile and body armor, the bullet geometry and the projectile striking angle. Finding the optimum material and geometry for maximum energy absorption in body armor, to satisfy the previous requirements from comfort, weight and cost, and to obtain the maximum efficiency of the body armor are studied and analyzed in this research.

1.2 Objectives

The main objective of this research is to develop an optimum body armor plate by:

- Studying the ballistic behavior of material sequence and geometrical configuration on hybrid body armor plates.
- Studying the effect of conical angles on the quasi-static crushing behavior of bullet guiding pocket structures.

- Developing a new protective structure which combines between the material and geometry wise, with high energy absorption capability and high ballistic protection.

1.3   Significance of the Study

Currently, finding the optimum geometry and material for comfort, lightweight and maximum energy absorption body armor is challenging [13, 14]. Most studies are looking at the material side for designing new ballistic plates; as an example, reducing the thickness of Ceramic or Kevlar layers in Ceramic Ballistic Plates with same level of protection is an effective solution for having a lightweight body armor [15]. Also, hybrid composite body armors are widely used under ballistic impacts. On the other hand, the physical design is taking a place in new researches, introducing new small scale energy absorption devices as a core in the armor plates forming sandwich panels is a new promising technique in the ballistic field [16-22]. Most of these energy absorbing devices are considered as thin-walled tubes with various geometries, dimensions and material properties. Their high strength-to-weight ratio and energy absorption capability make them suitable for impact resistance. Filling the gap in this field was one of the main reasons behind this research.

1.4   Thesis Layout

This thesis contains five chapters including this chapter, which introduces the background of the research, defines the problem, objectives, and significance of this study. Chapter 2 focuses on literature review related to the armor systems and their development through the history. Some of the new improved techniques and researches are introduced in Chapter 2 as well. Chapter 3 contains the methodology used to carry out the study. The first section covers the fabrication process and the experimental testing techniques. The second section represents the finite element modelling program used to optimize the geometry and

materials used for body armor plate. The results of the effect of conical angle, sequence, material types and other parameters are presented and discussed in Chapter 4. Finally, a conclusion is presented in Chapter 5 with some recommendations for future research.

CHAPTER 2

LITERATURE REVIEW

In this chapter, a literature review for the body armor systems and their development are presented. Classifications and types of current body armors with the testing standards and testing methods are discussed. Some of the new improved techniques and researches are also highlighted.

The ballistic performance evaluation of body armor is discussed through the following aspects; (1) energy absorption based on kinetic energy, (2) V_0 and V_{50} ballistic tests, (3) ballistic evaluation based on back face signature (BFS). Then the factors affecting the body armors function are mentioned with some previous work for many authors. The fabrication processes in producing composite body armors are mentioned. Finally, the mechanics of composite materials and composite failure theories are presented.

2.1   Introduction

A personnel body armor is defined in the literature as any protective clothing for absorbing impact energy resulting from gun fire or explosions. This includes; ballistic shields, vests that cover the torso, helmets that cover the skull, masks and goggles for face and eye protection [10, 23]. The military body armors are designed to protect from high velocity projectiles like fragments and rifle bullets. While police body armors provide protection from low velocity handgun bullets and sharp weapons [11, 24]. Thus, these armors should be designed consistent with the protection level needed, to provide an easy movement for the person.

2.2 Ballistic Protection

2.2.1 Body armors through history

Throughout history, humans have used various types of body armors to protect himself from weather conditions, injuries or other dangerous conditions; starting from leather skins of animals, through the wooden, metallic shields and the flak jackets of World War II, to today's high-tech polymer-matrix composite body armor plates and vests [25]. Nowadays, military and civil protection has been one of the major challenges for engineers and researchers in the ballistic protection field against bullets and shrapnel [11, 26]. Bulletproof term is not usually used in military industry, because this indicates that the bulletproof will protect against any type of threats. Thus, bullet resistant or ballistic protection is generally preferred.

Historically, the Roman Empire was involved in many battles and wars. therefore, romans designed their own protective clothes. They covered their torso, legs and arms with overlapping pieces of iron strips that are fastened with leather hooks (Figure 2-1-a). The helmets were made from iron or copper, the back of the helmet had a guard to protect the neck from the sword blows. It has been estimated that a soldier could wear from 30-45 kg of the protective uniform. In 15th Century, a new armor appeared in Italy. It was called Knights Armor (Medieval Armor) (Figure 2-1-b). Medieval Armors were very useful and effective for that time weapons (Swords, axes & arrows), but at the same time they were too heavy (approx. 50 kg) and non-flexible as they were made of Steel [25]. Trying to solve non-flexibility problem in the past body armors, Japanese people created Samurai Armor (Gusoku) in the sixteenths (Figure 2-1-c), which consist of multiple pieces of bamboo, leather and metal sheets, it provided more flexibility but it was still heavy (25-30 kg) [25,

27]. In 1860s, the first soft ballistic vest was created in Korea, it was made of 30 layers of cotton which called it "Myeonje Baegab" (Figure 2-1-d), it was lighter in weight but didn't provide an effective level of protection [25].

During the World War I (1914-1918), the United States of America has developed a Chrome Nickel Steel Shield (Figure 2-2-a), it consisted of two parts; breast armor and head piece. This protective shield was about 18 kg of weight, which made it very heavy and mobility-restricting shield. On the other hand, it could resist Lewis Gun bullets at 820 m/s [28]. While in World War II (1939-1945), infantrymen used to wear heavy steel body armor shields which were incompatible with their missions. So the United States military
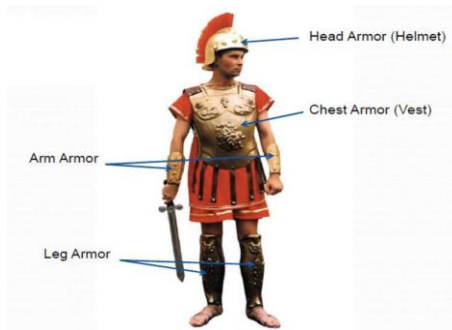
(a) B.C Roman armor [25]

(b) Knight armor (Medieval Armor) [25]

(c) Samurai armor (Gusoku) [25]

(d) Myeonje Baegab [25]

Figure 2-1: Past body armors.

tried to develop ballistic vests for their army made from woven nylon, these vests had a good improvement in weight reduction but unfortunately they were not fully efficient in stopping bullets, although the army claimed that these vests can stop a 7.62×25 mm Tokarev pistol bullets [26, 29]. In 1967, Natick Laboratories has introduced T65-2 plate carriers (Figure 2-2-b) for holding hard ceramic plates. These body armors were able to stop 7 mm rifle rounds [26]. In mid-seventies, DuPont Company has introduced Kevlar® fibers to the market. In 1976, Second Chance Company was the first one to manufacture all-Kevlar® vests. Those vests were light and concealable, therefore, the police officers used to wear it daily [30]. During 1980s, the US army used the PASGT Kevlar® vest (Personal Armor System for Ground Troops) (Figure 2-2-c), which weighted around 11 kg and was able to resist 9 mm FMJ bullets [31]. Nowadays, the body armors comprise two parts; soft and hard. The soft body armor is simply the vest that covers the torso which can be worn easily and comes with different sizes. It is made from high-performance lightweight synthetic polymer fibers that show a great ballistic resistance, due to their high stiffness and high tenacity [32]. The textiles that are used to manufacture the soft body armor include; aramids; Kevlar®, Technora®, Twaron®, highly oriented ultra-high molecular weight polyethylene (UHMWPE); Dyneema®, Spectra®, and p-phenylene-2-6-benzobisoxazole, polyamide (PBO); Nylon® [26]. Soft body armors provide the basic level of protection from low velocity handgun bullets, to resist the high velocity rifle bullets; hard plates are used and can be inserted inside the plate carrier of the vest (Figure 2-2-d). These plates can protect up to level IV, as per NIJ standard. The hard plates are usually ceramic-faced and composite-backed; alumina /aramid or totally made of composite; Kevlar®/epoxy [24, 33-36]. Designing lighter weights and higher energy absorption

capabilities under impact loads; new improved materials or systems are still under research. As a new promising technology; small scale energy absorption devices are inserted as a core in the armor plates forming sandwich panels. Currently, researchers are developing these energy absorption devices [16-21].

(a) Chrome Nickel Steel Brewster Body Shield [28]

(b) T65-2 plate carrier [26]

(c) PASGT Kevlar® vest [31]

(d) Heart Dyneema® plate & ballistic tactical vest [23]

Figure 2-2: Past and recent body armors

2.2.2 Body armor classification

Current body armors are classified into many classifications; depending on the applications, materials or threats. Some types are mentioned with brief description below. Table 2-1and Table 2-2 summarize the types of body armors by application and material.

2.2.2.1   Combat body armor (CBA)

Combat Body Armor (CBA) was introduced by the UK Ministry of Defense in 1991 [37-39]. CBA is designed for torso protection, which is made from many layers of plain woven nylon 6,6 and aramid fabrics, it has a waterproof cover to prevent water and ultraviolet radiation. CBA has two plate carriers in the front and rear of the vest. Ceramic-composite plates can be inserted in these carriers for high level of protection. Later on, the UK military medical community has determined the exact position of the plate to protect the heart, by introducing the Enhanced Combat Body Armor (ECBA) (Figure 2-3) [39, 40]. ECBA was first introduced in Northern Ireland and had a weight of less than 5 kg for a medium size; while ECBA plate was around 1.1 kg.

2.2.2.2   Osprey body armor system

In 2005, the UK Ministry of Defense has designed new body armor system to use in Iraq and Afghanistan [41], to provide a higher level of protection than ECBA. They called it osprey body armor system (Figure 2-4-a). Osprey has a tabard style for torso protection, it is made of many layers of water-repellent-treated (WRT) aramid fabrics. Also, it has a waterproof cover to prevent water and ultraviolet radiation. There are plate carriers in the front and back of the Osprey vest. Osprey plates (Figure 2-4-b) are more than twice the area of ECBA, these plates can provide a protection for the heart, mediastinum, spleen and liver from high velocity rifle bullets. Each Osprey plate weighs around 3 kg [23, 41].

2.2.2.3   Interceptor Body Armor (IBA)

As mentioned before, the US army used the PASGT Kevlar® vest (Figure 2-2-c) during 1980s [31]. Between 1990s and 2000s, they developed PASGT armor system into lighter

(a) ECBA (position of plate highlighted) [23]   (b) ECBA plates [23]

Figure 2-3: Combat Body Armor (CBA).

(a) Osprey body armor Mk1 [23]   (b) Osprey front and back plate [23]

Figure 2-4: Osprey body armor system

and more protective armor system which is called Interceptor Body Armor (IBA) (Figure 2-5). It consists of an Outer tactical vest (OTV) (Figure 2-5-c) which is made of Kevlar® and has four plate carries; front, back and sides. ESAPI ballistic plates (Enhanced Small Arms Protective Insert) (Figure 2-5-a) are inserted inside the vest carriers. ESAPI are made of boron carbide or silicon carbide ceramic. Enhanced Side Ballistic Inserts are inserted in the sides of the vest (Figure 2-5-d). Deltoid and Axillary Protectors (DAP) are worn on the shoulders (Figure 2-5-b) [42]. The USSOCOM (United States Special Operations Command) has developed a body armor vest that can be released quickly to use it in

emergency cases which is called the Releasable Body Armor Vest (Figure 2-6). This vest has 2 torso plates, 2 shoulder plates, 2 side plates and a groin plate. Table 2-1 summarizes the types of body armors based on their application; war fighting, public security, and covert security. On the other hand, Table 2-2 summarizes the types of body armors based on material used; textile, composite and ceramic.
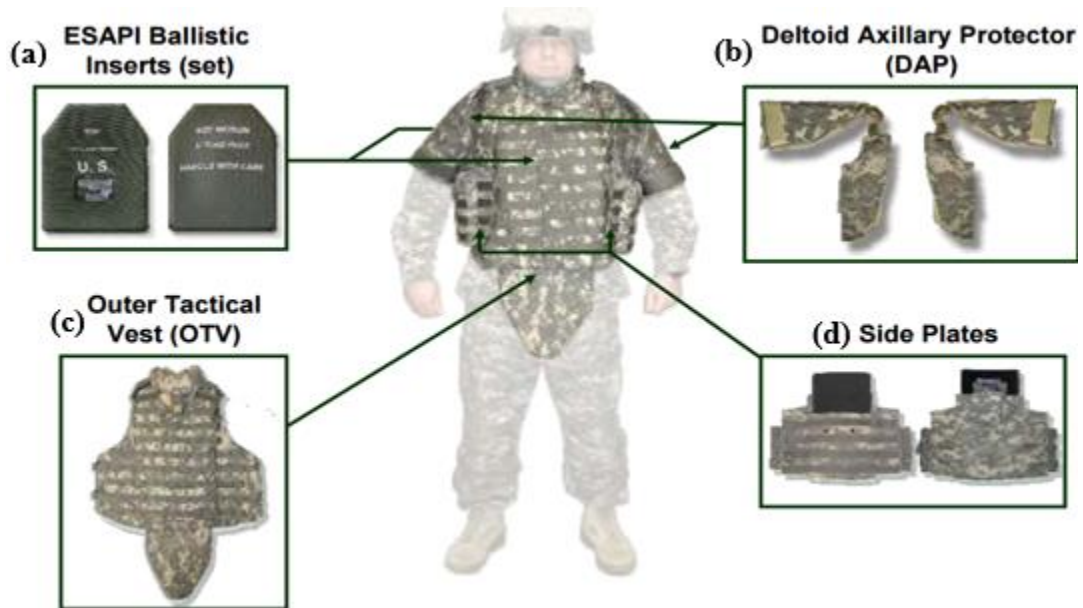
Figure 2-5: Interceptor body armor [42].

Figure 2-6: Releasable body armor vest

Table 2-1: Types of body armors by application

Application	Armor type	Protection level	Material
War fighting	Combat Body Armor (CBA)	• Fragments • High-velocity bullets	Aramid vest + Plate
	Osprey body armor system	• Fragments • High-velocity bullets	Aramid vest + Plate
	Interceptor Body Armor (IBA)	• Fragments • High-velocity bullets	Kevlar vest + Plate
Public security	Police firearms	• Large Handguns • High-velocity bullets	Textile + Plate
	Police routine patrol	• Small Handguns • Knives	Special Textile
Covert Security	VIP and close protection	• Small Handguns • Knives	Special Textile

Table 2-2: Types of body armors by material

Armor material	Protection level	Construction	Advantages	Disadvantages
Textile body armor	• Handgun bullets • bomb fragments (depends on number of layers & type of fibers)	• Multiple layers (20-100) of high strength textile • Various fibers (Kevlar®, Twaron®, …)	Flexible & lightweight for torso	Not sufficiently flexible for limbs (Comfort is decreased by increasing coverage)
Composite body armor	• Assault weapons • Shotguns	Rigid plates of fiber bonded in a resin	Rigid cover for torso	heavy and thick
Ceramic body armor	• High velocity rifle • Bomb fragments	Ceramic tiles on composite backing	• Rigid cover for torso • Less thick	Heavy

2.3 Energy Absorption Devices Inserted in Body Armor Plates

In present days, introducing new materials, techniques and designs of body armors will lead to better protection and reduction in weights of these armors. New blast protection structures are manufactured in the form of sandwiches; which have been known for several

14

decades with their excellent energy absorbing capabilities [43-46]. A sandwich structure consists of a light-weight core material and two cover sheets, one at the front and one at the back face of the core. Some core materials are not from bulk materials; it is designed with different geometries and structures for more energy absorbing capability and significant weight savings. These small-scale structures are called energy absorber devices.

As defined by Alghamdi [47], the energy absorber device can be any system or structure that converts the kinetic energy received into any other form of energy or deformation. While E. Mahdi and Hamouda [48] have classified the energy absorber devices into plastic and fracture energy absorber devices, depending on the materials used in the structures; metal based or composite based. Johnson *et al.* [49] have summarized the main factors that control the plastic deformation; the displacement patterns, Load description, application patterns and Properties of materials involved. There are many types and geometries of energy absorber devices that are studied in the literature; square/rectangular tubes [50-53], circular tubes [18, 54-56], hexagonal/octagonal tubes [57-59], conical tubes [60, 61], elliptical tubes [62], spheres [22], honeycomb cells [19, 20, 63, 64], and sandwich panels [43-46]. Overall, the main objective from these energy absorber devices is to provide the safety of high priority systems like vehicles and blast protection structures, by protecting them from damages resulted from kinetic energy and preventing the sudden impacts.

Palanivelu *et al.* [65-70] had studied experimentally and numerically the energy absorption capability of different geometrical E-glass/polyester structures under quasi-static and dynamic loading conditions. The main aim from these studies was to compare between these different geometries and exclude the structures that have less energy absorption capability in their sacrificial cladding application. This sacrificial cladding structure

consists of two layers; the outer skin for distributing the blast pressure and the inner core which deforms in a progressive manner to minimize the impact energy [71-73]. The energy absorber devices are introduced in the core layer with different configurations.
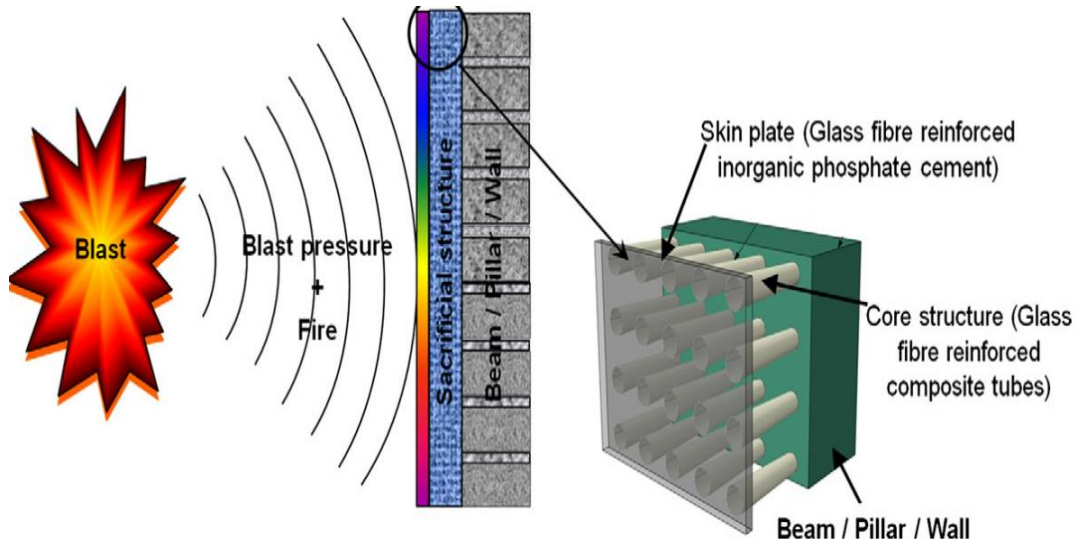
Figure 2-7: Concept of sacrificial cladding structure [44].

| (a)
square | (b)
circular | (c)
hexago
n | (d)
hourgla
ss-A | (e)
hourgla
ss-B | (f)
hourgla
ss-X | (g)
hourgla
ss-Y | (h)
cone-X | (i)
cone-Y |
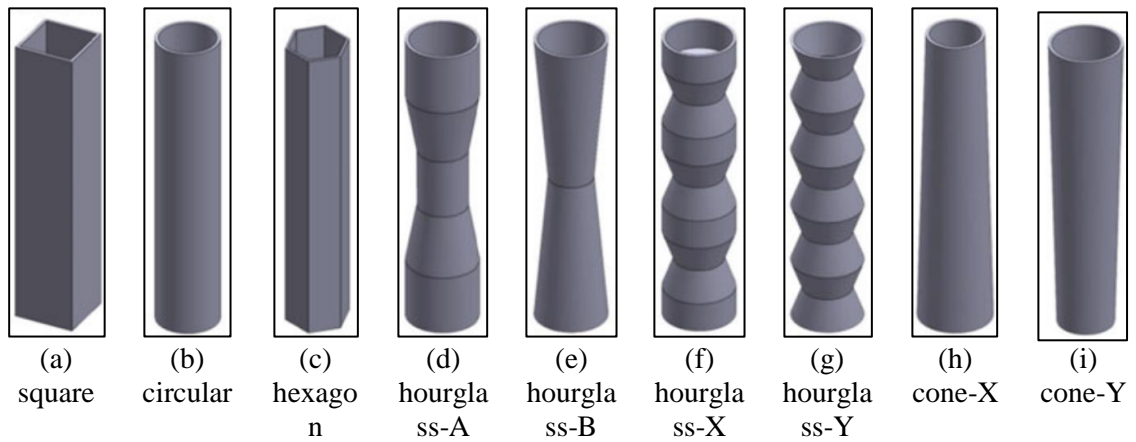
Figure 2-8: Schematic for the E-glass/polyester tubes [44, 65-70].

2.3.1   Crashworthiness parameters

To evaluate the crashworthiness of any energy absorber device, some parameters are studied and analyzed, which are listed as the following:

1. Peak load (P_p)

   P_p is obtained from the load–displacement curve directly, which is the first peak in the load–displacement curve.

2. Critical initial crushing load ($P_{i,cri}$)

   $P_{i,cri}$ is obtained from the load–displacement curve directly, which is the first critical peak in the curve.

3. Mean-crushing load (P_m)

   P_m is the average crushing load, which is obtained by taking the average of the crushing loads in the post-crushing region.

4. Crush force efficiency (CFE)

   CFE is the ratio between P_m and P_i. as shown in Equation (2.1):

$$CFE = \frac{P_m}{P_i}$$

(2.1)

5. Energy Absorbed (EA)

   The energy absorbed by the crushed composite specimens is the area under the load–displacement curve, as shown in Equation (2.2):

$$EA = \int_0^{S_f} P ds$$

(2.2)

6. Specific energy absorption (SEA)

SEA is the energy absorbed per unit mass of material. The energy absorbed by the crushed composite specimens is the area under the load–displacement curve, in other words, the integration of load–displacement curve, Equation (2.3).

$$SEA = \frac{\int_0^{S_f} P ds}{M} \qquad (2.3)$$

Where [0 and S_f] is the crushing distance, M is the mass of structure that have been investigated.

2.4 Ballistic Performance Evaluation

2.4.1 Energy absorption based on kinetic energy

The most common way to calculate the ballistic performance of body armor is to calculate the kinetic energy absorbed by the plate [74-77] as shown in Equation (2.4):

$$KE = \frac{1}{2} m (v_s^2 - v_r^2) \qquad (2.4)$$

Where m is the mass of the projectile, v_s is the projectile's striking velocity and v_r is the projectile's residual velocity

2.4.2 Ballistic Testing (V_0 and V_{50})

Zero penetration velocity (V_0) is a ballistic test that uses the bullet's kinetic energy, Equation (2.4), as a key factor and the velocity of the bullet (v) as a primary independent variable. In V_0 test, a bullet with constant velocity is fired towards the sample. After that, the velocity at which the sample will not be penetrated by the bullet is determined.

As V_0 test is difficult to measure, another testing concept has been developed in ballistic testing called the ballistic limit V_{50}. In this test the velocity at which 50% of the shots completely penetrates the armor and 50% of the shots partially penetrates the armor is determined [78]. A Ballistic Performance Indicator (BPI), was developed by Figucia [79], which measures the ballistic performance of the fabric and compares these results with the actual V_{50} values.

2.4.3 Ballistic performance evaluation based on back face signature (BFS)

Around the world many ammunition types and sizes are available. Due to this, body armor testing standards are regional so it reflects the threats found locally. In 1979, the Office of Science and Technology of the National Institute of Justice (NIJ), U.S. Department of Justice, has sponsored the Law Enforcement and Corrections Standards and Testing Program to improve and develop a performance standard for testing the body armors, in order to fulfill the needs of the criminal justice system nationally and internationally [80]. Recently, the Office of Law Enforcement Standards (OLES) of the National Institute of Standards and Technology (NIST) has developed NIJ Ballistic Resistance Standard, "Ballistic Resistance of Personal Body Armor". This standard is a technical document which assigns the essential performance requirements of the personal body armors. In this standard, a full description of the testing procedures required to test and approve any personal body armor is explained in details.

NIJ Standard-0101.06 is the latest updated version of NIJ Ballistic Resistance Standards, which has classified the personal body armors into five types (IIA, II, IIIA, III, IV) based on the level of ballistic protection. And a special test class for threats that are not covered by the previous five types (Appendix G). The ballistic threat from any bullet depends on

many parameters; bullet's shape, mass, composition, caliber, impact velocity and angle of incidence. Due to the wide variety of bullets available in the same caliber, body armors that pass the standard test round may not resist other loadings in the same caliber with higher impact velocity or different configuration [80]. Figure 2-9 shows the ballistic test setup.
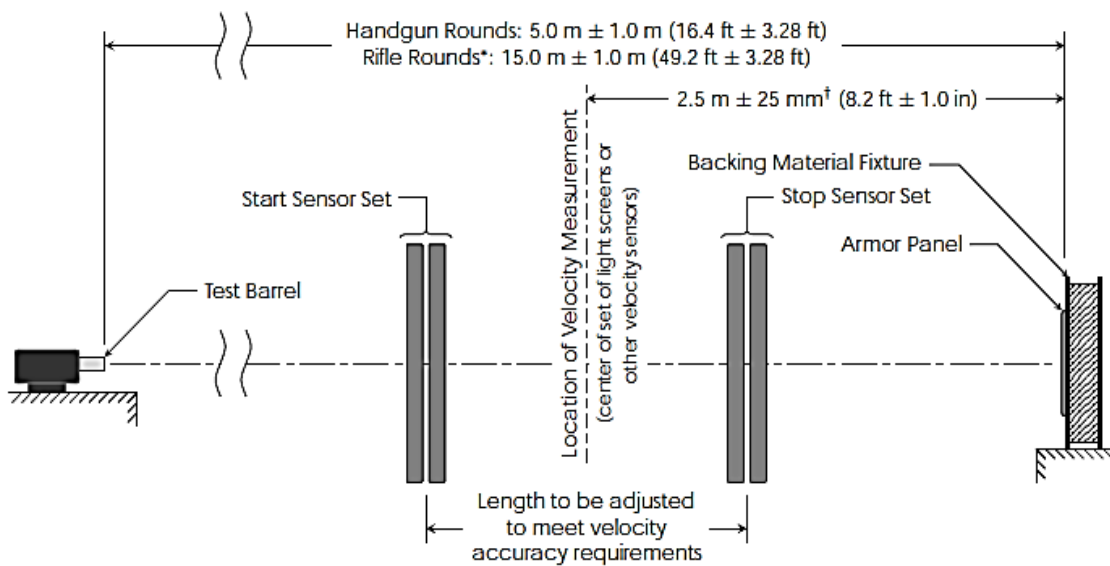
Figure 2-9: Ballistic test setup for NIJ test [80].

Ballistic testing is a way to check the resistance of body armor to penetration. Ballistic testing is a destructive test but it does not measure the stresses on sample or energy absorbed by the sample; it only measures the acceptable number of partial and complete penetrations, and the depth of the back-face Signature (BFS) for partial penetration of the body armor which should not exceed an acceptable limit. These two parameters are called the performance specifications or the Contact Purchase Description (COPD). The way of knowing a partial or complete penetration, is by placing a clay backing material behind the

armor plate, once the bullet passes into the clay that means complete penetration occurred. And if the bullet penetrates the armor plate partially, the depth of the bulge created on the clay will be measured and should not exceed 44 mm according to NIJ ballistic resistance standard (Figure 2-10) [80].

The backing clay material is also called "Roma Plastilena", this clay is roughly twice the density of human tissue, therefore it does not match the human's specific gravity. For accurate BFS measuring, this clay is a plastic material that will not recover its shape elastically [81].
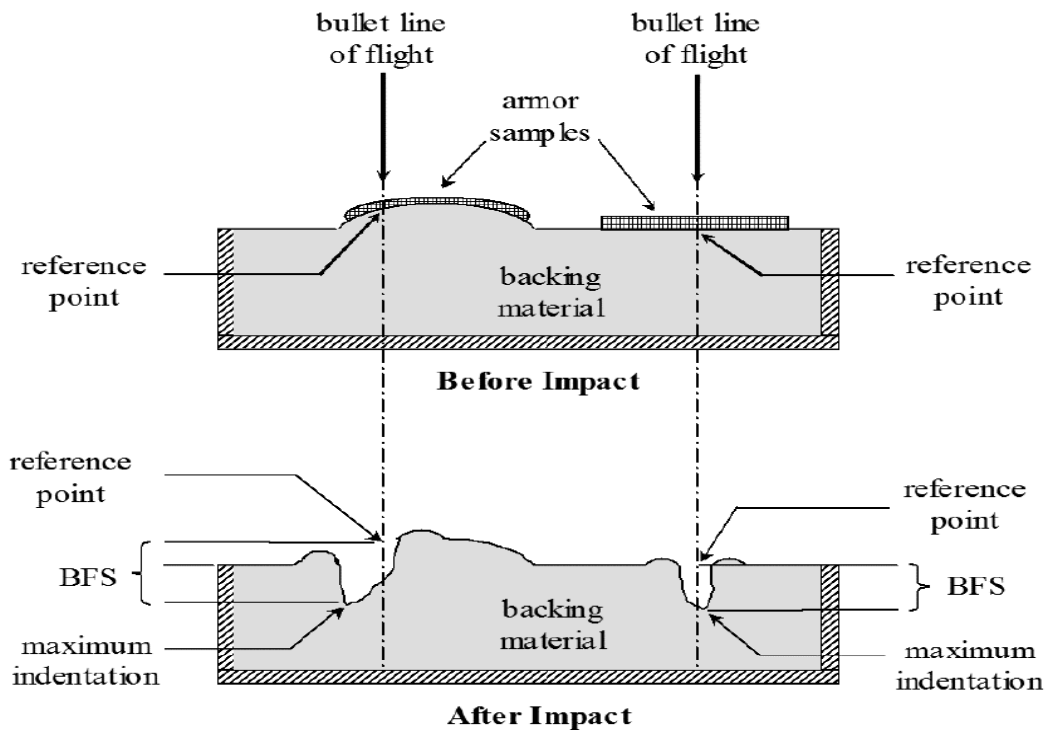
Figure 2-10: Measuring back-face signature (BFS) according to NIJ [80].

2.5   Factors Affecting Composite Body Armor Performance

Many authors have mentioned the factors that affect the composite body armor performance [82, 83]. These factors are related to each other, so it is difficult to separate between them. In this section, some factors will be discussed in details.

2.5.1   Fiber ballistic properties

The fiber ballistic performance depends on many parameters. For example, if the fiber ballistic performance depends on fiber tensile strength, then Nylon will behave better than Kevlar in arresting the bullet. But in fact, Kevlar has shown the highest performance fiber in soft and hard body armors [84]. Cunniff [85] has shown in his work that the ballistic property of fibers is a function of many parameters; velocity of sound in a fiber and the material density, where the fiber ballistic property in m^3/s^3 (U^*) is the product of fiber specific toughness $\left(\frac{\sigma\varepsilon}{2\rho}\right)$ and strain wave velocity $\left(c = \sqrt{\frac{E}{\rho}}\right)$, as shown in Equation (2.5):

$$U^* = \frac{\sigma\varepsilon}{2\rho}\sqrt{\frac{E}{\rho}} \qquad (2.5)$$

σ is the fiber ultimate tensile strength, ε is rupture strain, E is the fiber Young's modulus, ρ is the fiber mass density. On the other hand, Roylance and Wang [86] have found that half of the total energy absorption by the ballistic body armor is stored as strain energy. They also found that the fiber with higher Young's modulus gives higher wave velocity, which means a rapid energy absorption rate. While when the fiber's Young's modulus is decreased, the wave velocity is decreased and the strain is more concentrated in the impact zone, as shown in Figure 2-11, graphite has high Young's modulus but it was not able to extract energy as Kevlar or Nylon which have low Young's modulus.
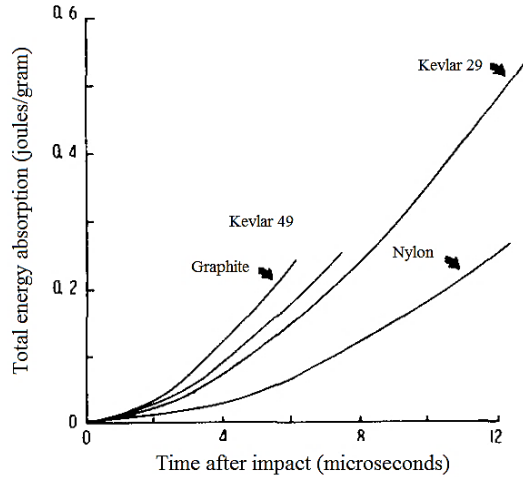
Figure 2-11: Comparison of total energy absorption for different fabrics [86]

2.5.2 Fiber structure (woven, unidirectional)

Soft body armors are usually made of woven fabrics, which have the abilities to stop the bullets by making a network around the bullet. This network transmits the bullet's kinetic energy through the fibers [87]. In woven fabrics, a cover factor which is known as "weave density of fabric" defines the number of warp (ends) and weft (picks) in a unit of length of fabric (Figure 2-12-a), it indicates the percentage area covered by the fabric.

(a) Warp (ends) and weft (picks) in a unit of length of fabric

(b) Different weave density of fabric
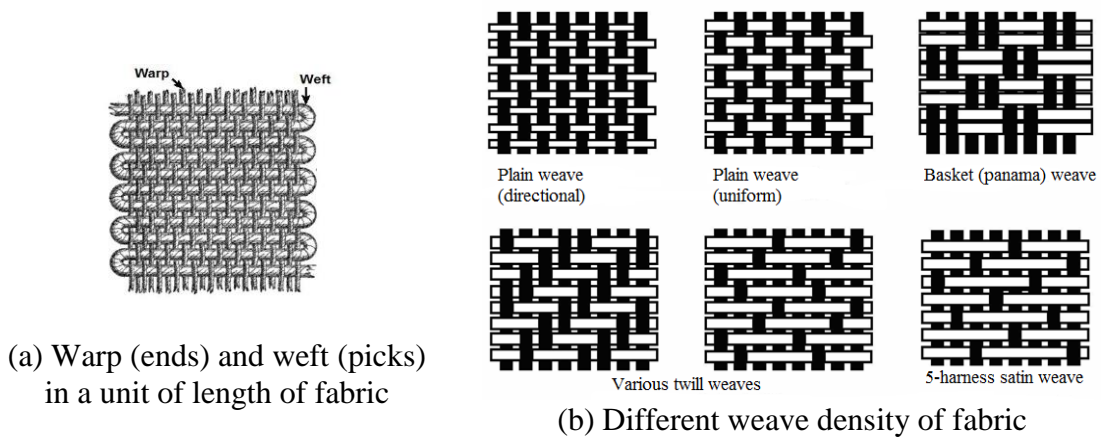
Figure 2-12: Fiber structure

High weave density of fabric will increase the strain energy capability dissipated through the fabric by involving more fibers with the projectile arresting, This study was carried out by Shockey *et al* [74], which studied the Zylon fabrics with different weave densities. They concluded that the weave density for ballistic application should be between 0.6 and 0.95. As more than 0.9 weave density, the fabric will decrease the function of fibers in arresting the projectile, and a weave density below 0.6 will make the fabric too loose to arrest the projectile. In case of unidirectional filaments, it is not widely used for ballistic protection, because of the duration of fiber stretching which causes blunt trauma under the impact zone [14]. Lee *et al* [88] have studied the angled ply laminates for ballistic protection, they found that 100% unidirectional panel can absorb 12.5% to 16.5% more energy than 100% of woven panel under same conditions.

2.5.3   Friction between the projectile and fabric

Friction is divided into two frictional mechanisms; friction between the projectile and fabric, and the friction between fabric layers inside the body armor itself. The frictional energy is related to many factors; like boundary conditions and yarn-yarn coefficient of friction [83]. The response of fiber-reinforced and dray woven fabric armors under ballistic impacts was studied by Lee *et al* [89]. They found that the failure of fiber-reinforced composite armor is due to fiber fracture, this is because the existence of the matrix. While in dry woven fabric armor, the fracture happens because of yarn slippage. From these observations, they concluded that the energy absorbed by the composite armor is more than that absorbed by the dry woven fabric armor. Yarn-yarn coefficient of friction was studied numerically by Zeng *et al* [90], they increased the yarn-yarn coefficient of friction (μ) from 0 to 0.1, and concluded that the ballistic limit of the fabrics were doubled. This work was

totally opposed to Briscoe *et a* 's work [91], which have treated Kevlar 29 chemically by soxhlet-extraction and polydimethylsiloxane (PDMS). Results showed that soxhlet-extracted fabric had a 0.25 coefficient of friction value, while PDMS treated fabric had a 0.18 coefficient of friction value. Thus, increasing the yarn-yarn frictional coefficient will improve the energy absorbed by the ballistic fabric. Chemical treatment is commonly used for increasing the yarn-yarn frictional coefficient is the shear thickening method. The concept is about increasing the fabric viscosity with the increase of shear rate [7, 92-94].

2.5.4   Bullet geometry

Bullet geometry plays a big role in penetrating the body armor, thus it affects the energy absorbed by the body armor. Figure 2-13 shows four different projectiles studied by Tan *et al* [95]. In this study, they investigated the energy absorbed by Twaron CT 716 woven fabric. They concluded that the sharp noses projectiles (ogival and conical), resulted to less energy absorption than hemispherical and flat projectiles, as shown in Figure 2-14. This is because ogival and conical projectiles (sharp noses projectiles) slip through the fabric yarns which causes less energy absorption. While in hemispherical projectile, it penetrates the fabric by stretching its yarns. In flat projectile, the geometry has an angled edge which causes shearing for the yarns during penetration.
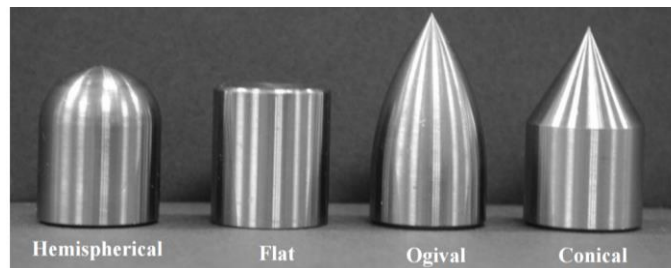
Figure 2-13: Different projectile geometries [95]
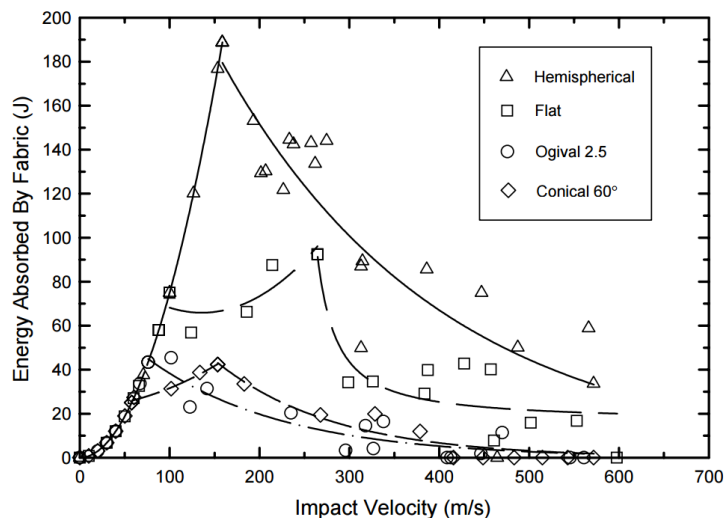
Figure 2-14: Energy absorbed by impacted Twaron CT 716 woven fabric for different projectile geometries [95]

2.5.5 Projectile striking obliquity

Projectile striking obliquity is the angle at which the projectile hits the body armor as shown in Figure 2-15. Shockey *et al* [74] have concluded from their study that the striking angle is dependent on the projectile dimensions. So, if the length of the projectile is equal to the diameter of the projectile's head, then the angle of obliquity has less effect on the energy absorbed by the ballistic plate. likely to affect the energy absorption of ballistic fabrics.
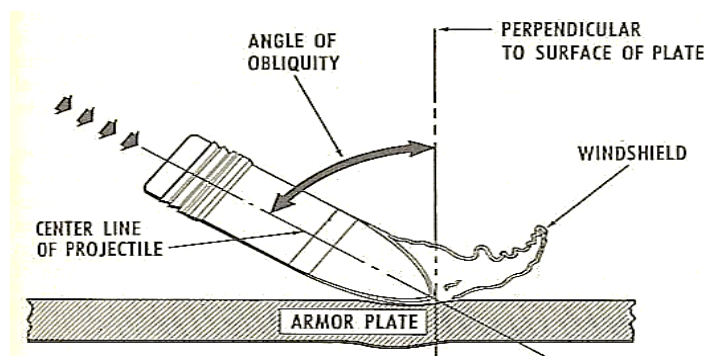
Figure 2-15: Projectile striking obliquity

2.6   Fabrication Processes of Composite Materials

2.6.1   Vacuum infusion process

Vacuum infusion process is a closed mold fabrication process, that uses the pressure difference technique to infuse the resin through the reinforcement. Dry reinforcements are arranged in the proper required sequence over the mold and covered by bagging materials. Vacuum is applied to the system before resin is introduced. Once the vacuum is completed, the resin inlet is opened to drive the resin through the laminates [96]. Vacuum infusion is better fiber-to-resin ratio than hand lay-up process with a high-quality surface finishing and high strength parts. At the same time, less wasted resin is used, thus it is a cost-effective process. On the other hand, Vacuum infusion is a slow manufacturing process, so it is not recommended for mass productions [97]. The vacuum infusion process set-up, equipment and mold preparations are shown in Figure 2-16 and Figure 2-17.
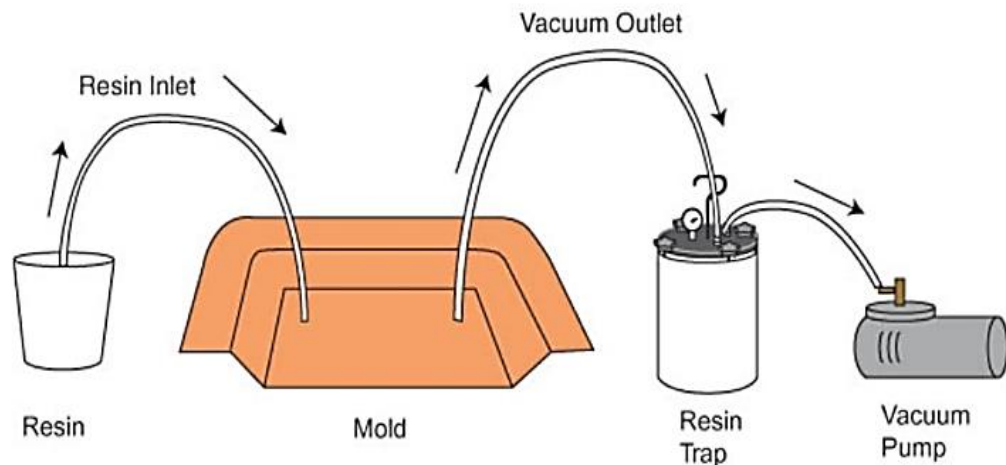
Figure 2-16: Vacuum infusion process [98]
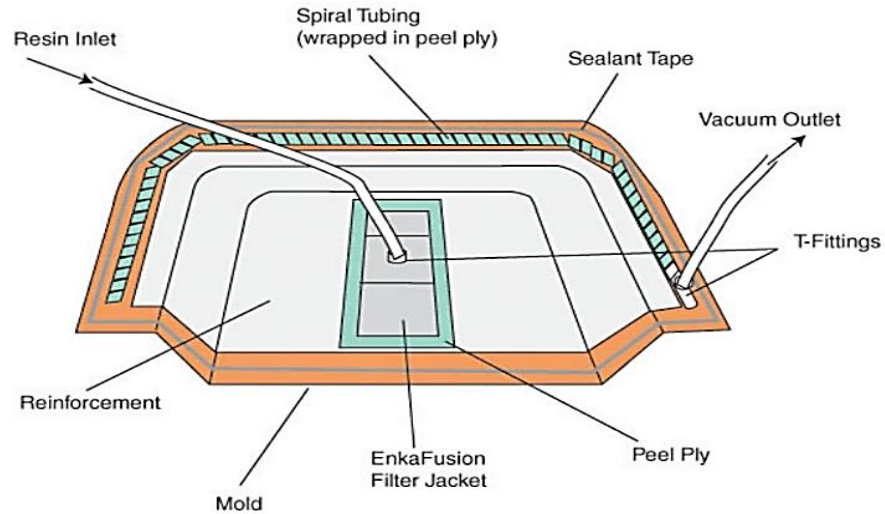
Figure 2-17: Vacuum infusion mold preparation [98]

2.6.2 Filament winding process

Filament winding is a fabrication process that uses a continuous band of fibers, that are pre-immersed in resin. These fibers are rolled around a rotating mandrel with a chosen angle to create axisymmetric hollow composite geometries. Filament winding is used widely in industry; pipelines, drive shafts, pressure vessels, aircraft fuselage, storage tanks…etc [99, 100]. Figure 2-18 shows a basic filament winding process scheme.
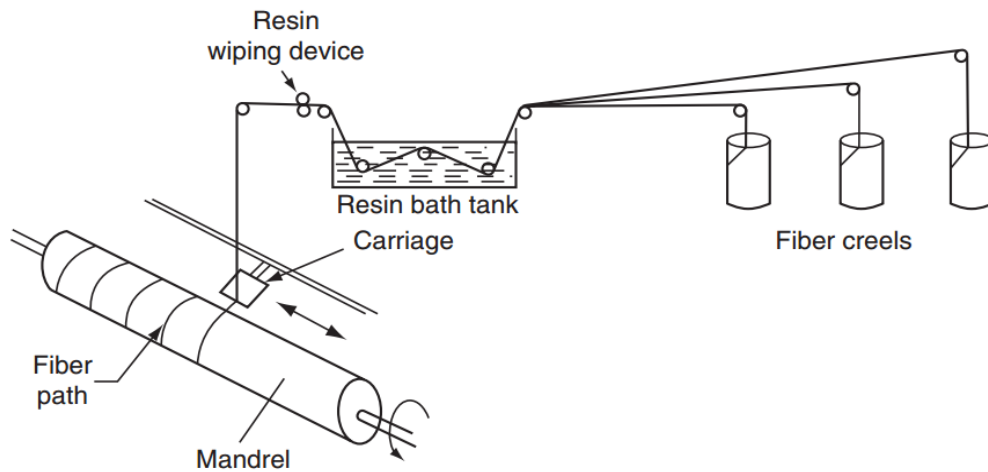
Figure 2-18: Filament winding process [99]

Filament winding provides a highly reliable and low cost parts, as the whole part can be fabricated easily from continuous fibers without using any joints. This process is suitable for mass productions, because less labor can be used, no bagging materials are used and no wasted resin. Finally, accurate fiber placement can be achieved, so repeating layers and having a high fiber volume parts is not a problem. Otherwise, in filament winding the mandrel removal can be complicated especially in non-uniform shapes, because of this, mandrels should be made of frangible or dissolvable materials, and this make it expensive mandrels. Filament winding has a poor surface finishing, which may affect the structure's aesthetics [101].

2.7 Composite Failure Theories

In this section, three composite failure theories, that will be used in finite element modelling, will be explained with equations and details; maximum stress failure theory, maximum strain failure theory and Chang/Chang failure theory.

2.7.1 Maximum stress failure theory

This theory is applied to isotropic materials, as the stresses acting on a lamina are resolved into the normal and shear stresses in the local axes. Failure is predicted in a lamina, if any of the normal or shear stresses in the local axes of a lamina is equal to or exceeds the corresponding ultimate strengths of the unidirectional lamina [102]. The lamina is fails if:

$$-X_{c,a} < \sigma_a < X_{t,a} \tag{2.6}$$

$$-Y_{c,b} < \sigma_b < Y_{t,b} \tag{2.7}$$

$$-S_c < \tau_{ab} < S_c \tag{2.8}$$

2.7.2 Maximum strain failure theory

This theory is applied to isotropic materials. The strains applied to a lamina are resolved to strains in the local axes. Failure is predicted in a lamina, if any of the normal or shearing strains in the local axes of a lamina equal or exceed the corresponding ultimate strains of the unidirectional lamina. Given the strains/stresses in an angle lamina, one can find the strains in the local axes [102]. A lamina fails if:

$$-\varepsilon_{c,a} < \varepsilon_a < \varepsilon_{t,a} \tag{2.9}$$

$$-\varepsilon_{c,b} < \varepsilon_b < \varepsilon_{t,b} \tag{2.10}$$

$$-\gamma_{ab,ult} < \gamma_{ab} < \gamma_{ab,ult} \tag{2.11}$$

The maximum strain failure theory is like the maximum stress failure theory in that no interaction occurs between various components of strain. However, the two failure theories give different results because the local strains in a lamina include the Poisson's ratio effect. In fact, if the Poisson's ratio is zero in the unidirectional lamina, the two failure theories will give identical results.

2.7.3 Matzenmiller's failure theory

In Matzenmiller's failure theory, it has the ability to model the damages independently in the principle axis direction of any orthotropic material [103], Equations (2.12) and (2.13) describes how this theory works.

$$\begin{bmatrix} \sigma_a \\ \sigma_b \\ \tau \end{bmatrix} = \frac{1}{c} \begin{bmatrix} (1-\omega_a)E_a & (1-\omega_a)(1-\omega_b)v_{ba}E_b & 0 \\ (1-\omega_a)(1-\omega_b)v_{ab}E_a & (1-\omega_b)E_b & 0 \\ 0 & 0 & c(1-\omega_s)G \end{bmatrix} \times \begin{bmatrix} \varepsilon_a \\ \varepsilon_b \\ \gamma \end{bmatrix} \tag{2.12}$$

$$c = 1 - (1-\omega_a)(1-\omega_b)v_{ab}v_{ba}$$

$$\omega = 1 - \frac{\alpha X_{t,c}}{E_\varepsilon} \qquad (2.13)$$

Where σ is normal stress, τ is shear stress, ε is normal strain, γ is shear strain, E is Young's modulus, G is shear modulus, ν is Poisson's ratio, ω is a damage function, *i = 1T, 1C, 2T, 2C, S* (T = tensile, C = compressive, S = shear), X is strength, α is a limiting stress ratio to the peak stress.

2.7.4   Chang/Chang failure theory

In Chang/Chang failure criteria, the failure of elements can occur in tensile fiber mode, compressive fiber mode, tensile matrix mode and compressive matrix mode. As shown by Equations (2.14), (2.15), (2.16) and (2.17), e_f, e_c, e_m and e_d are history variables, which represents respectively, tension failure for fiber direction, compression failure for fiber direction, tension failure for matrix direction and compression failure for matrix direction [104, 105].

Tensile fiber mode when $\sigma_{aa} \geq 0$,

$$e_f^2 = \left(\frac{\sigma_{aa}}{X_t}\right)^2 + \beta \left(\frac{\sigma_{ab}}{S_c}\right) - 1 \begin{cases} \geq 0 & failed \\ < 0 & elastic \end{cases} \qquad (2.14)$$

Upon failure: $E_a = E_b = G_{ab} = \nu_{ba} = \nu_{ab} = 0$

Compressive fiber mode when $\sigma_{aa} < 0$,

$$e_c^2 = \left(\frac{\sigma_{aa}}{X_c}\right)^2 - 1 \begin{cases} \geq 0 & failed \\ < 0 & elastic \end{cases} \qquad (2.15)$$

Upon failure: $E_a = \nu_{ba} = \nu_{ab} = 0$

Tensile matrix mode when $\sigma_{bb} \geq 0$,

$$e_m^2 = \left(\frac{\sigma_{bb}}{Y_t}\right)^2 + \left(\frac{\sigma_{ab}}{S_c}\right)^2 - 1 \begin{cases} \geq 0 & failed \\ < 0 & elastic \end{cases} \qquad (2.16)$$

31

Upon failure: $E_b = v_{ba} = 0 \rightarrow G_{ab} = 0$

Compressive matrix mode when $\sigma_{bb} < 0$,

$$e_d^2 = \left(\frac{\sigma_{bb}}{2S_c}\right)^2 + \left[\left(\frac{Y_c}{2S_c}\right)^2 - 1\right]\frac{\sigma_{bb}}{Y_c} + \left(\frac{\sigma_{ab}}{S_c}\right)^2 - 1 \begin{cases} \geq 0 & failed \\ < 0 & elastic \end{cases} \tag{2.17}$$

Upon failure: $E_b = v_{ba} = v_{ab} = 0 \rightarrow G_{ab} = 0$

2.8   Micro Failure Modes in Composites

In practice, when a fiber-reinforced composite material is subjected to loading, not all of fibers have equal strength. Therefore, fibers will be broken in a statistical distribution; low stress fibers will break first and the remaining fibers will carry higher stresses. Due to the high stress concentration carried by the fibers, microcracks in the matrix will start. As the matrix is a ductile material, plastic deformation or micro-yielding will start. At the end, fiber breakage or pullout will be recognized clearly, due to the high local stress concentrations [99]. Figure 2-19 summarizes the micro-failure modes in longitudinal tension.

(a) Debonding of the broken fiber   (b) Matrix cracking   (c) Fiber breakage
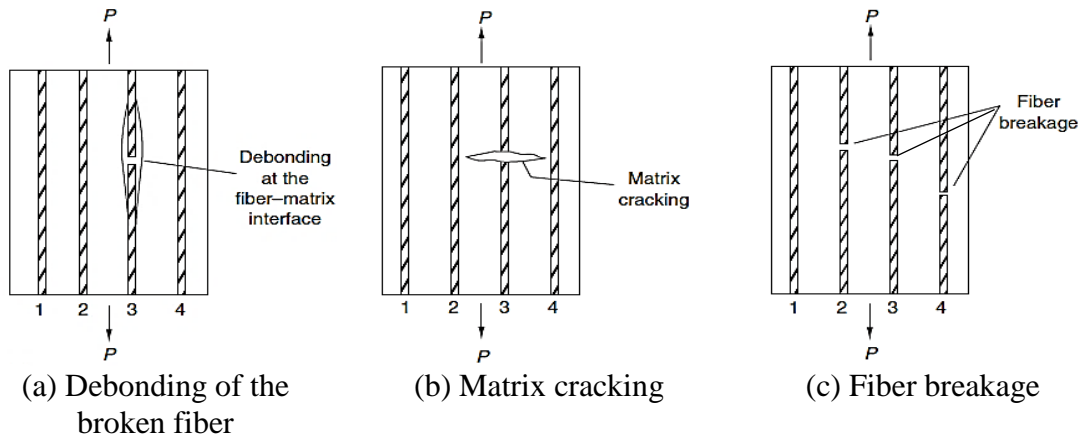
Figure 2-19: Micro-failure modes in fiber direction [99]

2.8.1 Matrix failure

When a composite material subjected to compressive load, matrix micro-failure will occur, the matrix cracking is usually at an angle to the loading direction. Therefore, this micro-failure mode is a shear matrix failure (Figure 2-20-a) [106]. While if the composite material is subjected to tensile loading, micro-failure will occur perpendicularly to the transverse tension (Figure 2-20-b).

(a) Shear matrix failure in transverse compression

(b) Tensile matrix failure perpendicular to transverse tension

Figure 2-20: Matrix failure modes [107]

2.8.2 Fiber failure

Many micro-failure modes will happen if a composite material is subjected to compressive load in fiber direction. Transverse tensile micro-failure mode observed to initiate cracks at the interface between fiber and matrix, attributed to Poisson's ratio effect, causing tensile stresses in transverse direction. Also, fiber micro-bucking can occur. If the fibers are densely packed, shear failure mode will occur, since the matrix shows mostly shear strains (Figure 2-21-a) [106] For carbon fibers, the angle of the crack is often at approximately 45° to the loading axis [108].

(a) Shear fiber failure due to compression in fiber direction

(b) Tensile fiber failure perpendicular to tensile load in fiber direction

Figure 2-21: Fiber failure modes [107]

2.8.3 Delamination failure

Agarwal *et al* [108], have divided the energy absorption mechanisms during fracture into two mechanisms; deformation of the material and formation of new surfaces (cracks). If cracks occurred in a loaded composite material, these cracks will absorb an amount of energy, causing propagating of the cracks along the ply. These cracks can extend to reach the other plies in the composite structure, causing debonding and separation between the laminates. Delamination is usually found in samples which are subjected to bending, because of the predominant out-of-plane shear stresses.
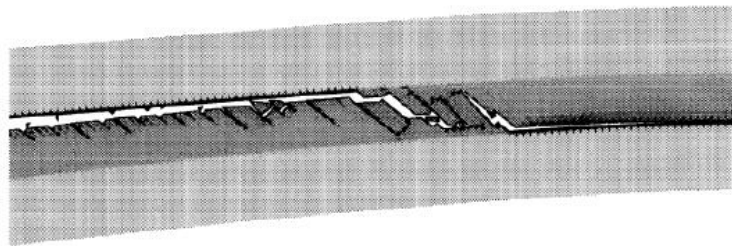
Figure 2-22: Delamination in sample due to impact which has caused bending [109]

2.9 Summary

In this chapter, a literature review related to this research has been presented to create an understanding of the research background. Five aspects have been covered; (1) Ballistic protection, which presents the body armors through the history and body armor classifications. (2) Ballistic performance evaluation. (3) Factors affecting composite body armors. (4) Fabrication processes of composite body armor. (5) Mechanics of composite materials, which presents the composite failure theories and the micro-failure modes in composite materials. In next chapter, the experimental and numerical programs methodologies are presented with detailed description.

CHAPTER 3

METHODOLOGY

In this chapter methods that were implemented to carry out the study are described. The methodology has been divided into three phases concerning the problem solution. This methodology has been divided into two sections concerning the problem solutions. The first section is the experimental program and the finite element program. In the experimental program section, the fabrication processes for the body armor plates are mentioned with details and pictures. While in the finite element program section, the effect of material stacking sequence, conical angle effect on the ballistic behavior of body armor plates has been simulated using ANSYS/LS-DYNA. The developed finite element model has been described, presented and verified in details. The flow chart for this investigation is shown in Figure 3-1, in which description for the outline of the study is presented in details.

3.1   Experimental Program

3.1.1   Fabrication Processes

3.1.1.1   Vacuum infusion process

Flat and curved body armor plates were fabricated using vacuum infusion process. Two different fabrics were used; woven Kevlar® and woven carbon fiber with different sequences. The plates dimensions are $250 \, \text{mm} \times 300 \, \text{mm}$. In vacuum infusion process, high strength samples with good surface finishing, more reliability and less resin for the ballistic test have been achieved. Table 3-1 summarizes the fabricated samples with their characteristics.

METHODOLOGY

EXPERIMENTAL PROGRAM

STRUCTURAL GEOMETRY

Bullet guiding pocket

Flat body armor plate

Curved body armor plate

Material
- KFRP
- CFRP

Material
- KFRP
- CFRP/KFRP
- CFRP/KFRP/DPRP

Material
- KFRP
- KFRP/CFRP

Bullet Guiding Pocket Armor Plate (BGPAP)

Material
- KFRP/CFRP

FINITE ELEMENT WORK

STRUCTURAL GEOMETRY

Flat body armor plate

Bullet guiding pocket

Material
- KFRP
- CFRP/KFRP

Material
- KFRP
- CFRP

Bullet Guiding Pocket Armor Plate (BGPAP)

Material
- KFRP/CFRP

Figure 3-1: Flow chart describes the plan to carry out this research.

Table 3-1: Summary of the characteristics for the fabricated body armor plates.

Plate type	Material sequence	Sample ID	Thickness [mm]	Weight [g]	Total no. of sample
Flat non-hybrid [KFRP]$_{40}$ plate	[KFRP]$_{40}$	1	10.1±0.3%	746±0.4%	3
		2	9.8±2.7%	723±2.7%	
		3	10.3±2.3%	760±2.3%	
		average	10.07	743	
Curved non-hybrid [KFRP]$_{40}$ plate	[KFRP]$_{40}$	1	9.9±0.2%	730±0.04%	3
		2	9.85±0.7%	726±0.6%	
		3	10±0.8%	735±0.64%	
		average	9.92	730.3	
Flat hybrid [CFRP$_4$/KFRP$_6$]$_4$ plate	[(CFRP)$_4$ / (KFRP)$_6$ / (CFRP)$_4$ / (KFRP)$_6$ / (CFRP)$_4$ / (KFRP)$_6$ / (CFRP)$_4$ / (KFRP)$_6$]	1	12.8±2.1%	822±2.4%	3
		2	13.4±2.5%	845±0.36%	
		3	13±0.5%	859±2%	
		average	13.07	842	
Curved hybrid [CFRP$_4$/KFRP$_6$]$_4$ plate	[(CFRP)$_4$ / (KFRP)$_6$ / (CFRP)$_4$ / (KFRP)$_6$ / (CFRP)$_4$ / (KFRP)$_6$ / (CFRP)$_4$ / (KFRP)$_6$]	1	12.6±0.24%	792±0.25%	3
		2	12.5±0.56%	790±0.5%	
		3	12.6±0.24%	800±0.76%	
		average	12.57	794	
Flat hybrid [CFRP$_{10}$/KFRP$_{30}$] plate	[(CFRP)$_{10}$ / (KFRP)$_{30}$]	1	11.1±0%	915±0%	3
		2	11.4±2.7%	923±0.87%	
		3	10.8±2.7%	907±0.87%	
		average	11.1	915	
Curved hybrid [CFRP$_{10}$/KFRP$_{30}$] plate	[(CFRP)$_{10}$ / (KFRP)$_{30}$]	1	11.1±0%	901±0.14%	3
		2	11±0.9%	895±0.81%	
		3	11.2±0.9%	911±0.96%	
		average	11.1	902.3	
Flat [CFRP$_4$/[DPRP$_2$/ KFRP$_{10}$]$_3$] plate	[(CFRP)$_4$ / (DPRP)$_2$/ (KFRP)$_{10}$/ (DPRP)$_2$/ (KFRP)$_{10}$/ (DPRP)$_2$/ (KFRP)$_{10}$]	1	16.3±0%	1496±0.86%	3
		2	16.5±1.23%	1525±1.1%	
		3	16.1±1.23%	1507±0.13%	
		average	16.3	1509	

Flat and curved non-hybrid [KFRP]$_{40}$ body armor plates: Forty layers of woven Kevlar were used to fabricate the flat and curved plates. Resin was infused to the dry fabrics depending on the pressure difference in vacuum infusion. The resin was cured for 24 hours under atmospheric conditions. Figure 3-2 shows the vacuum infusion fabrication process and the final product of the curved non-hybrid [KFRP]$_{40}$ body armor plate.

| (a) Vacuum infusion fabrication process | (b) Final product |

Figure 3-2: Curved non-hybrid [KFRP]$_{40}$ body armor plate.

Flat and curved hybrid [CFRP$_4$/KFRP$_6$]$_4$ body armor plates: In flat and curved hybrid [CFRP$_4$/KFRP$_6$]$_4$ body armor plate, carbon fiber was added to examine its effect on ballistic protection. Carbon fiber has high strength-to-weight, due to this using it in ballistic plates may reduce the weight of the plate with high level of ballistic protection. The layers' configuration that are used in these armor plates is (4 layers CFRP - 6 layers KFRP)×4. Figure 3-3 shows the fabrication process and final product of the curved hybrid [CFRP$_4$ /KFRP$_6$]$_4$ body armor plate.

| (a) Vacuum infusion fabrication process | (b) Front face of final product | (c) Back face of final product |
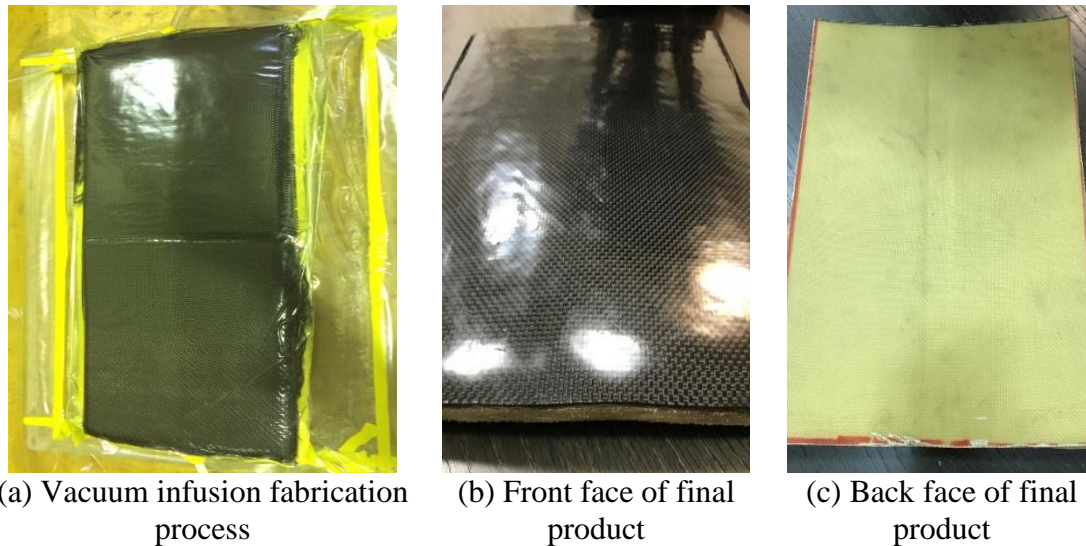
Figure 3-3: Curved hybrid [CFRP$_4$/KFRP$_6$]$_4$ body armor plate.

Flat and curved hybrid [CFRP$_{10}$/KFRP$_{30}$] body armor plates: The idea for these flat and curved hybrid [CFRP$_{10}$/KFRP$_{30}$] body armor plate came from the ceramic faced/composite backed body armor plate that is used nowadays. In this plate the ceramic layer is replaced by many layers of CFRP; to check if these layers can act like ceramic and break the tip of the bullet before penetrating the KFRP layers. This will make a huge reduction in plate's weight. Figure 3-4 shows the final product of the curved hybrid [CFRP$_{10}$/KFRP$_{30}$] body armor plate.

Flat [CFRP$_4$/[DPRP$_2$/KFRP$_{10}$]$_3$] body armor plate: In this body armor plate, Qatari date palm leaves were introduced inside the plate, the idea was to use the natural fibers, which is known in its light weight, inside the body armor plate. In this plate, four CFRP layers are the face of the armor plate, six layers of NFRP were used in-between the KFRP layers. Figure 3-5-a shows the natural fiber layers that were used and Figure 3-5-b shows the final product of the flat [CFRP$_4$/[DPRP$_2$/KFRP$_{10}$]$_3$] body armor plate.
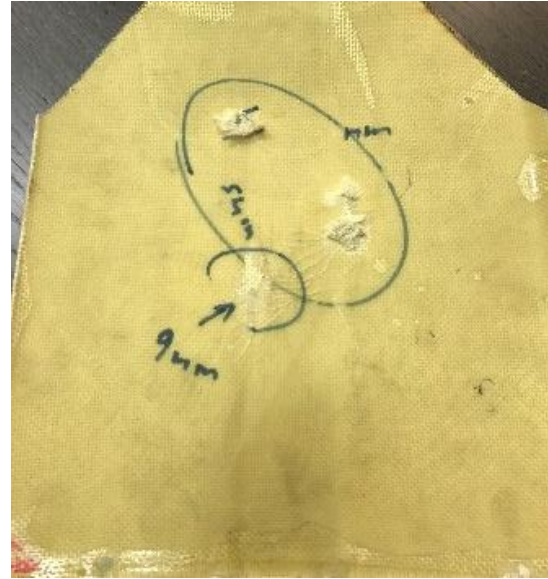
|(a) Front face|(b) Back face|

Figure 3-4: Curved hybrid [CFRP$_{10}$/KFRP$_{30}$] body armor plate;
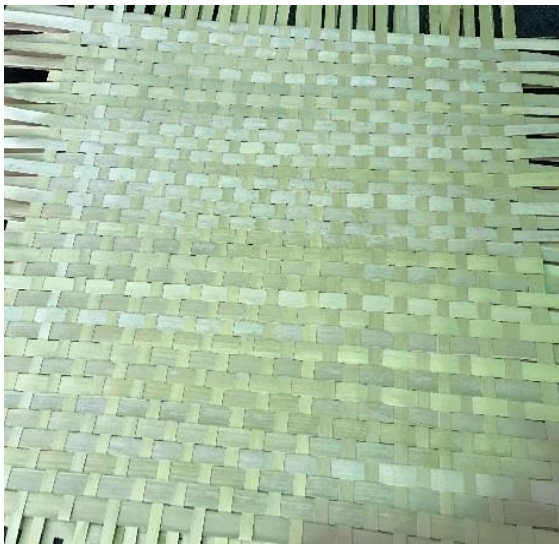
(a) Untreated Qatari date palm fibers (b) Flat [CFRP$_4$/[DPRP$_2$/KFRP$_{10}$]$_3$] body armor plate

Figure 3-5: Flat [CFRP$_4$/[DPRP$_2$/KFRP$_{10}$]$_3$] body armor plate

```
                    ┌──────────────────────────────┐
                    │   EXPERIMENTAL PROGRAM       │
                    └──────────────────────────────┘
                                   │
                                   ▼
                    ┌──────────────────────────────┐
                    │    FABRICATION PROCESSES     │
                    └──────────────────────────────┘
```

Figure 3-6: Flow chart describes the experimental program plan

EXPERIMENTAL PROGRAM

FABRICATION PROCESSES

VACUUM INFUSION

3D PRINTING

FILAMENT WINDING

Flat & curved body armor plate

ABS (Acrylonitrile Butadiene Styrene) plastic BGP

Bullet guiding pockets

Effect of material sequence

$35°$ $40°$ $45°$ $50°$ $55°$

CFRP KFRP

Non-hybrid $[KFRP]_{40}$ plate

Hybrid $[CFRP_4/KFRP_6]_4$ plate

Hybrid $[CFRP_{10}/KFRP_{30}]$ plate

$[CFRP_4/[DPRP_2/KFRP_{10}]_3]$ plate

Effect of geometry (conical angle)

$35°$ $40°$ $45°$ $50°$ $55°$

Bullet Guiding Pocket Armor Plate (BGPAP)

Figure 3-6: Flow chart describes the experimental program plan

3.1.1.2   3D printing

The 3D printed conical tubes were made of ABS plastic (Acrylonitrile Butadiene Styrene) with 1 mm thickness. Five different conical angles were printed, ranges from 35° to 55° with 5° increment each time. All the conical tubes have a height of 150 mm with five cone steps as shown in Figure 3-7. The major diameter of all conical tubes is 54 mm while the minor diameter differs depending on the conical angle. The mechanical properties of the ABS plastic are listed in Appendix A.

(a) 35°ABS BGP   (b) 40°ABS BGP   (c) 45°ABS BGP   (d) 50°ABS BGP   (e) 55°ABS BGP

(f) General scheme of ABS BGP
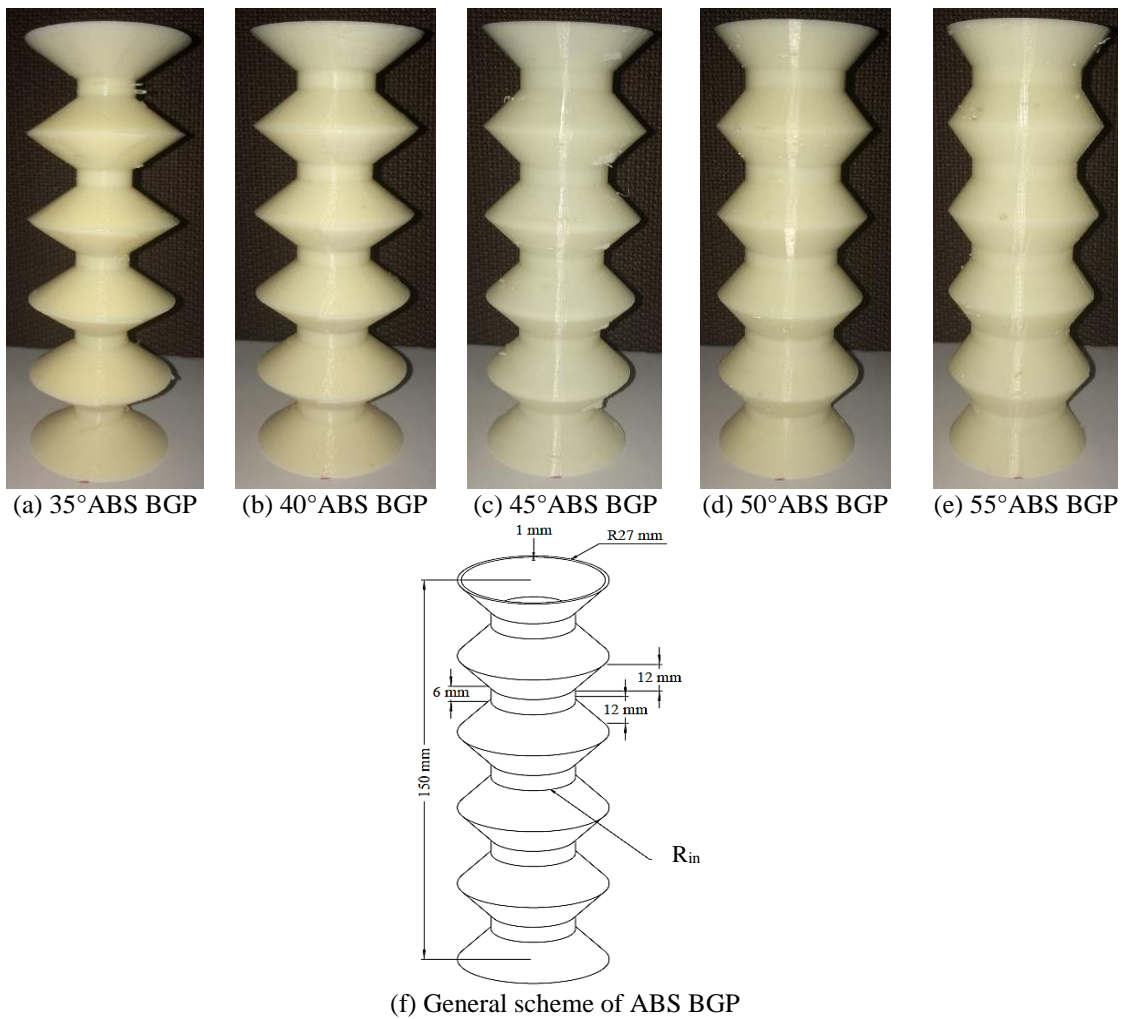
Figure 3-7: 3D printing process of BGP.

Table 3-2: ABS plastic cones weight

	ABS plastic cones [gram]	Inner diameter (R_{in}) [mm]	No. of samples
35°	25.7	9.86	3
40°	25.5	12.7	3
45°	25.3	15	3
50°	24.9	16.92	3
55°	24.7	18.6	3

3.1.1.3   Filament winding

The composite bullet guiding pockets were fabricated using filament winding process. The conical mandrels were 3D printed as mentioned above, and the fibers were wrapped up around the mandrel radially (fiber wrapping angle = 0°); to fill the outside gaps between the cones to get a solid composite cylinder. Two different fibers were used; carbon fiber and Kevlar®. Due to the corrugated shape of the ABS plastic conical molds, the winding process was assisted with the horizontal carriage of lathe machine at a constant rotating speed of 96 RPM. Fibers were immersed in resin and wiped by a brush to remove the excess resin. Figure 3-8 shows the fabrication process. The samples were cured in oven for 8 hours at 80°C. Figure 3-8-d and e show the final products. ABS conical tubes were not removed from the samples as having 1 mm thickness of ABS plastic will not make a major difference in energy absorption capability. The mechanical properties of the used UD carbon fiber/epoxy, UD Kevlar®/epoxy are listed in Appendix A.

(a) Filament winding process. (b) Kevlar filament. (c) Carbon fiber filament.

(d) Final product of 45° CFRP BGP (e) Final product of 45° KFRP BGP

Figure 3-8: CFRP and KFRP BGP

Table 3-3: CFRP and KFRP BGP weight

Conical angle	Sample ID	CFRP mass [gram]	KFRP mass [gram]
35°	1	312.5±0.16%	250.2±0.48%
	2	316.5±1.12%	245.9±1.2%
	3	310.2±0.89%	251±0.8%
	average	313	249
40°	1	285.6±2.82%	240.8±0.04%
	2	295.6±0.58%	242.2±0.54%
	3	300.5±2.25%	239.7±0.5%
	average	293.9	240.9
45°	1	229±0.13%	204±1%
	2	233±1.6%	200±1%
	3	226±1.44%	201±0.5%
	average	229.3	202
50°	1	213±0.06%	199±0.5%
	2	216±0.08%	203±1.5%
	3	214±0.01%	199±0.5%
	average	214.3	200
55°	1	199±0.15%	167±1.2%
	2	202±1.7%	160±3%
	3	195±1.86%	169±2.4%
	average	198.7	165

3.1.2 Testing procedure

3.1.2.1 *Body armor plates*

Real shooting test was performed to test the composite body armor plates, 9 mm FMJ RN bullet was used to test the ballistic behavior of these plates. 3 bullets were shot for each sample from 15 m away.

3.1.2.2 *Bullet guiding pocket*

A quasi static slipping process at speed of 15 mm/min for a stroke of approximately 60 mm was carried out, to calculate the energy absorption capability of the bullet guiding pockets. Using Instron machine with 250 kN capacity.

3.2 Finite Element Simulation Program

Finite element analysis (FEA) is a numerical method for solving partial differential equations (PDE) with boundary values (BV). By dividing the problem into small parts which are called the finite elements. FEA is widely used in structural analysis, solid mechanics, thermal analysis, electrical analysis, and dynamic problems. Figure 3-9 shows a flow chart for the finite element modelling.

3.2.1 Time integration numerical method

In finite element analysis, usually the time-step method is used, which is classified into explicit or implicit. Explicit computational algorithm uses the central difference numerical method for integration, while the implicit method uses the Newark forward difference numerical method. The major difference between the explicit and implicit methods is the requirement on the time-step size Δt. The explicit solution is stable if the time-step Δt is smaller than Δt_{cr}, where Δt_{cr} is the critical time-step for shell elements, $\Delta t_{cr} = \frac{L_s}{c}$ (where

L_s is the characteristic length and C is the speed of sound). The implicit method is not bound by the time-step size, therefore unconditionally stable for large time steps. In time integration method, accelerations, velocities and displacement are expressed in the following equation:

$$M \frac{\partial^2 u}{\partial t^2} + Ku = F(t, u)$$

(3.1)

Where, M is the mass matrix, K is the stiffness, u is the displacement vector to a load vector of F.
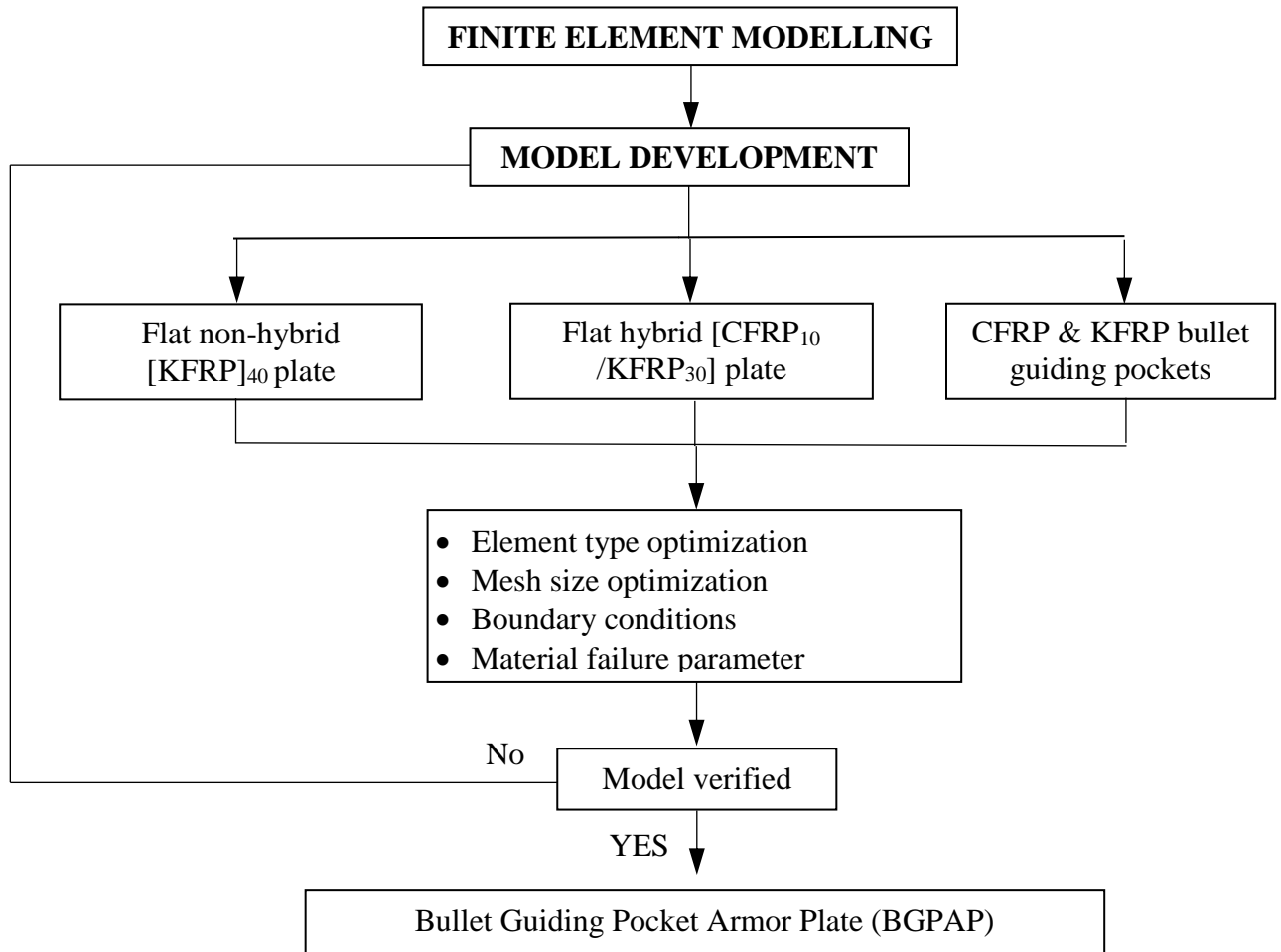
Figure 3-9: FEM flow chart

3.2.1.1 The explicit method

Explicit numerical method is used to solve the future value of the solution at a single node in terms of only past values. That means, when the only unknown is the future value of the solution at a single node, and everything else on the right-hand side of the finite difference equation is a solution derived at earlier time step, the velocity and acceleration are expressed in Equations (3.2) and (3.3) respectively.

$$\left.\frac{\partial u}{\partial t}\right|_{j+1} \cong \frac{u^{j+1} - u^j}{\Delta t} \tag{3.2}$$

$$\left.\frac{\partial^2 u}{\partial t^2}\right|_{j} \cong \frac{1}{2\Delta t}\left[\left.\frac{\partial u}{\partial t}\right|_{j+1} - \left.\frac{\partial u}{\partial t}\right|_{j-1}\right] \tag{3.3}$$

Where j is the current time-step, $j+1$ the next time-step, $j-1$ is the previous time-step. Substituting Equation (3.2) in Equation (3.1) for the current time-step j, to obtain the displacement at next time-step $j+1$ as shown in Equation (3.4):

$$Mu_{j+1} = \Delta t^2 F_j + (2M - \Delta t^2 K)u_j - Mu_{j-1} \tag{3.4}$$

u_{j+1} is known then the velocity of $j+1$ can be determined and acceleration of j is calculated between $j-1$ and $j+1$.

3.2.2 ANSYS/LS-DYNA

In this study, the finite element model was created and built using the pre-processor LS-PREPOST, while solving the finite element code was generated by ANSYS/LS-DYNA solver from ANSYS software, and finally, the solved data was analyzed using the post-processor from LS-PREPOST. The first step was creating the geometry of the structure and assigning its dimensions, then meshing it with the suitable mesh type and size, as the

solution of the meshed geometry will be affected by the type and size of the mesh, all was done using the pre-processor LS-PREPOST. The material and contact type, boundary and initial conditions were specified in the pre-processor. Once the finite element model was completed, ANSYS/LS-DYNA solver was ready to solve the finite element code.

ANSYS/LS-DYNA software is a general-purpose transient dynamic finite element program capable of simulating complex real world problems. It is used by the Aerospace, Automobile, Manufacturing, Military and Bioengineering industries. ANSYS/LS-DYNA simulates highly nonlinear physical problems which uses explicit and implicit time integration. Those problems change their boundary conditions and material behavior within deformation, e.g. thermoplastic polymers do not exhibit ideally elastic behavior during deformation. Usually these problems are subjected to high speed and large deformations in short time duration where inertial forces are very important, and that what is meant by transient dynamics, e.g. automotive crashing (deformation of chassis, airbag inflation, seatbelt tensioning), explosions, bullet impact, drop testing, sheet metal forming.

ANSYS/LS-DYNA offers many options that makes it very useful tool for solving complex problems. One of the main important options that is provided by the software is creating an automatic definition of the contact type between geometries in the structure. The software also provides a huge library of material types with different failure modes and behaviors.

3.2.3 Body armor plates and bullet guiding pockets FEM

In this section, the body armor plates and composite bullet guiding pockets were modelled in ANSYS/LS-DYNA, the non-hybrid $[KFRP]_{40}$ and the hybrid $[CFRP_{10}/KFRP_{30}]$ body

armor plates were shot by 9 mm FMJ RN bullet, while the composite bullet guiding pockets were tested under quasi-static sliding crushing test. The tested flat plates are 10"×12", and the composite conical tubes are 150 mm in height and 54 mm in outer diameter. Geometry modelling, meshing, material used in modelling, boundary conditions and contact formulation are stated below. Figure 3-10 shows a general FEM of the flat body armor plates and Figure 3-11 shows a general FEM of the parts that forms the composite conical tubes.

3.2.3.1   Geometry modelling and meshing

The flat plates and conical tubes were drawn using SOLIDWORKS software with detailed dimensions as shown in Figure 3-12 and Figure 3-13. Meshing for the flat plates was biased meshing with different element sizes due to the symmetry of the plate. Meshing of conical ABS plastic shells was 2D mixed mesh, while for the solid conical tubes was 3D quadratic. Table 3-4 and Table 3-5 summarize the number of elements and nodes, section and material model used in each part for the modelled samples.
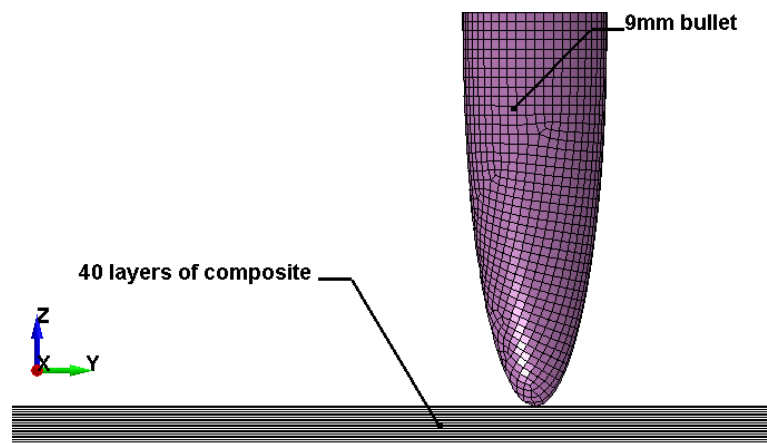
Figure 3-10: Section view of FEM for the flat composite body armor plate.
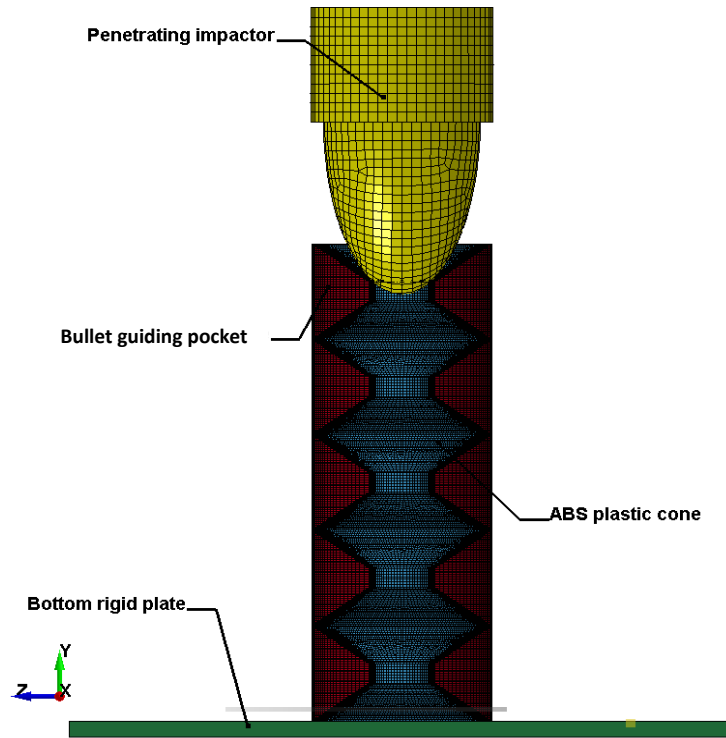
Figure 3-11: Section view of FEM for the composite BGP
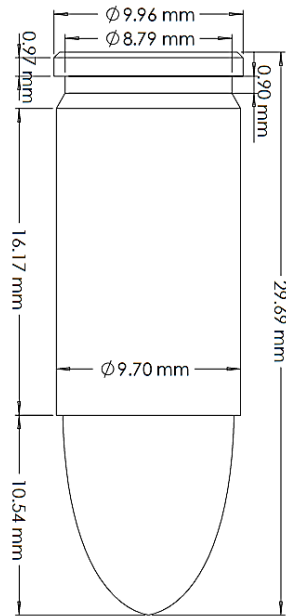
(a) Geometry of the 9mm bullet   (b) Geometry of the composite plate
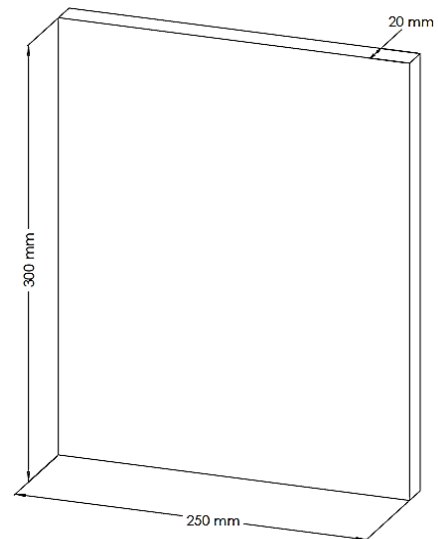
Figure 3-12: Real shooting test setup with dimensions.

(a) 35° BGP   (b) 40° BGP   (c) 45° BGP

(d) 50° BGP   (e) 55° BGP
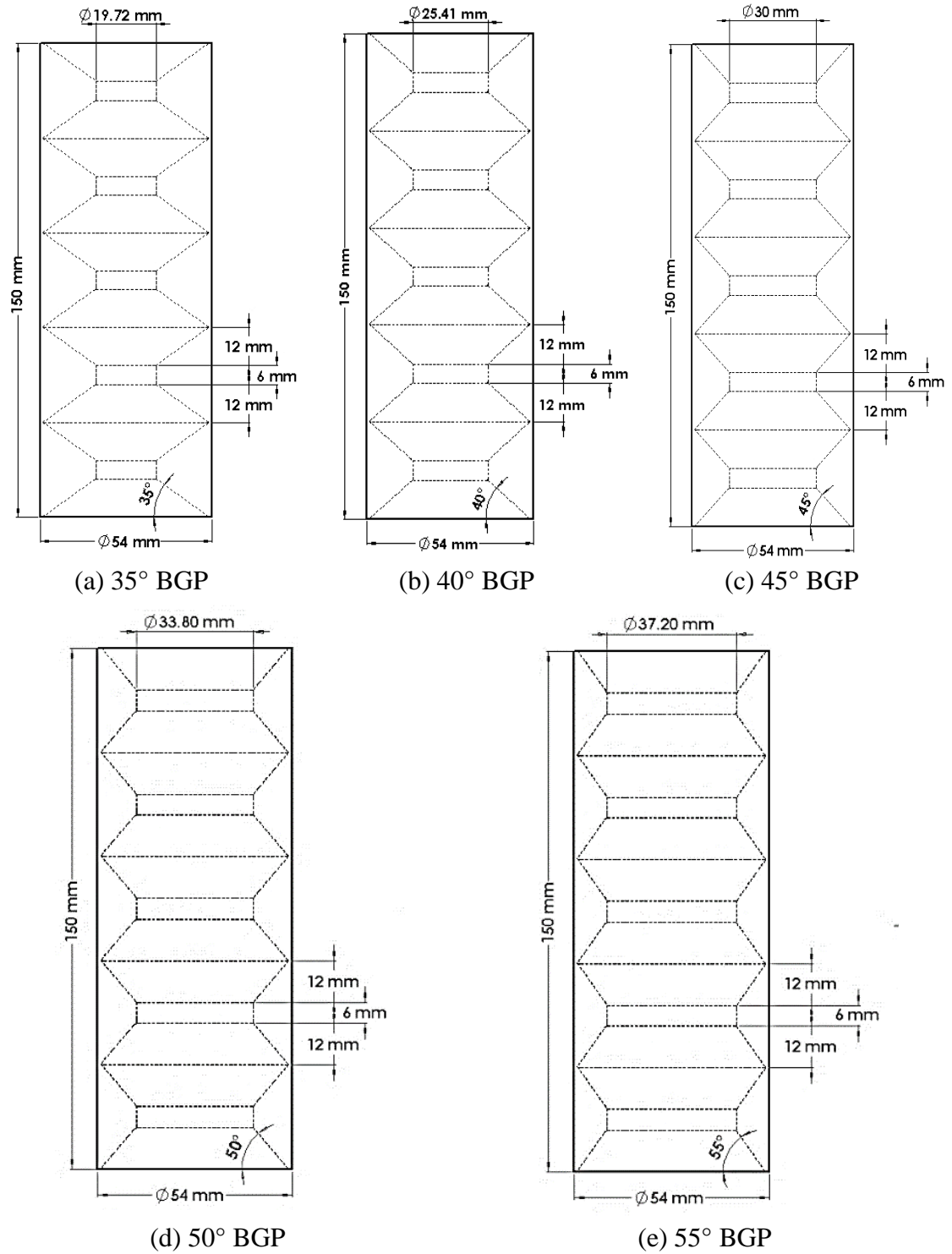
Figure 3-13: Geometry of BGP.

Table 3-4: FEM details for the flat composite body armor plates

Part ID	Part name	No. of elements	No. of nodes	Section	Material
1-40	Composite layer	3600×40	3721×40	Shell	MAT_LAMINATED_COMPOSITE_FABRIC
100	Bullet	34503	36564	Solid	MAT_ELASTIC_PLASTIC_HYDRO

Table 3-5: FEM details for the composite BGP

Part ID	Part name	Conical angle	No. of elem.	No. of nodes	Section	Material
1	Bullet guiding pocket	35°	12640	15392	Solid	MAT_ENHANCED_COMPOSITE_DAMAGE
		40°	13200	16440		
		45°	13200	16848		
		50°	13160	17136		
		55°	12600	16560		
2	ABS plastic cone	35°	6876	6880	Shell	MAT_PIECEWISE_LINEAR_PLASTICITY
		40°	6378	6406		
		45°	6367	6401		
		50°	6287	6353		
		55°	6198	6194		
3	Impactor	-	2503	2490	Shell	MAT_RIGID
4	Bottom plate	-	1	8	Solid	MAT_RIGID

3.2.3.2 Material modelling

ANSYS/LS-DYNA provides many material models in its huge material library, 5 material models were used to simulate the FEMs, MAT_058 was used to model the composite woven fabrics of Kevlar and carbon fiber that were used in flat body armor plates. MAT_010 was used to model the bullet in the real shooting test of the flat body armor plates. MAT_054 was used to model the composite bullet guiding pockets (CFRP and KFRP). MAT_024 was used to model the ABS plastic cone and MAT_020 was used to

model the rigid bottom plate and the rigid impactor. A full description of each material and its failure criteria are presented below.

MAT_LAMINATED_COMPOSITE_FABRIC (MAT_058)

MAT_058 was used to model the non-hybrid $[KFRP]_{40}$ and hybrid $[CFRP_{10}/KFRP_{30}]$ body armor flat plates that were tested by the real shooting test. The woven Kevlar/epoxy and woven carbon-fiber/epoxy were represented as shell layers in the FEM. This material model is based on Matzenmiller's damage mechanics model, which has the ability to model the damages independently in the principle axis direction of any orthotropic material [103], which makes it suitable for fabric composites as stated in Section 2.7.3. This material has 7 cards as shown in Table 3-6. Card 1 and 2 represent the elastic orthotropic material parameters for the longitudinal, transverse and normal directions (red color variables). The out-of-plane material properties Young's modulus (E_c) is not required for the fabric material. The blue variables (cards 2, 3, 6 and 7) are the failure modeling parameters, which makes MAT_058 a suitable choice to predict delamination accurately. Card 4 and 5 (green color variables), control the material coordinate system for each element. Table B.5 (Appendix B) has a brief description of each parameter in MAT_058.

Table 3-6: Material card for MAT_058

Card 1	MID	RO	EA	EB	(EC)	PRBA	TAU1	GAMMA1
Card 2	GAB	GBC	GCA	SLIMT1	SLIMC1	SLIMT2	SLIMC2	SLIMS
Card 3	AOPT	TSIZE	ERODS	SOFT	FS			
Card 4	XP	YP	ZP	A1	A2	A3		
Card 5	V1	V2	V3	D1	D2	D3	BETA	
Card 6	E11C	E11T	E22C	E22T	GMS			
Card 7	XC	XT	YC	YT	SC			

MAT_ELASTIC_PLASTIC_HYDRO (MAT_010)

MAT_010 was used to model the bullet used in real shooting test, as this material model is suitable for hydrodynamic materials. 6 material cards are used in this model as shown in Table 3-7. Table B.1 (Appendix B) has a brief description of each parameter in MAT_010.

Table 3-7: Material card for MAT_010

Card 1	MID	RO	G	SIGY	EH	PC	FS	CHARL
Card 2	A1	A2	SPALL					
Card 3	EPS1	EPS2	EPS3	EPS4	EPS5	EPS6	EPS7	EPS8
Card 4	EPS9	EPS10	EPS11	EPS12	EPS13	EPS14	EPS15	EPS16
Card 5	ES1	ES	ES3	ES4	ES5	ES6	ES7	ES8
Card 6	ES9	ES10	ES11	ES12	ES13	ES14	ES15	ES16

MAT_ENHANCED_COMPOSITE_DAMAGE (MAT_054)

MAT_054 was used to model the bullet guiding pockets. As mentioned before, these tubes were fabricated by filament winding process, using unidirectional carbon fibers or Kevlar. Solid elements represented these tubes. This material model is an enhanced version of material model 22 in ANSYS/LS-DYNA. It represents a progressive failure model for orthotropic materials, which makes it a suitable choice for unidirectional fibers. In MAT_054, the strains in a-direction, b-direction and ab-direction are expressed as functions of the plane-stresses and shear in the elastic region. While, beyond elastic region, MAT_054 follows Chang/Chang failure criterion [104, 105], which is stated in Section 2.7.4. Usually this material type is defined for thin shell elements, which don't have parameters in z-direction, but once the mechanical properties are defined in z-direction, the failure model will work for thick-shell and solid elements. The strains in a-direction, b-direction and ab-direction are expressed as functions of the plane-stresses and shear in the elastic region as shown in the following equations:

$$\varepsilon_a = \frac{1}{E_a}(\sigma_a - \nu_{ab}\sigma_b) \tag{3.5}$$

$$\varepsilon_b = \frac{1}{E_b}(\sigma_b - \nu_{ba}\sigma_a) \tag{3.6}$$

$$\varepsilon_{ab} = \frac{1}{2}\left(\frac{1}{G_{ab}}\tau_{ab} + \alpha\tau_{ab}^3\right) \tag{3.7}$$

In Equation (3.7), α is a weighting factor for the non-linear shear stress term. α ranges between 0 and 1, it is determined by trial and error when shear is presented in the model.

In Equation (2.14), β is the weighing factor for shear stress, which defines the influence of shear stress in the tensile fiber mode. If $\beta = 1$, Hashin failure criteria [110] will be activated. If $\beta = 0$, Equation (2.14) will be reduced to the Maximum Stress failure criteria. Otherwise, β can be adjusted by trial and error. In this FEM, the tensile stresses have less effect on the results than the compressive stresses, thus β will not make a big difference.

In ANSYS/LS-DYNA, this material has 8 cards as shown in Table 3-8: Material card for MAT_054/055. Card 1 and 2 represent the elastic orthotropic material parameters for the longitudinal, transverse and normal directions (red color variables). The out-of-plane material properties (E_c, ν_{ca}, ν_{cb}) are not required for shell elements, but once are defined, like in these models; the failure criteria can be used for solid elements. Although, MAT_054 cannot predict delamination accurately. Card 3 and 4 (green color variables), control the material coordinate system for each element. In this FEM, to present the filament wound fibers; a cylindrical coordinate system was defined by setting AOPT = 4, the vector components were defined in V1, V2, V3 parameters. V1 represents the angular direction (a-direction), V2 represents the axial direction (b-direction) and V3 represents the radial direction (c-direction) as shown in Figure 3-14.
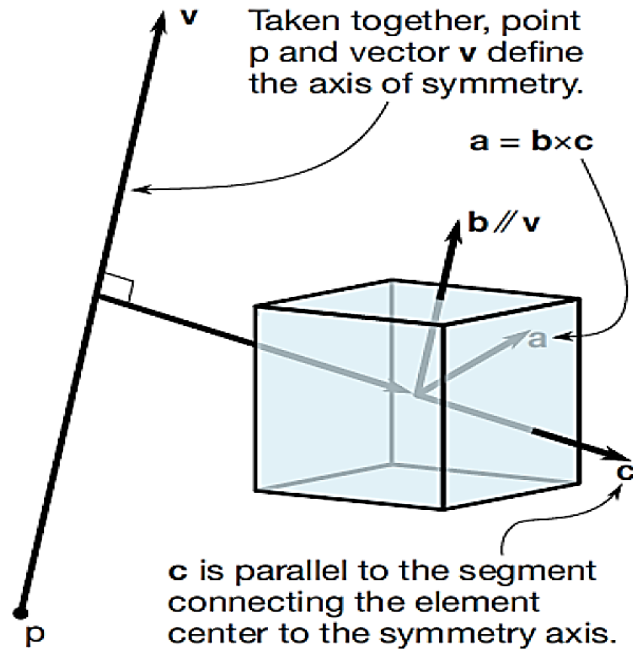
Figure 3-14: Cylindrical coordinate system defined for MAT_054

Finally, the blue variables (cards 5-9) are the failure modeling parameters. Card 5 represents the strain parameters and the unphysical tuning parameters. Table B.4 (Appendix B) has a brief description of each parameter in MAT_054.

Table 3-8: Material card for MAT_054/055

Card 1	MID	RO	EA	EB	EC	PRBA	PRCA	PRCB
Card 2	GAB	GBC	GCA	KF	AOPT			
Card 3	XP	YP	ZP	A1	A2	A3	MANGLE	
Card 4	V1	V2	V3	D1	D2	D3	DFAILM	DFAILS
Card 5	TFAIL	ALPH	SOFT	FBRT	YCFAC	DFAILT	DFAILC	EPS
Card 6	XC	XT	YC	YT	SC	CRIT	BETA	
Card 7	PFL	EPSF	EPSR	TSMD	SOFT2			
Card 8	SLIMT1	SLIMC1	SLIMT2	SLIMC2	SLIMS	NCYRED	SOFTG	
Card 9	LCXC	LCXT	LCYX	LCYC	LCSC	DT		

In this material card, if the maximum strains are defined, then strain-to-failure criterion is active. It is recommended to define the maximum strains, otherwise the elements are not

56

deleted hence, more computing time. The maximum strains in this material card are: DFAILT, DFAILC, DFAILS and DFAILM. It should be noted that the maximum matrix strain is defined for both tension and compression, thus the choice of DFAILM must be estimated if two of these limits are known for the material. Also, the residual stresses can be optionally defined in all directions in card 8: SLIMT1, SLIMT2, SLIMC1, SLIMC2 and SLIMS. Element deletion is controlled by the pre-defined maximum strains or by Chang/Chang failure criterion. In addition, the time step parameter TFAIL has other way of element deletion. This parameter works for deleting any distorted element that does not carry any load, which is not deleted by the maximum strain or Chang/Chang failure criteria.

$t_{fail} \leq 0$	No element deletion by time step size.
$0 < t_{fail} < 0.1$	TFAIL is defined in units of time. Elements are deleted when their required time step is smaller than TFAIL.
$t_{fail} \geq 0.1$	TFAIL is defined as a quotient of the initial time step. Elements are deleted when $\frac{current\ time\ step}{original\ time\ step} < TFAIL$.

If compressive matrix failure took a place in the model, FBRT and YCFAC strength reduction parameters are activated to degrade the pristine fiber strength. The following equations (3.8) and (3.9) are applied to simulate the damage occurred to the fibers from the failed matrix. FBRT ranges between 0 and 1. While YCFAC has a default value = 2.

$$XT' = XT \times FBRT \tag{3.8}$$

$$XC = YC \times YCFAC \tag{3.9}$$

$$[XT', XC', YT', YC'] = [XT, XC, YT, YC] \times SOFT \tag{3.10}$$

Other strength reduction parameter used in crushing simulation is SOFT, this parameter reduces the material strength in elements after crushing, the strength reduction follows

equation (3.10). The default value for SOFT = 1, which means no material strength
reduction. To reduce the strength value, SOFT will range between 0 and 1, and can be
determined by trial and error.

MAT_RIGID (MAT_020)

MAT_020 was used to model the penetrating impactor and the rigid bottom plate. The
penetrating impactor was constrained in all directions except the displacement in y-
direction, while the bottom plate was constrained in all transitional and rotational
directions. MAT_020 was chosen because it is very cost efficient, since rigid elements are
not counted in the element processing and there is no storing for the history variables like
stress or strain. Also, the meshing is not essential for simple shapes in rigid bodies. Table
3-9: Material card for MAT_020 shows the material card for MAT_020 and Table B.2
(Appendix B) has a brief description for each variable.

Table 3-9: Material card for MAT_020

Card 1	MID	RO	E	PR	N	COUPLE	M	ALIAS
Card 2	CMO	CON1	CON2					
Card 3	LCO or A1	A2	A3	V1	V2	V3		

MAT_PIECEWISE_LINEAR_PLASTICITY (MAT_024)

MAT_024 was used to model the ABS cone. It is often used to simulate thin walled
structures which have a linear elastic deformation behavior. As MAT_024 allows to define
an elasto-plastic material with an arbitrary stress-strain curve and arbitrary strain rate
dependency, or a plastic strain failure can be defined. Table 3-10 shows the material card
for MAT_024 and Table B.3 (Appendix B) has a brief description for each variable.

Table 3-10: Material card for MAT_024

Card 1	MID	RO	E	PR	SIGY	ETAN	FAIL	TDEL
Card 2	C	P	LCSS	LCSR	VP			
Card 3	EPS1	EPS2	EPS3	EPS4	EPS5	EPS6	EPS7	EPS8
Card 4	ES1	ES2	ES3	ES4	ES5	ES6	ES7	ES8

In this material 3 options to define the strain rate are possible; Cowper-Symonds formulation, user defined load curve, user defined stress-strain curve. In this FEM Cowper-Symonds formulation was used, which scales the yield stress according to Equation 3.11.

$$1 + \left(\frac{\dot{\varepsilon}}{C}\right)^{1/p} \tag{3.11}$$

Where the strain rate $\dot{\varepsilon} = \sqrt{\dot{\varepsilon}_{ij}\,\dot{\varepsilon}_{ij}}$, C and P are strain rate parameters. Viscoplastic parameter VP = 1 was used, and yield stress (SIGY) was defined, this yields to compute the dynamic yield stress from the static stress multiplied by Cowper-Symonds formula, according to Equation 3.12.

$$\sigma_y\left(\varepsilon_{eff}^P, \dot{\varepsilon}_{eff}^P\right) = \sigma_y^s\left(\varepsilon_{eff}^P\right) + SIGY.\left(\frac{\dot{\varepsilon}_{eff}^P}{C}\right)^{1/p} \tag{3.12}$$

3.2.3.3 Contact formulation and boundary conditions

ANSYS/LS-DYNA provides a variation of contact types and boundary conditions, depending on the equation modelled. In this FEM, four contact types were used to simulate the contact conditions of the systems; AUTOMATIC_SINGLE_SURFACE, AUTOMATIC_SURFACE_TO_SURFACE_TIEBREAK, AUTOMATIC_SURFACE_TO_SURFACE, and ERODING_NODES_TO_SURFACE. While for the boundary conditions; INITIAL_VELOCITY was set as an initial condition for the bullet in the real shooting test, BOUNDARY_SPC_SET to fix the flat body armor

plates in all in x and y-axis direction, where the z-axis is the direction of the shot bullet. PRESCRIBED_MOTION_RIGID was defined as a function of constant velocity to model the quasi-static sliding crushing test.

CONTACT_AUTOMATIC_SINGLE_SURFACE

This contact type was used in the composite conical based FEM, to prevent the penetration between the sample itself; in other words, to avoid the interpenetration between the broken or folded elements of the ABS plastic cone and the composite tube during crushing process. A contact algorithm called Penalty-Based was adjusted to check the penetration each time step depending on the nodal masses, by setting SOFT parameter = 2, which is effective in case of two different material stiffness (ABS plastic cone and the composite tube). A 0.3 value of static and dynamic coefficient of frictions was used.

CONTACT_AUTOMATIC_SURFACE_TO_SURFACE

AUTOMATIC_SURFACE_TO_SURFACE is usually used for crashworthiness and impacts, due to its properties in dealing with resulted deformations easily. This contact type was used in both real shooting test and quasi-static sliding crushing test. For real shooting test, this contact was used between the bullet and the composite plate. In the quasi-static test, this contact was used twice; firstly, to simulate the contact between the whole sample and the bottom rigid plate with coefficient of friction 0.8. Secondly, to simulate the contact between the impactor and conical tube.

CONTACT_AUTOMATIC_SURFACE_TO_SURFACE_TIEBREAK

This contact type was imposed to model the bonding between the Kevlar layers and carbon-fiber layers in the body armor plates FEM, also the bonding between the ABS plastic cone and the CFRP or KFRP conical tubes. AUTOMATIC_SURFACE_TO_SURFACE_ TIEBREAK, used to create a contact surface with a coefficient of friction between defined parts. In this contact type, shear and normal interfacial forces are considered, following tiebreak failure Equation 3.13,

$$\left(\frac{\sigma_n}{NFLF}\right)^2 + \left(\frac{\sigma_s}{SFLF}\right)^2 \geq 1 \tag{3.13}$$

Where σ_n and σ_s are the normal and shear interfacial forces, respectively. *NFLF* and *SFLF* represent the normal and shear forces that limits the bonding failure.

CONTACT_ERODING_NODES_TO_SURFACE

This contact type was used to simulate the erosion between the bullet and the composite layers in the flat body armor plates FEM, as an erosion parameter is defined as a part of the material failure criteria in MAT_058, to delete any failed element from the simulation to save computational time, since the time-step is automatically adjusted, and to avoid random contact between failed elements.

INITIAL_VELOCITY

INITIAL_VELOCITY is a keyword in ANSYS/LS-DYNA that allows the user to define translational velocities for node or set of nodes. It was used to model the impact velocity from the 9mm bullet on the composite body armor plate.

BOUNDARY_PRESCRIBED_MOTION_RIGID

A constant velocity was applied to the moving rigid impactor in negative y-direction for the quasi-static sliding crushing test. No Gravitational forces were defined, as the crushing speed is constant so the effect of gravity can be neglected. The crushing results are independent of the mass of the impactor and that's why the impactor was modelled as rigid shell part.

3.2.4   Element types and mesh optimization

In FEM, many finite element types are used; depending on the physical equation, loading and boundary conditions, most of the common element types are; solid, shell, thick-shell, beam, etc... In this finite element modeling, solid and shell elements will be used. Solid elements are 3D finite elements for modelling solid structures. Solid elements give a realistic physical behavior, although the computational time is not efficient most of the times, as the equation is more complicated in 3D. On the other hand, shell elements are 2D finite elements that are usually used in modelling simple and thin structures. In this FEM, solid elements will be used to model the composite material tubes, while the ABS plastic cones will be modelled using shell elements.
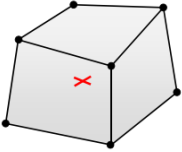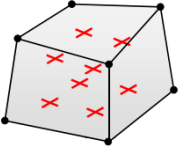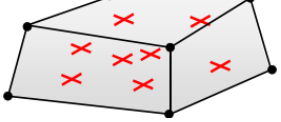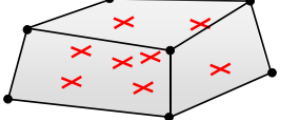
ANSYS/LS-DYNA provides many element formulations (theories) for each element type. The choice of element formulation depends on many factors such as; the required accuracy in simulation, required time in solving and type of material used. In this parametric study, four different quadratic solid element formulations (ELFORM) were studied; -2, -1, 1 and 2.

- ELFORM -2: fully integrated selective reduced intended for elements with poor aspect ratio, accurate formulation.

- ELFORM -1: fully integrated selective reduced intended for elements with poor aspect ratio, efficient formulation.

- ELFORM 1: constant stress solid elements

- ELFORM 2: fully integrated selective reduced solid.

Table 3-11 gives a brief description of the quadratic solid element formulations used. For shell elements, Belytschko-Tsay formulation was used (ELFORM = 2), that uses one integration point.

Table 3-11: Element formulations for quadratic solid element type

ELFORM	No. of nodes	Pros	Cons	
1	1	Constant stress, Efficient & accurate for large deformations	Hourglass needed for stabilization	
2	8	No hourglass needed	Slow, Stiff, Unstable for large deformation	
-1	8	Efficient, for poor aspect ratio elements	Hourglass needed	
-2	8	Accurate, for poor aspect ratio elements	High computational time	

Notes:

- Fully integrated expression means the number of Gaussian points needed for integration the polynomial terms in the stiffness matrix.

- Hour glassing expression is a zero-energy parameter, which oscillates at frequency higher than the structure's global response.

The selection of the most efficient and useful ELFORM was based on the element mesh size, four different element sizes were used in this selection criteria, Figure 3-15 shows a front section view for the meshed CFRP conical tubes that were used in this parametric study. These conical tubes were impacted at 250 m/s constant speed for 60 mm stroke. Slipping force-stroke curves and eroded internal energy – time curves resulted from this parametric study are shown in Table D.1 (Appendix D) for the different element size and ELFORMs. Time required to solve each model is presented in Table 3-12.
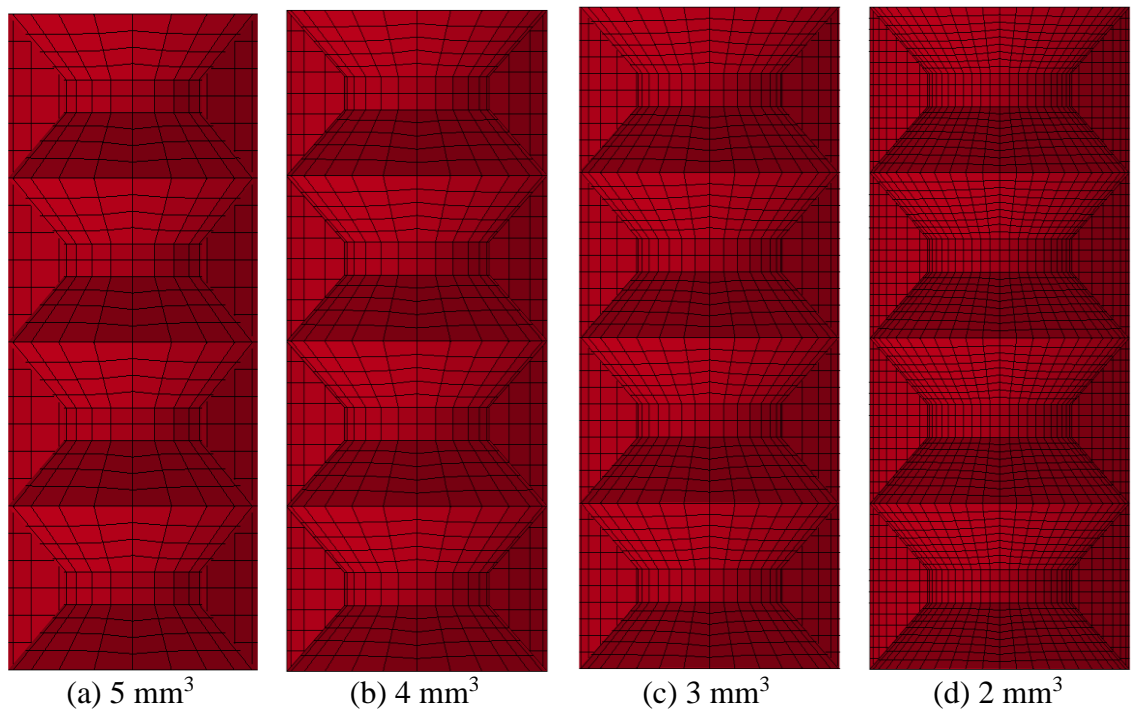

(a) 5 mm^3 (b) 4 mm^3 (c) 3 mm^3 (d) 2 mm^3

Figure 3-15: Front section view of the structure used in ELFORM

Table 3-12: Effect of element size on CPU time

ELFORM	Element size			
	5 mm^3	4 mm^3	3 mm^3	2 mm^3
1	37 s	75 s	2372 s	14445 s
2	100 s	76 s	131 s	Negative volume
-1	28 s	85 s	125 s	957 s
-2	46 s	149 s	159 s	997 s

From the previous results, it can be noticed that ELFORM 1 had the maximum internal energy. While the behavior of ELFORM -2 and -1 was almost the same, their computational time differs a little from each other due to the accuracy of ELFORM -2, their internal energy was around half of the internal energy obtained from ELFORM 1. Based on slipping force-stroke curves, ELFORM 1 had the highest crushing peaks in all the models. ELFORM 2 proved that it is not suitable for high deformation problem due to its high stiffness, the results obtained from it was totally different than other ELFORMs, which makes it the worst choice in modelling this model. Finally, ELFORM 1 was selected for modeling the sliding crushing test, because of its reasonable results that were obtained from this parametric study.
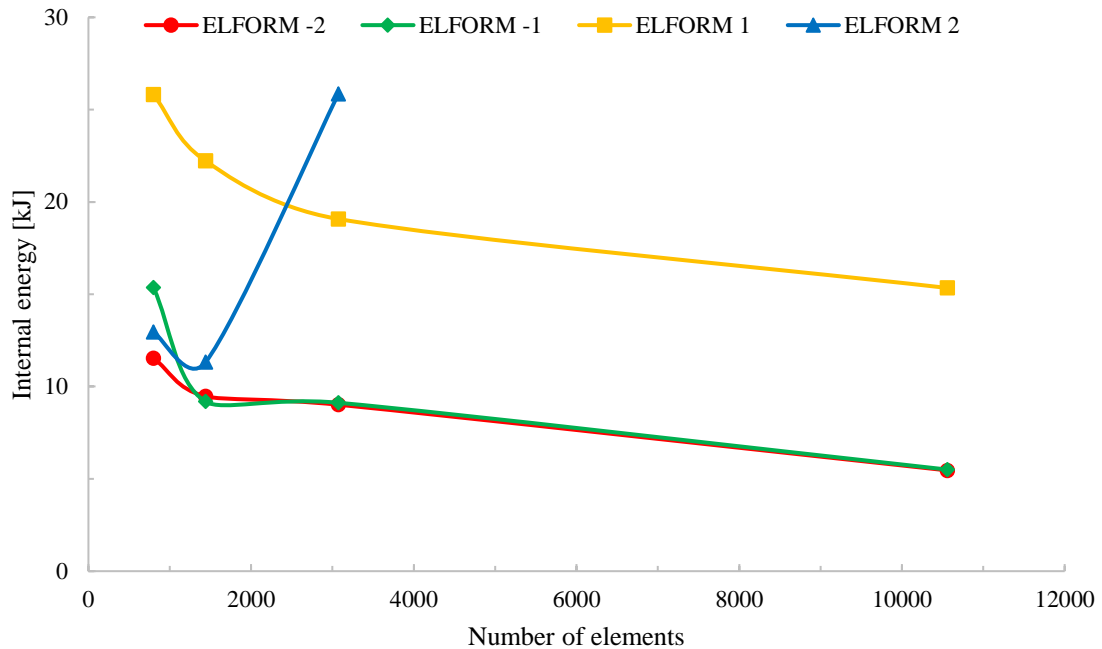
Figure 3-16: Effect of element formulation type on the internal energy and number of elements

After the selection of element formulation type (ELFORM), a parametric study for optimizing the most suitable element size was done for different five element sizes; 5, 4, 3, 2, 1 mm^3. 250 m/s constant speed was impacting the models. Slipping force-stroke curves obtained from this study are presented in Figure 3-17. Table D.2 (Appendix D) represents the deformation history for the five studied element sizes.

The obtained results can be summarized in Table 3-13. It can be concluded that the internal energy of the model is decreasing with the increasing in number of elements and this can be referred to the increase in the eroded internal energy with the increase in number of elements. In Figure 3-18 the internal energy and the eroded internal energy with number of elements are shown, it is obvious that at element size = 1 mm^3 the internal energy is approximately equal to the eroded internal energy, on the other hand, 1 mm^3 element size
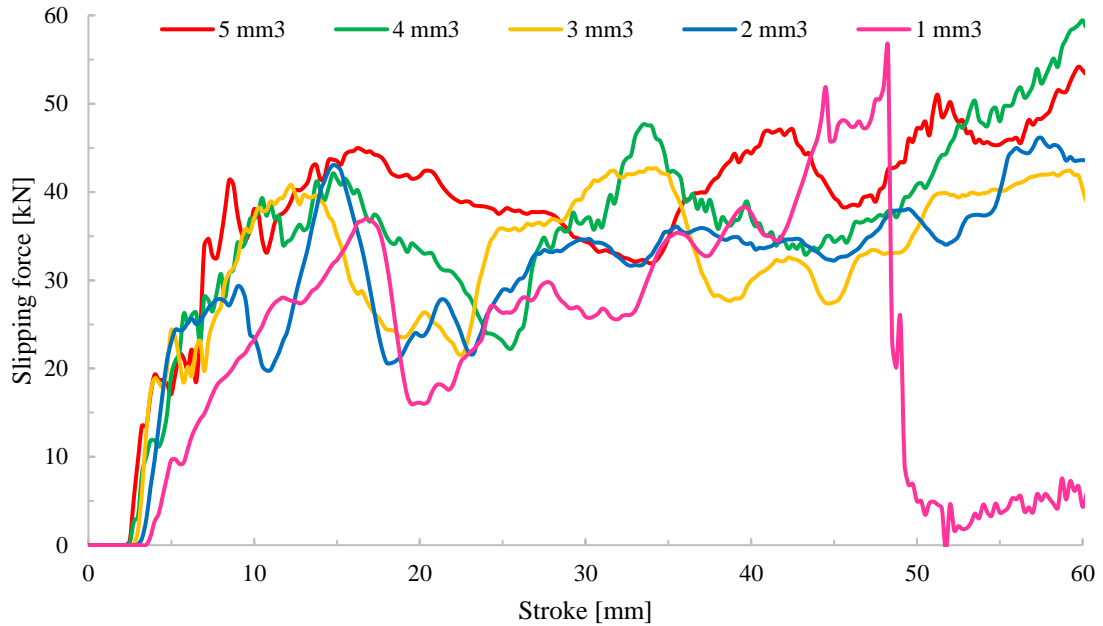
Figure 3-17: Effect of element size on slipping force-stroke curves

cannot be selected for this model because of its non-reasonable computational time compared to other element sizes, and the unjustified contact losses between the elements at the end of the solution. Otherwise, element size = 2 mm^3, showed very good results in Slipping force-stroke curve and the deformation behavior of the conical tube.

Table 3-13:Summary for the results of mesh optimization parametric study

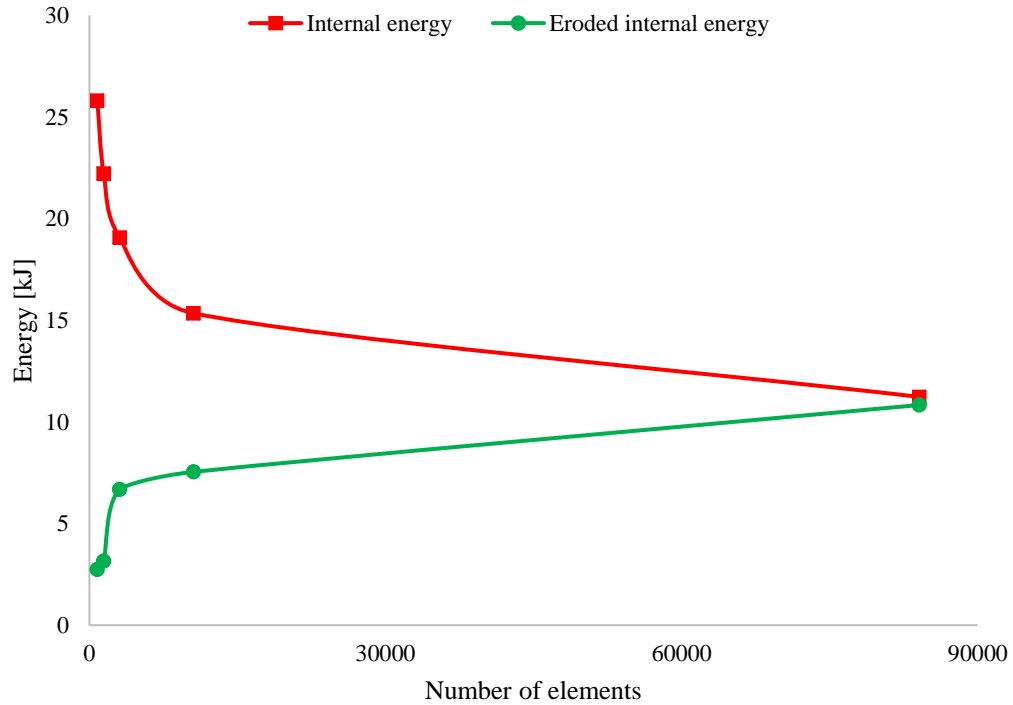| Element size	No. of elements	No. of nodes	Internal energy	Eroded internal energy	CPU time
1 mm^3	84096	96480	11.23 kJ	10.83 kJ	170359 s
2 mm^3	10560	13296	15.34 kJ	7.54 kJ	14445 s
3 mm^3	3072	4256	19.08 kJ	6.68 kJ	2372 s
4 mm^3	1440	2232	22.23 kJ	3.16 kJ	75 s
5 mm^3	800	1300	25.81 kJ	2.75 kJ	37 s

Figure 3-18: Internal energy and eroded internal energy VS number of elements.

3.2.5 Parametric study for MAT_054

A parametric study was performed for MAT_054, to determine the failure modelling parameters for this material model. A baseline values were considered for all the trials with one parameter change each time. Table D.3 (Appendix D) summarizes the values that were used in this study for each parameter. Results for these failure modelling parameters are shown in Appendix D. From this parametric study, the most effective parameters are YCFAC and failure strain limits; DFAILM, DFAILS and DFAILC.

3.2.6 Parametric study for crushing test speed

A parametric study was performed to check the effect of the crushing test speed on the model (Table 3-14). Big variations were observed.

Table 3-14: Parametric study for the crushing test speed

Test speed [mm/ms]	Displacements [mm]	Termination time [ms]	Time step [ms]	No. of steps
2.5	100	40	0.1	402
25	100	4	0.01	402
100	100	1	0.025	402
250	100	0.4	0.001	402

The quasi-static sliding test was performed with a velocity of 15 mm/min (0.00025 m/s). This low crushing speed is very costly to simulate. Since no strain rate dependent parameters are defined for the material failure model, the only dynamic factors that affects the model are vibration and wave propagation while increasing the crushing speed. To overcome this issue, damping parameters are defined, thus the effect of high crushing speed can be neglected. However, results in Figure 3-19 have differences, the highest crushing speed (250 m/s) has the highest response, and the lowest crushing speed (2.5 m/s) has the lowest response. It can be concluded from Table 3-15, that increasing the crushing speed will reduce the computational time with good simulation results.
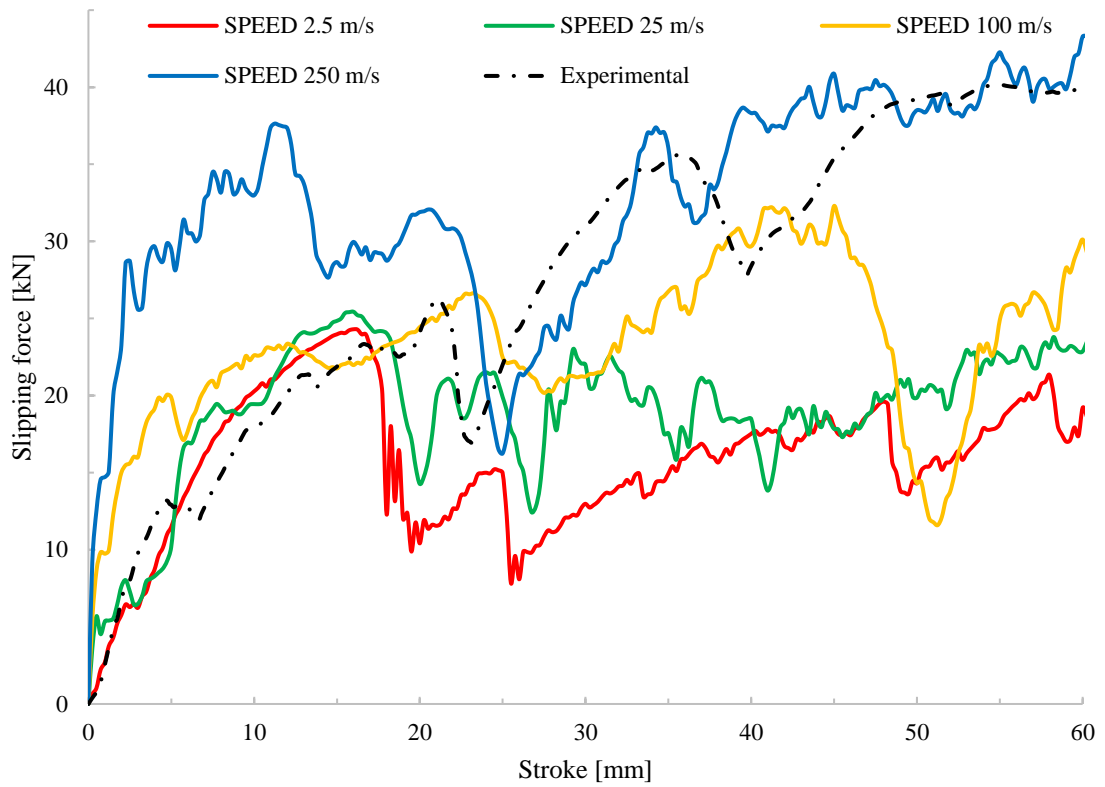
Figure 3-19: Correlation between experimental and numerical crushing speed for 45°
CFRP BGP

Table 3-15: Effect of crushing speed on CPU time

Crushing speed [m/s]	CPU time [s]
2.5	7247
25	1297
100	44
250	36

3.3 Summary

In this chapter, the experimental and the finite element simulation program were employed to achieve the objectives of this research. Both the vacuum infusion and filament winding fabrication processes of the experimental program were described in details. The flat and curved body armor plates were fabricated by vacuum infusion process, while the bullet guiding pockets were fabricated using filament winding process. In the finite element program, ANSYS/LS-DYNA software was used to model the FEM. Parametric study has been performed to optimize element type, mesh size, material failure parameters and crushing speed. The optimized finite element model was validated against the experimental results, in which an excellent agreement was achieved. In the next chapter, effect of materials stacking sequence on ballistic behavior of fabricated body armor plates will be presented and discussed in details. In addition, the effect of conical angle on the sliding crush behavior of the bullet guiding pockets will be examined and discussed. Furthermore, the new bullet guiding pocket armor plate will be developed and modelled based on the results from ballistic real shooting and quasi-static sliding crush tests.

CHAPTER 4

RESULTS AND DISCUSSION

In this chapter the results of phase-I including the effect of material sequence and geometrical configuration on the ballistic behavior of hybrid body armor plates will be presented and discussed in details. To this end, three types of fibers and plates with two configurations have been employed. The fibers used are carbon fiber, Kevlar fiber and date palm fiber, while the plate configurations are flat plate and curved plate. In phase II, the effect of conical angles on the quasi-static crushing behavior of bullet guiding pockets will also be presented and discussed. The findings of these phases will be used to develop the bullet guiding pocket body armor plate. The results of the bullet guiding pocket armor plate will be presented and discussed in Phase III.

4.1 Ballistic Behavior of Flat and Curved Body Armor Plates

4.1.1 Effect of material stacking sequence: experimental investigation

To find the optimum material sequence for hybrid body armor plates, four material sequences have been used to test their ballistic behavior. The ballistic behavior was carried out by utilizing the Qatari internal security forces (LEKHWIYA) facilities. The tests were performed on non-hybrid $[KFRP]_{40}$, hybrid $[CFRP_4/KFRP_6]_4$, hybrid $[CFRP_{10}/KFRP_{30}]$ and $[CFRP_4/[DPRP_2/KFRP_{10}]_3]$. The ballistic test was done in an open space with 15 m away from the body armor plates. The 9 mm FMJ RN bullet was used for all the samples, with an initial impact speed of 398 m/s according to NIJ standard [80]. The main aim of these tests is to examine the ballistic behavior of flat and curved body armor plates. Accordingly, the back-face signature (BFS) will be measured for each body armor plate.

This will indicate, whether the body armor plate stopped the bullet or not as stated in Section (2.4.3). In that manner, Figure 4-2 presents the strike face and back face pictures for the tested body armor plates.

From these ballistic tests, it can be observed that non-hybrid $[KFRP]_{40}$ body armor plate and hybrid $[CFRP_{10}/KFRP_{30}]$ body armor plate succeeds to stop the bullet and no complete penetration was observed. While a complete penetration was observed for $[CFRP_4/KFRP_6]_4$ body armor plate. This can be referred to the carbon fiber layers that were in-between the Kevlar layers. Although carbon fiber has good strength-to-weight ratio, its ballistic properties are weak compared to Kevlar. In Figure 4-1-a, the bullet takes a path inside the non-hybrid $[KFRP]_{40}$ body armor plate and was arrested by the Kevlar fiber layers. Similar behavior was observed for the plate with non-hybrid $[KFRP]_{40}$ body armor plate in all three trials. In contrast, the $[CFRP_4/[DPRP_2/KFRP_{10}]_3]$ hybrid body armor plate has showed different ballistic properties with respect to the three trials. The plate was observed to succeed in the first two trials, in which a partial penetration was observed, while the bullet is completely stopped between the layers. But the $[CFRP_4/[DPRP_2/KFRP_{10}]_3]$ hybrid body armor plate failed to stop the bullet and complete penetration was observed in the third trial. Based on the criterion, the $[CFRP_4/[DPRP_2/KFRP_{10}]_3]$ hybrid body armor plate is considered to fail the ballistic test as shown in Figure 4-1-b. It is worth to mention that the involvement of natural fiber is very interesting, since it is very cheap. The fail in trial three can be easily attributed the random distribution of natural fibers and its critical length. Therefore, using natural fiber in body armor needs more investigation.

| (a) Path of the stopped bullet in the non-hybrid [KFRP]$_{40}$ plate | (b) Stopped bullet inside the [CFRP$_4$/[DPRP$_2$/KFRP$_{10}$]$_3$] plate |

Figure 4-1: Deformed plates after real shooting test

It is worth to mention that the deformation of the bullet in the hybrid [CFRP$_{10}$/KFRP$_{30}$] body armor plate was more than the bullet's deformation in the non-hybrid [KFRP]$_{40}$ plate. It is also very important to mention that the ballistic behavior of the plate and curved plate is found to be similar. But in the case of the curved body armor plate, it is more compatible with the human's torso which gives the soldier more comfort while wearing it. Table 4-1 summarizes the results obtained from the ballistic test on all the plates, each plate type has been tested on 3 samples of plates and 3 shooting trials per plate.

Table 4-1: Results of ballistic tested body armor plates

Plate type	Sample ID	Shot ID	PASS	FAIL	BFS
Flat non-hybrid [KFRP]$_{40}$ plate	1	1	✓		20 mm
		2	✓		24.3 mm
		3	✓		22.5 mm
	2	1	✓		26.9 mm
		2	✓		21.5 mm
		3	✓		26.5 mm
	3	1	✓		23.5 mm
		2	✓		22.3 mm
		3	✓		33.5 mm

Plate					
Curved non-hybrid [KFRP]$_{40}$ plate	1	1	✓		27.2 mm
		2	✓		22.5 mm
		3	✓		29.8 mm
	2	1	✓		21 mm
		2	✓		24.8 mm
		3	✓		32.7 mm
	3	1	✓		26.8 mm
		2	✓		31.1 mm
		3	✓		35 mm
Flat hybrid [CFRP$_4$/KFRP$_6$]$_4$ plate	1	1		✕	NA*
		2	✓		36.1 mm
		3	✓		42 mm
	2	1		✕	NA*
		2		✕	NA*
		3	✓		35.3 mm
	3	1		✕	NA*
		2	✓		41.9 mm
		3	✓		37 mm
Curved hybrid [CFRP$_4$/KFRP$_6$]$_4$ plate	1	1	✓		39 mm
		2		✕	NA*
		3	✓		40.2 mm
	2	1		✕	NA*
		2		✕	NA*
		3	✓		43.2 mm
	3	1		✕	NA*
		2		✕	NA*
		3	✓		39.8 mm
Flat hybrid [CFRP$_{10}$/KFRP$_{30}$] plate	1	1	✓		26.2 mm
		2	✓		26 mm
		3	✓		32 mm
	2	1	✓		21.3 mm
		2	✓		22.5 mm
		3	✓		23.4 mm
	3	1	✓		23 mm
		2	✓		27.9 mm
		3	✓		24.5 mm
Curved hybrid [CFRP$_{10}$/KFRP$_{30}$] plate	1	1	✓		33.3 mm
		2	✓		29.2 mm
		3	✓		31.5 mm

	2	1	✓		24.2 mm
		2	✓		26.7 mm
		3	✓		21 mm
	3	1	✓		25.1 mm
		2	✓		22.2 mm
		3	✓		25.9 mm
Flat [CFRP$_4$/[DPRP$_2$/KFRP$_{10}$]$_3$] plate	1	1	✓		38.2 mm
		2	✓		40.5 mm
		3		×	NA*
	2	1	✓		41 mm
		2		×	NA*
		3		×	NA*
	3	1		×	NA*
		2		×	NA*
		3		×	NA*

NA*: Non-applicable (Complete penetration)

(a) Flat non-hybrid [KFRP$_{40}$] plate, sample #1, shot #1

(b) Curved non-hybrid [KFRP$_{40}$] plate, sample #2, shot #1

FAILED
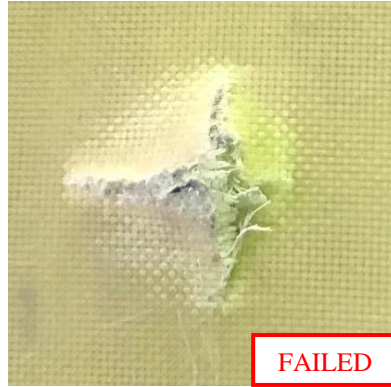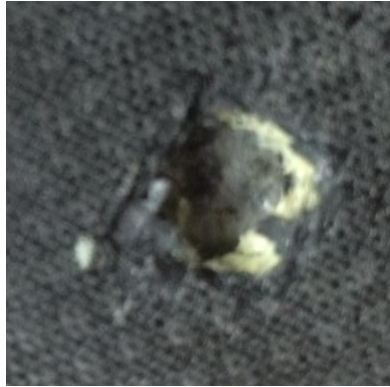
(c) Flat hybrid [CFRP$_4$/KFRP$_6$]$_4$ plate, sample #1, shot #1

FAILED
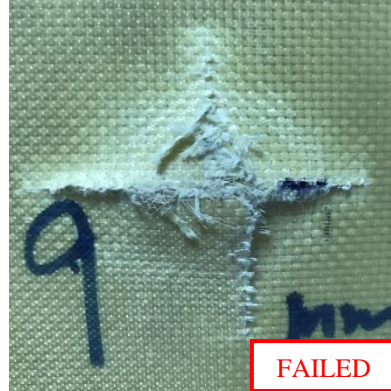
(d) Curved hybrid [CFRP$_4$/KFRP$_6$]$_4$ plate, sample #3, shot #1

PASSED
BFS=26.2mm
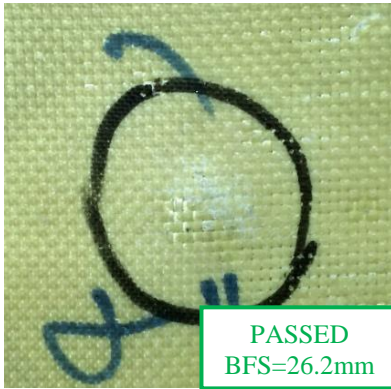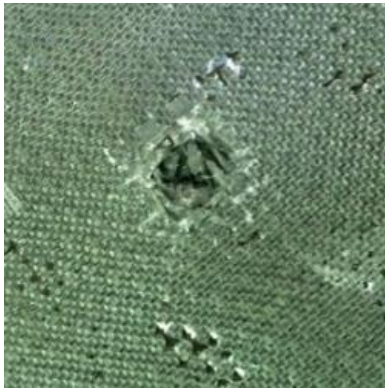
(e) Flat hybrid [CFRP$_{10}$/KFRP$_{30}$] plate, sample #1, shot #1

(f) Curved hybrid [CFRP$_{10}$/KFRP$_{30}$] plate, sample #2, shot #1
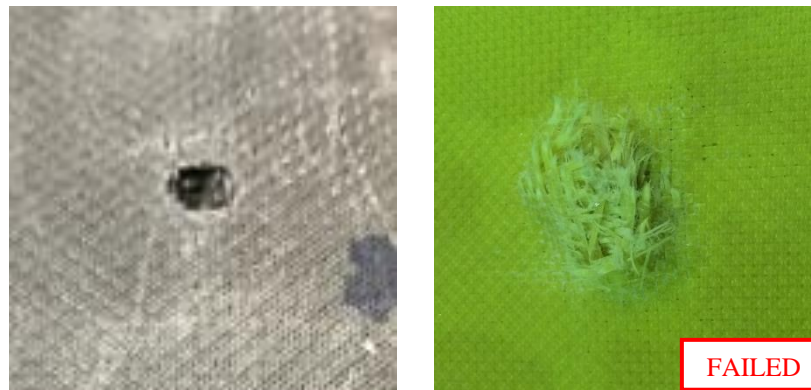
(g) Flat [CFRP$_4$/[DPRP$_2$/KFRP$_{10}$]$_3$] plate, sample #3, shot #1

Figure 4-2: Strike-face and back-face for the ballistic tested body armor plates

4.1.2 Energy dissipation mechanism of armor plates

4.1.2.1 Macro-energy dissipation mechanism of armor plates

Body armor plate has main four categories in encountering the bullet and dissipating the bullet's kinetic energy on the macro level:

1. **Deformation of the fabric**; as the bullet hits the composite armor plate layers, the layers start to bend to cause deformation. After fabric deformation, matrix cracking occurs to cause fiber debonding and breakage. At this point the energy from the bullet is dissipated and the composite layers start to absorb some of this energy by deforming the layers. In the non-hybrid [KFRP]$_{40}$, the first layers of KFRP faced

the striking bullet, the matrix has cracked, fiber debonding and breakage have occurred. The bullet continued to deform and penetrate the KFRP till its kinetic energy was dissipated through the layers. In the hybrid [CFRP$_4$/KFRP$_6$]$_4$ plate, the bullet has bent the four facing layers of CFRP, these layers were deformed after the matrix cracking and fiber breakage. On the other hand, the next six layers were supporting the armor plate from penetration coming from the bullet's kinetic energy. Although these layers were trying to avoid penetration, but the matrix cracking, fiber breakage and deformation in fabric, made them easy to penetrate. Same mechanism occurred for the next CFRP and KFRP layers to end up with complete penetration. In case of the hybrid [CFRP$_{10}$/KFRP$_{30}$] plate, the ten CFRP tend to bend then deform due to the impact from the bullet to cause penetration due to the matrix cracking and fiber breakage. The KFRP will act as a support like in the hybrid [CFRP$_4$/KFRP$_6$]$_4$ plate, but the thirty layers were enough to arrest the bullet between them.

2. **Fabric destruction**; while the bullet is penetrating the composite layers, the fabric is deformed, as mentioned before, to cause finally a destruction of the fabric, which means a complete failure in the layer. As the first layer failed; delamination occurs between layers, especially in case of two different materials, due to the coefficient of mutual influence, as out-of-plane shear strains to in-plane shear and normal stresses can be observed. $\eta_{i,ij}$ and $\eta_{ij,i}$ are the first and second coefficients of mutual influence which are defined in Equations (4.1) and (4.2).

$$\eta_{x,xy} = \frac{\varepsilon_x}{\gamma_{xy}}, for\ \tau_{xy} = \tau \qquad (4.1)$$

$$\eta_{xy,x} = \frac{\gamma_{xy}}{\varepsilon_x}, for \ \sigma_x = \sigma \tag{4.2}$$

Where $\eta_{x,xy}$ is the coefficient of mutual influence caused by shear in the xy-plane, $\eta_{xy,x}$ is the coefficient of mutual influence caused by normal stress in x-direction, ε_x is the axial normal strain, γ_{xy} is the in-plane engineering shear strain, τ_{xy} is the in-plane shear stress, and σ_x is the normal stress.

3. **Thermal energy**; some of this bullet's kinetic energy is transferred into thermal energy because of the friction between the bullet and fibers, a high thermal expansion coefficient (α) means more heat energy absorb by the material which means more deformation between the composite layers. Although, Kevlar and carbon fiber are resistant to very high temperatures, the destruction in Kevlar will be more than carbon fiber as α for Kevlar is 3.5 higher than carbon fiber.

4. **Wave propagation**; some energy from the bullet is dissipated as two main waves; transverse wave and longitudinal wave depending on the sound velocity of the material at the point of impact (Figure 4-3). The longitudinal wave travels outward along the fiber axis as per Equation (4.3), to cause stretching in fibers and make an in-plane movement. While the transverse wave deflects the fibers vertically to cause an out-of-plane movement, the transverse wave speed can be calculated from Equation (4.4).

$$c = \sqrt{\frac{E}{\rho}} \tag{4.3}$$

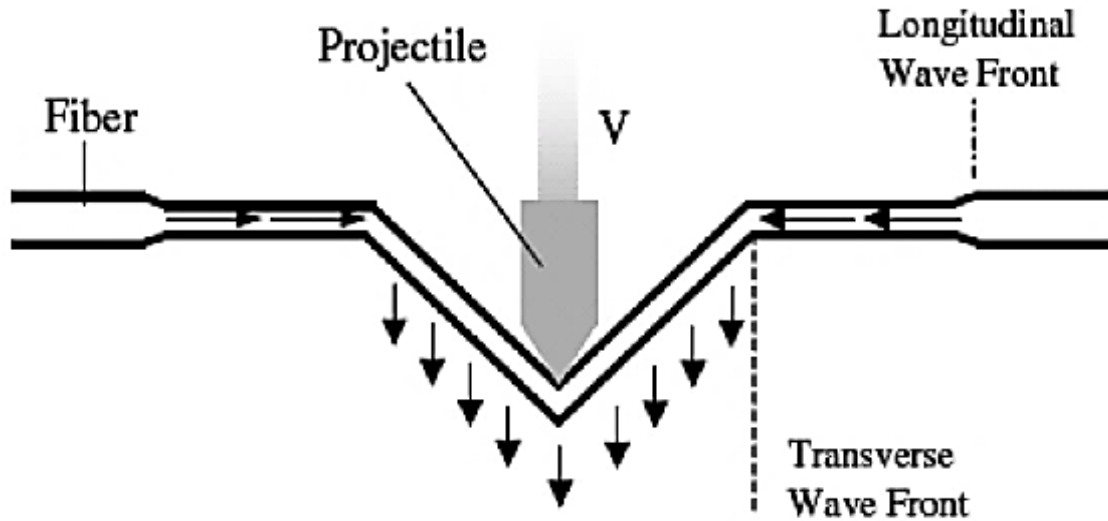$$u = c\left(\sqrt{\varepsilon(1+\varepsilon)} - \varepsilon\right) \tag{4.4}$$

Figure 4-3: Transverse and longitudinal waves resulted in fiber from the bullet

where c is the longitudinal wave speed (m/s), E is material Young's modulus (GPa), ρ is the mass density of the material (kg/mm^3), and ε is the fiber's strain.

4.1.2.2   *Micro-energy dissipation mechanism of armor plates*

Scanning electron microscopy (SEM) analysis was performed on samples taken from the strike faces of hybrid and non-hybrid body armor plates. The SEM was carried out to examine and identify the energy dissipation mechanism of the bullet's kinetic energy through body armor plates at micro level. Figure 4-4 shows SEM images for strike faces of hybrid and non-hybrid body armor plates.

- Figure 4-4-a shows the micro failure mechanisms for non-hybrid [KFRP$_{40}$] body armor plate. As the bullet strikes the face layers, matrix cracking was observed to initiate the kinetic energy dissipation mechanism. This is followed by fiber debonding and fiber breakage. Similar mechanism was observed to occur as the bullet progresses through the rest of layers until the bullet stops at BFS of 20 mm

as shown in Table 4-1. Micro delamination was observed between layers as shown in Figure 4-4-a.

- Figure 4-4-b presents the SEM image for $[CFRP_4/KFRP_6]_4$ body armor plate, in which the first four CFRP layers are designed to face the strike, while first six KFRP layers are designed to support the CFRP layers and preventing bending of CFRP layers and accelerating the bullet penetration. Bending was observed to dominate the first stage of bullet strike, which delayed the bullet penetration. This results in low energy dissipation. At the end of bending stage, the bullet penetrates the CFRP layers and small energy believed to be dissipated in the form of matrix cracking and delamination between the CFRP layers and KFRP layers. The rest of the kinetic energy is dissipated in form of KFRP fiber breakage and significant destruction on KFRP observed. This results in complete penetration of the plate. Existence of CFRP layers between the KFRP increases the deformation throughout the entire plate thickness, which decreases the energy dissipation mechanism in the form of KFRP destruction.

- The results of $[CFRP_4 /KFRP_6]_4$ inspired to develop the new design by placing the CFRP layers at the strike face, while the KFRP layers at the back face of the armor plate. Figure 4-4-c shows SEM image for $[CFRP_{10}/KFRP_{30}]$ body armor plate. As the bullet strikes the CFRP layers, small deformation on CFRP layers was observed, while the KFRP support and prevents the CFRP layers to experience more deformation. This leads to matrix cracking at CFRP layers and accelerates the penetration of the CFRP layers, which results in high energy dissipation. As the bullet progress the KFRP layers start to absorb the kinetic energy of the bullet in

destruction failure mode such as matrix cracking, fiber debonding, fiber breakage and delamination between layers. This was measured to occur until BFS of 26.2 mm at which the bullet was arrested and no complete penetration was observed.

- Figure 4-4-d presents SEM image for the $[CFRP_4/[DPRP_2/KFRP_{10}]_3]$ armor plate. This material sequence has four layers of CFRP at the strike face of the plate, which was penetrated and deformed due to the matrix cracking and fiber breakage. The next two layers of the date palm fiber (DPRP) did not support the previous CFRP due to their weak ballistic properties. The DPRP faced huge matrix cracking, as these fibers were used without treatment. Thus, a small amount of epoxy was absorbed by these fibers in the fabrication process. The next six KFRP layers supported the DPRP, but the bullet's kinetic energy was high enough to penetrate and deform the KFRP, after the matrix cracks and Kevlar fiber breakage. The next two layers of DPRP did not minimize the kinetic energy from the bullet, to cause penetration and deformation in the layers. This mechanism was repeated through the layers to cause complete penetration in the armor plate.

4.1.3   Effect of material stacking sequence: FEM Simulation

The behavior of passed armor plates were simulated using ANSYS/LS-DYNA. Accordingly, simulation of non-hybrid $[KFRP_{40}]$ and $[CFRP_{10}/KFRP_{30}]$ plates will be presented and discussed in this section. The plates were subjected to a 398 m/s impact velocity from a 9 mm FMJ RN bullet according to NIJ standard, similar to the real test [80].
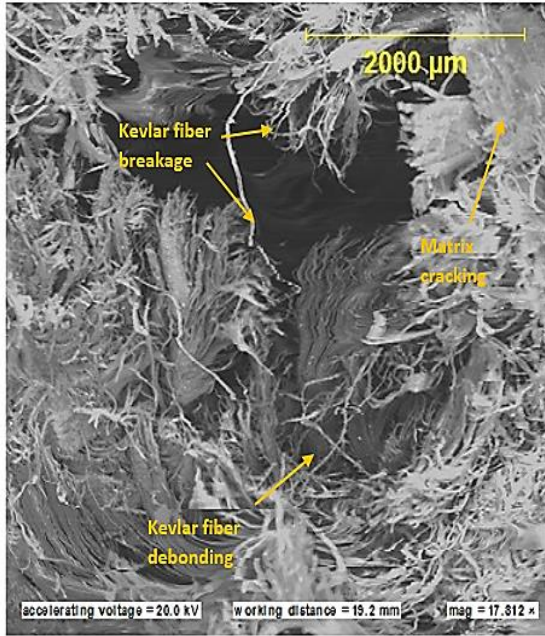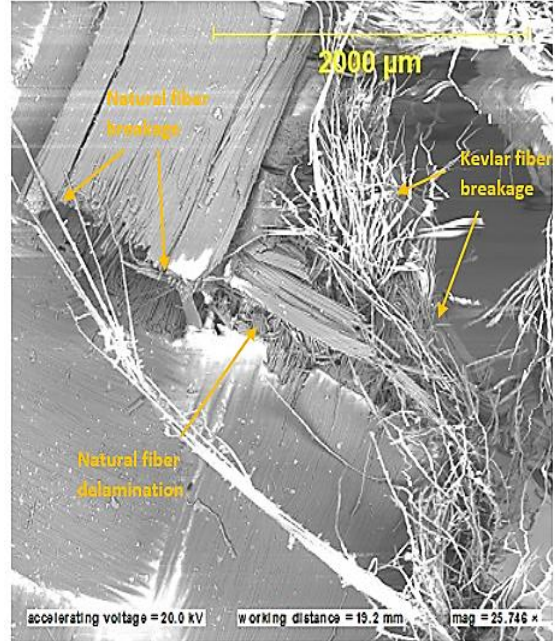
(a) Flat non-hybrid [KFRP$_{40}$] plate, sample #1, shot #1
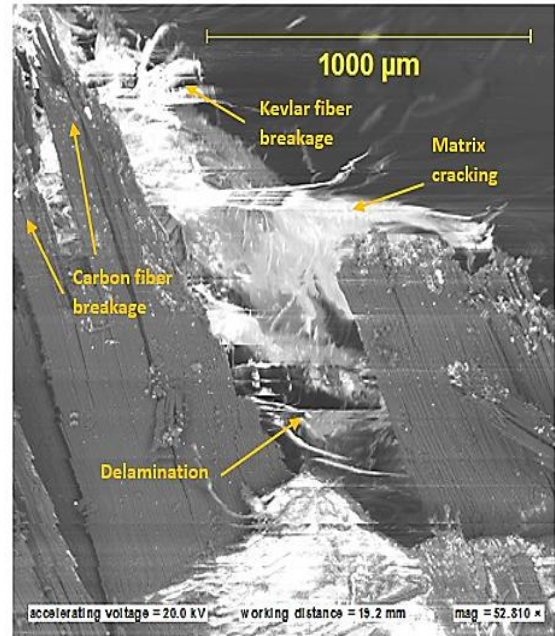
(b) Flat hybrid [CFRP$_4$/KFRP$_6$]$_4$ plate, sample #1, shot #1
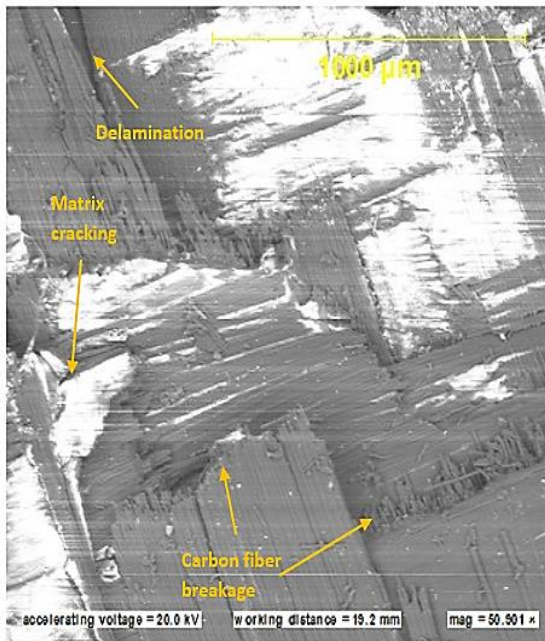
(c) Flat hybrid [CFRP$_{10}$/ KFRP$_{30}$] plate, sample #1, shot #1

(d) Flat hybrid[CFRP$_4$/[DPRP$_2$/KFRP$_{10}$]$_3$] plate, sample #3, shot #1

Figure 4-4: SEM images of strike face for the ballistic tested body armor plates.

Geometrical properties, material modelling, element type and element size optimization and boundary conditions are all presented and discussed in Section (3.2.3). The FEM simulation was carried out at this stage to assure the validity of FEM in simulating the behavior of experimentally tested hybrid body armor plate.

Figure 4-5 shows a comparison between the experimental ballistic test and the FEM simulation of non-hybrid [KFRP$_{40}$] and [CFRP$_{10}$/KFRP$_{30}$] plates. From Equation (2.4), the kinetic energy of the bullet can be calculated. A 9 mm FMJ RN bullet has an approximate mass of 8 grams and the impact velocity of the bullet is 398 m/s. Thus the kinetic energy of the bullet is 633 J. It can be noticed that for non-hybrid [KFRP$_{40}$] body armor plates, the bullet had stopped at 22.5 mm displacement in layer number 29 repsenting the back-face signiture for non-hybrid [KFRP$_{40}$] body armor plat as shown in Table 4-2. For the hybrid [CFRP$_{10}$/KFRP$_{30}$] body armor plate, the bullet computed to be stopped at 36.8 mm displacement in layer number 37. Both back-face signature values (i.e. 22.5 and 36.8 mm) are acceptable according to NIJ standard [80] which defines back-face deformation till 44 mm as shown in Section 2.4.3). Figure 4-6 shows bullet kinetic energy versus back face signature for hybrid [CFRP$_{10}$/KFRP$_{30}$] and non-hybrid [KFRP$_{40}$]. It can be seen clearly that the back face signature for [KFRP]$_{40}$ is significantly less than [CFRP$_{10}$/KFRP$_{30}$]. The effect of CFRP layers has dominated the behavior of the kinetic energy until BFS of 10 mm, then after the domination is for KFRP layers. It is also computed that the CFRP layers cause the bullet tip to be highly deformed compare with the KFRP as shown in Table 4-2.

(a) Strike face for non-hybrid [KFRP$_{40}$] armor plate; numerical and experimental top view

(b) Strike face for hybrid [CFRP$_{10}$/KFRP$_{30}$] armor plate; numerical and experimental top view
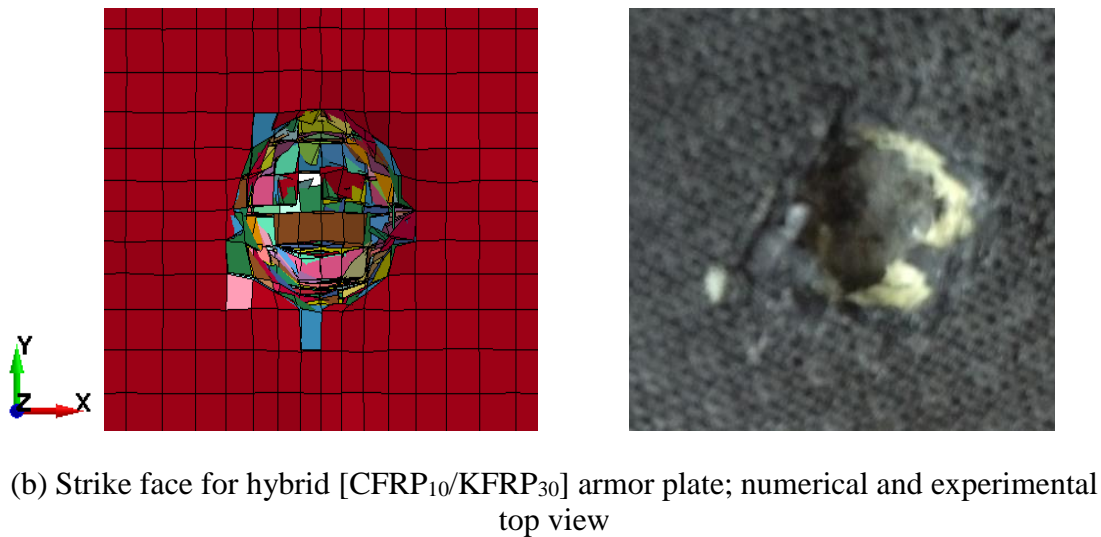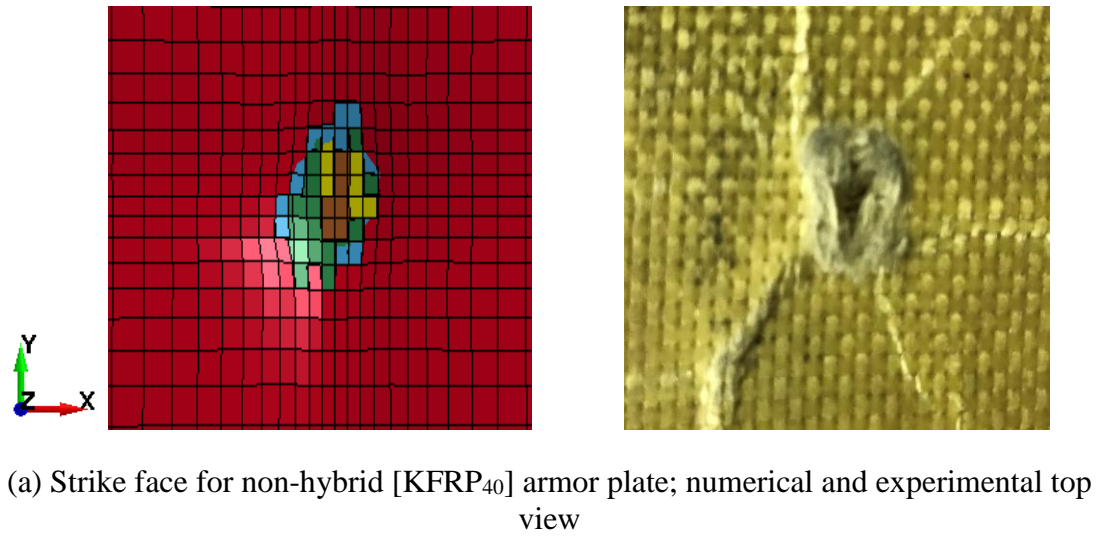
Figure 4-5: Comparison between experimental and numerical strike faces

As mentioned in Section (3.1.1.3), the CFRP and KFRP bullet guiding pockets were fabricated by filament winding process. The fiber composite has been wound over an ABS plastic five steps [cone-cylinder-cone] mandrel. The fabricated bullet guiding pockets is 150 mm overall length as shown in Figure 4-7. Their outer diameter is constant, while the inner diameter varies with the conical angles, Table 4-3 summarizes the dimensions of one cone step for the five bullet guiding pocket angles. Crashworthiness parameters are

computed and analyzed to determine the optimum angles to be used in designing the bullet guiding pocket.
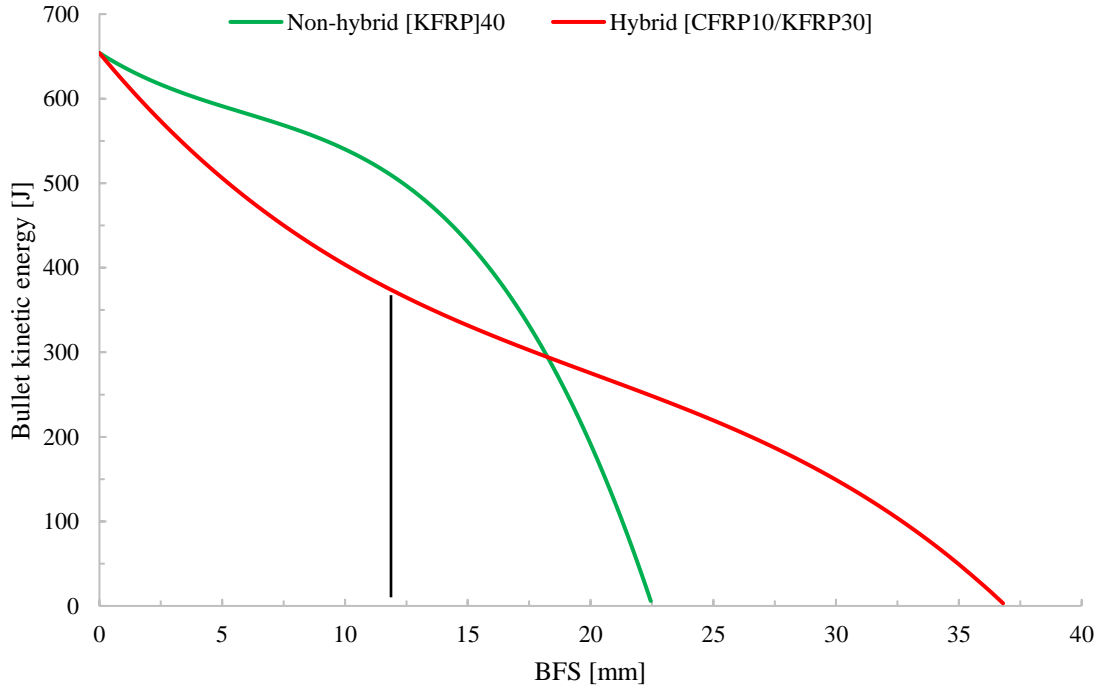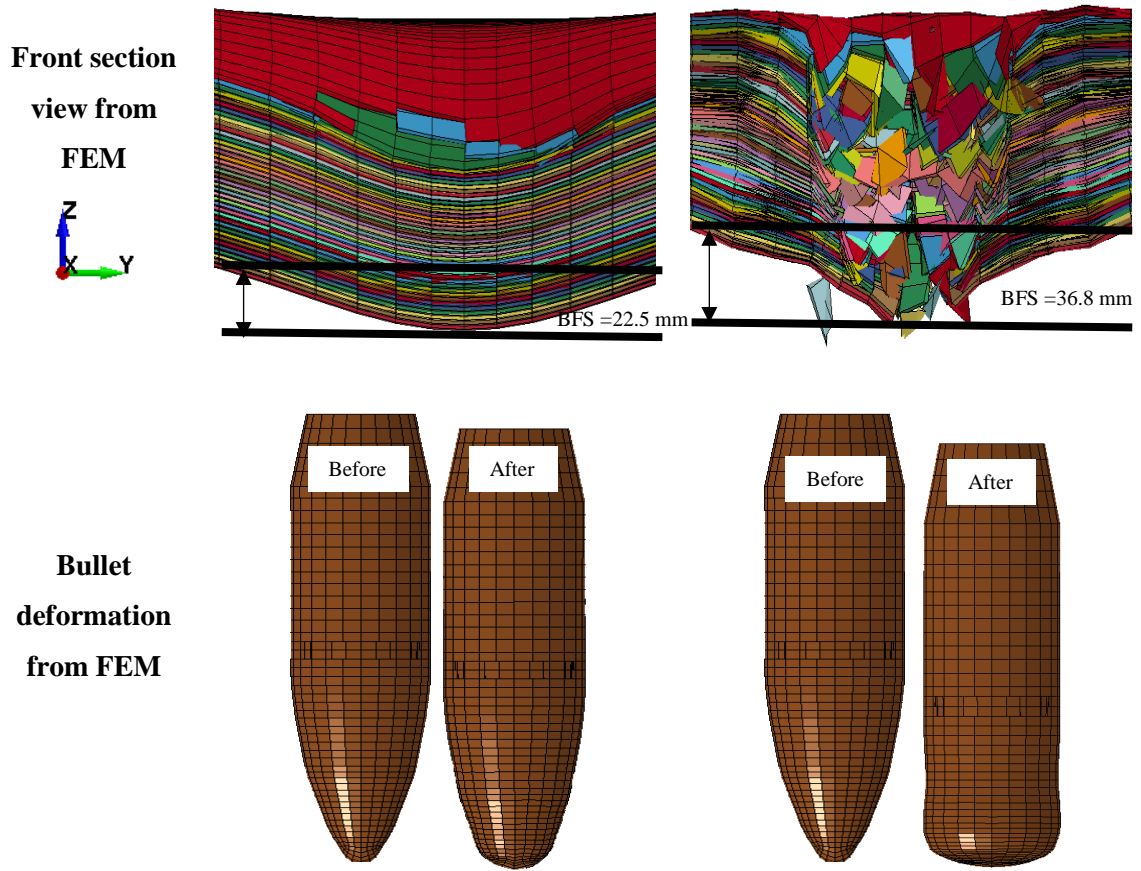

Figure 4-6: Bullet kinetic energy - BFS for non-hybrid [KFRP$_{40}$] and hybrid [CFRP$_{10}$/KFRP$_{30}$] armor plates

Table 4-2: Comparison for back-face signature in non-hybrid [KFRP$_{40}$] and hybrid [CFRP$_{10}$/KFRP$_{30}$] armor plates.

	Non-hybrid [KFRP$_{40}$] armor plate	Hybrid [CFRP$_{10}$/KFRP$_{30}$] armor plate
Experimental BFS	20 mm	26.2 mm
Numerical BFS	22.5 mm	36.8 mm

Front section view from FEM

BFS =22.5 mm

BFS =36.8 mm

Bullet deformation from FEM

Before | After | Before | After

4.2 Ballistic Behavior of the Composite Bullet Guiding Pocket

Based on above results, one can easily see that as the bullet strike the body armor plate, mitigating the bullet in a designed path will result in a very high protection. This can only be made by creating a guiding pocket for the bullet at the face of the body armor. Therefore, the main purpose of this section is to optimize the conical angles for the bullet guiding pocket. Bullet guiding pocket consists of five steps of [cone-cylinder-cone] tubular structures with five different conical angles have been fabricated and tested. Carbon fiber and Kevlar fibers have been employed to fabricate these structures. The test was carried out by slipping a mandrel into the bullet guiding pocket. Accordingly, the mandrel was designed to simulate the bullet. The mandrel dimensions are based on the bullet

dimensions. A quasi static slipping process at speed of 15 mm/min for a stroke of approximately 60 mm was carried out. Force-stroke curves and failure mechanisms for the CFRP and KFRP bullet guiding pockets will be presented and discussed in the next subsections.
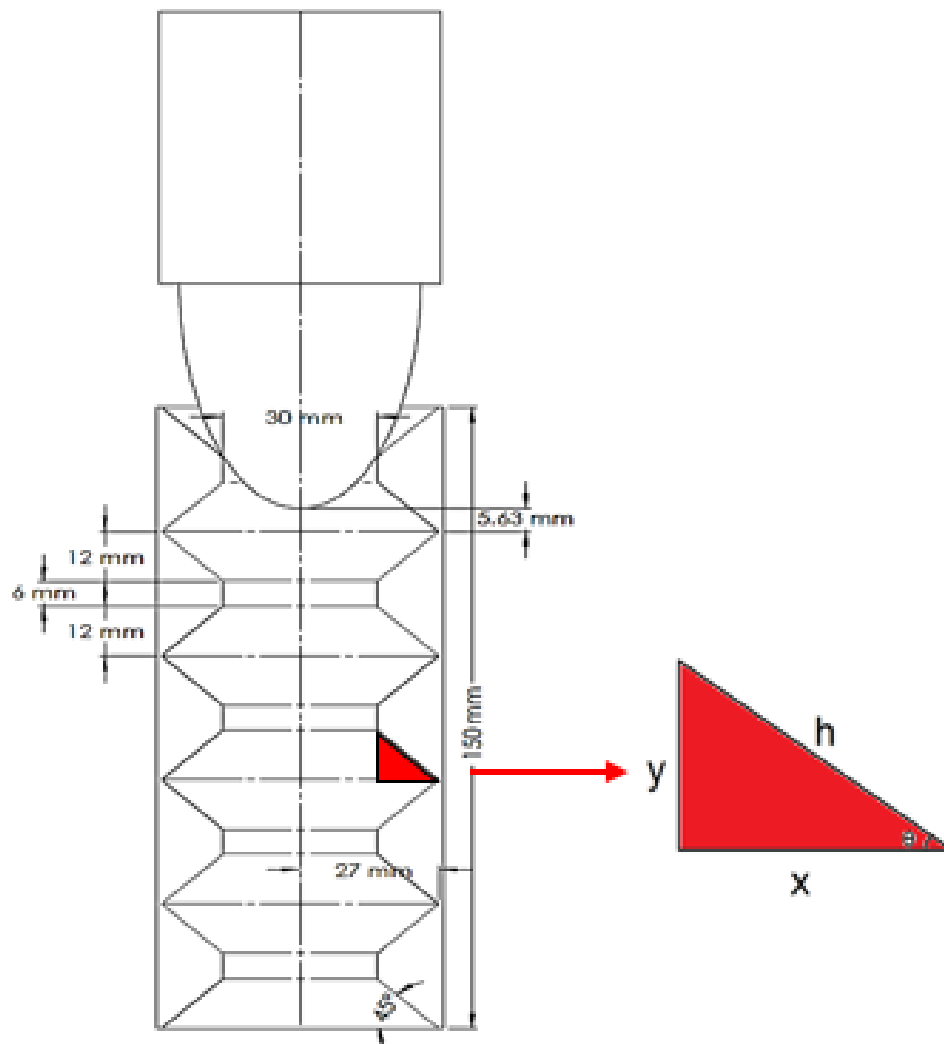

Figure 4-7: Scheme of the bullet guiding pocket sample and the impactor

Table 4-3: Dimensions of one cone step for the five conical angles of BGP

Conical angle (θ)	x [mm]	y [mm]	h [mm]
35°	17.14	12	20.92
40°	14.3	12	18.67
45°	12	12	16.97
50°	10.09	12	15.68
55°	8.4	12	14.65

4.2.1 Crushing response of CFRP BGP

The behavior of the CFRP bullet guiding pocket was divided into two sets based on the appearance of their slipping force-stroke curves and mode of failure. SET-1 associated to the bullet guiding pocket with conical angles of 35° and 40°, while SET-2 associated to the bullet guiding pocket with conical angles of 45°, 50° and 55°. In parallel, simulation of the same has been carried out based on the parametric study that was performed in Sections (3.2.4, 3.2.5 and 3.2.6).

4.2.1.1 SET-1 (conical angle = 35°and 40°)

Figure 4-8 and Figure 4-9 show the slipping force-stroke curves and representative deformation histories obtained experimentally and numerically from crushing the 40° CFRP bullet guiding pocket, respectively. Numerical results showed good agreement with the experimental data. Although the crushing response in the numerical results is less than the experimental crushing response. The first contact line between the tube and the impactor is at 12.7 mm radius of the impactor. Based on the impactor ellipse equation, the impactor head is 20.53 mm inside the geometry as shown in Figure E.2 (Appendix E). The

sliding penetration test starts from this point. Five stages were observed during the test which are discussed as follows:
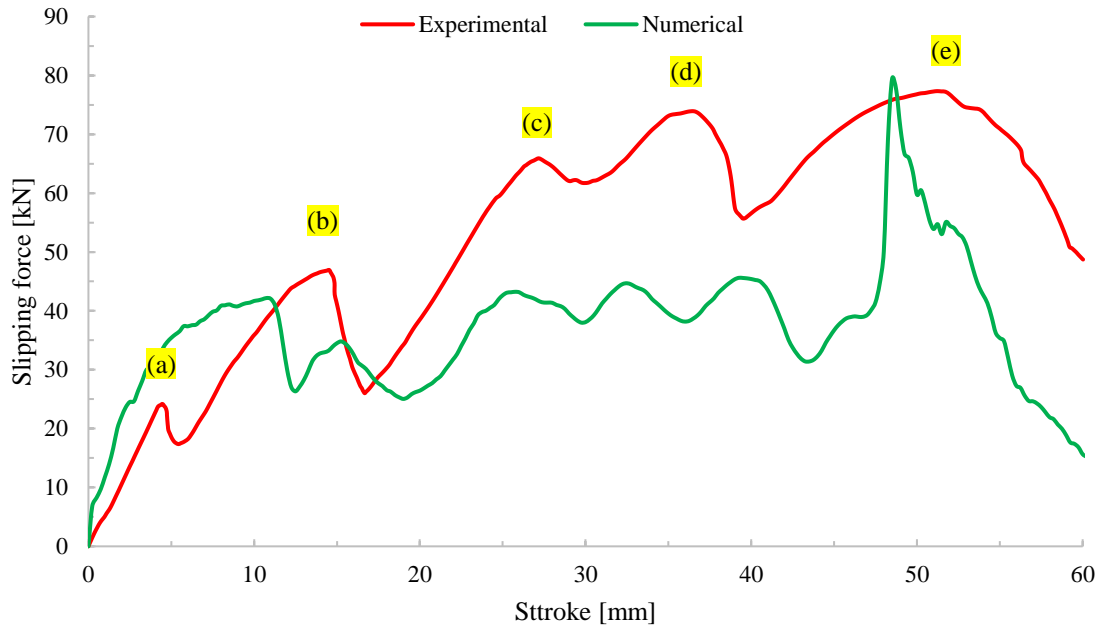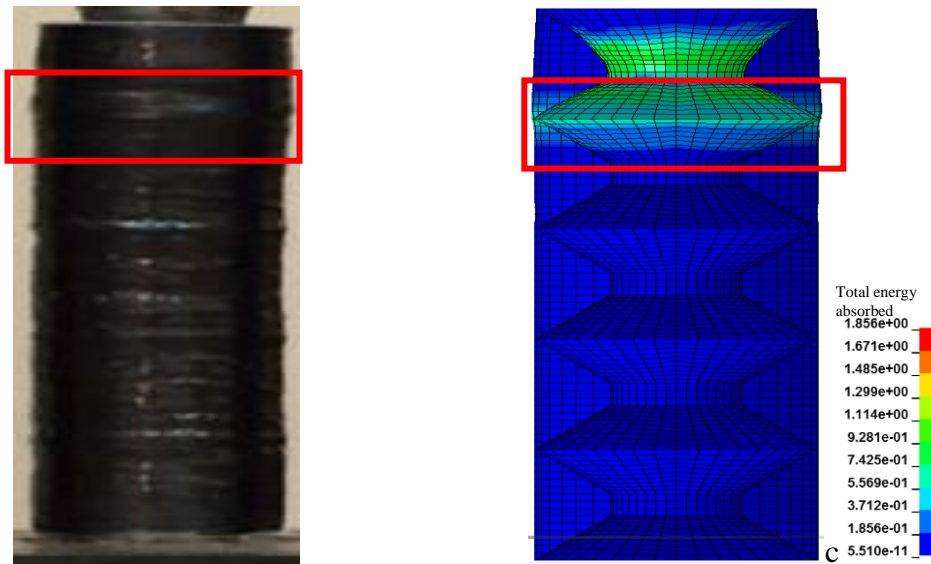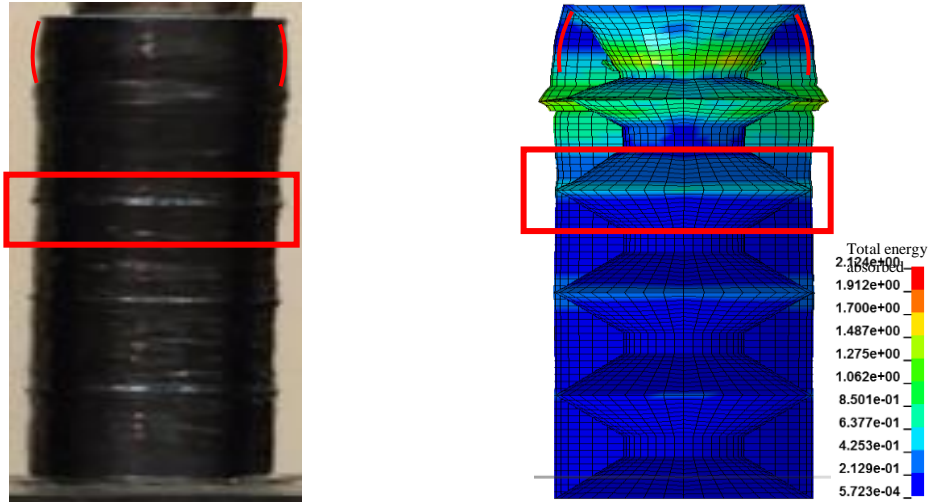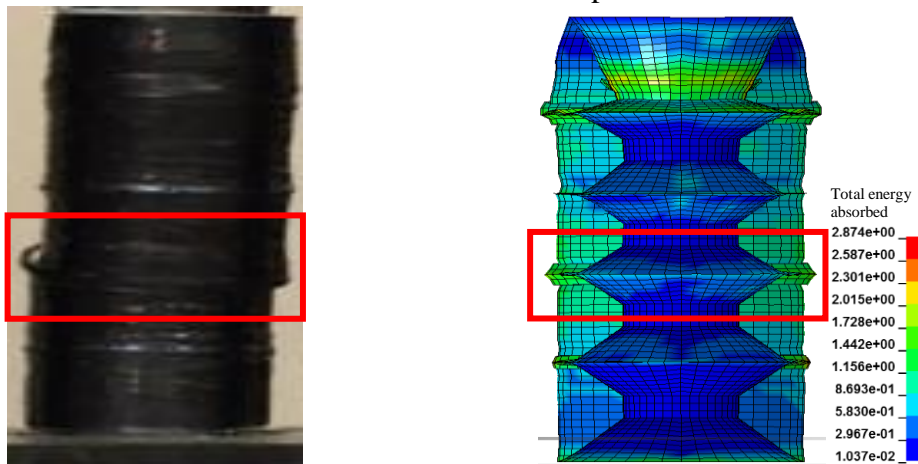

Figure 4-8: Experimental and numerical slipping force-stroke curves for 40° CFRP BGP
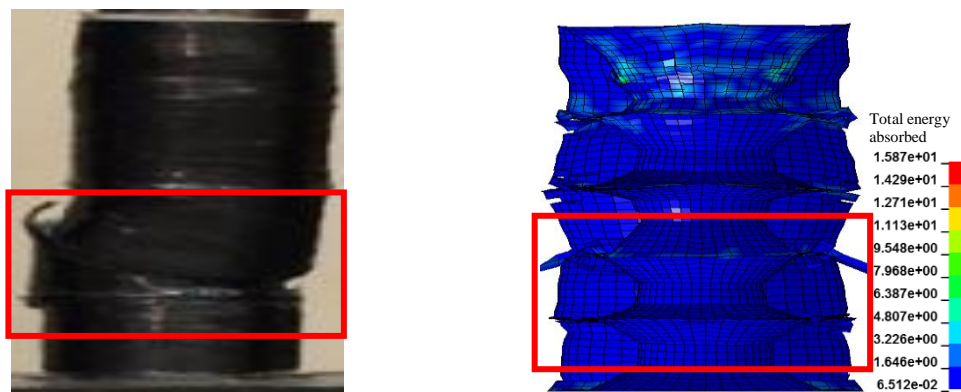

(a) 4.3 mm stroke, Initial matrix cracks and fiber breakage in the first conical step
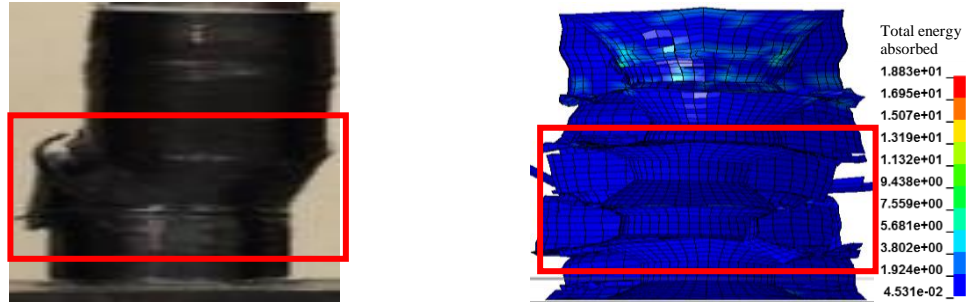
(b) 14.6 mm stroke, Failure in first conical step with matrix cracks and fiber breakage in the second conical step

(c) 27.3 mm stroke, Cracks started at the third conical step with initial slipping

(d) 36.3 mm stroke, Slipping and fiber breakage in the third and fourth conical steps

(e) 51.5 mm stroke, Slipping and contcact loss to end up with tearing in the structure

Figure 4-9: Representative photos during the different five stages of deformation history for the 40° CFRP BGP; experimentally and numerically.

It can be noticed that the slipping force–stroke curve shows a nonlinear relationship between prior to the first crush initiation as depicted in Figure 4-8-a. A sudden drop was observed at the same stroke, where, the crush is initiated. This small drop in slipping force is attributed to matrix cracks that lead to tear the innermost wall layer of the first cone-cylinder-cone step. In the second stage, first recovered in slipping force carrying capacity was achieved to reach its first peak value of 46.52 kN at 14.6 mm as indicated, where the impactor has stuck in the cylindrical face and became as one part with the geometry as shown in Figure 4-8-b. The first transverse shear crack was observed at the second step of [cone-cylinder-cone], which accompanied by a drop in slipping force-stroke which sustained for around 2 mm stroke at a load of 26.2 kN. In the third stage, the crushing force increases gradually to 65.7 kN at 27.3 mm stroke, after which a considerable drop was observed coinciding with the formation of the second crack. The propagation of this transverse shear crack around the third step of [cone-cylinder-cone] is shown in Figure 4-8-c. It was noticed that slipping has started in this stage, due to the low amount of fibers that reinforce the structure and the high value of moment compared to the second step in the conical tube. In the fourth stage, the load has increased till it reached 37.9 kN at 36.3 mm

stroke, the third crack was observed at the fourth step of the geometry (Figure 4-8-d), with more slipping and contact loss in the third and fourth steps. The moment is higher than before which will cause more cracks in the matrix and more fiber breakages. Around 18 kN of load drop occurred at this stage within 3.3 mm stroke. In the fifth stage, the load has increased till to the fifth peak 77.3 kN at 51.5 mm stroke. More slipping, matrix cracks and fibers breakage are presented (Figure 4-8-e). The crushing test was stopped at 60 mm stroke with 49 kN load. Figure 4-10 shows the experimental slipping force-stroke curve for SET-1 (conical angle = 35° and 40°). Almost same behavior was observed for both angles; five failure stages can be seen from the curves. Energy absorbed by 40° CFRP bullet guiding pocket is higher than 35° bullet guiding pocket, which will be discussed later. The numerical results of the 35° CFRP conical tube are presented in Appendix F.
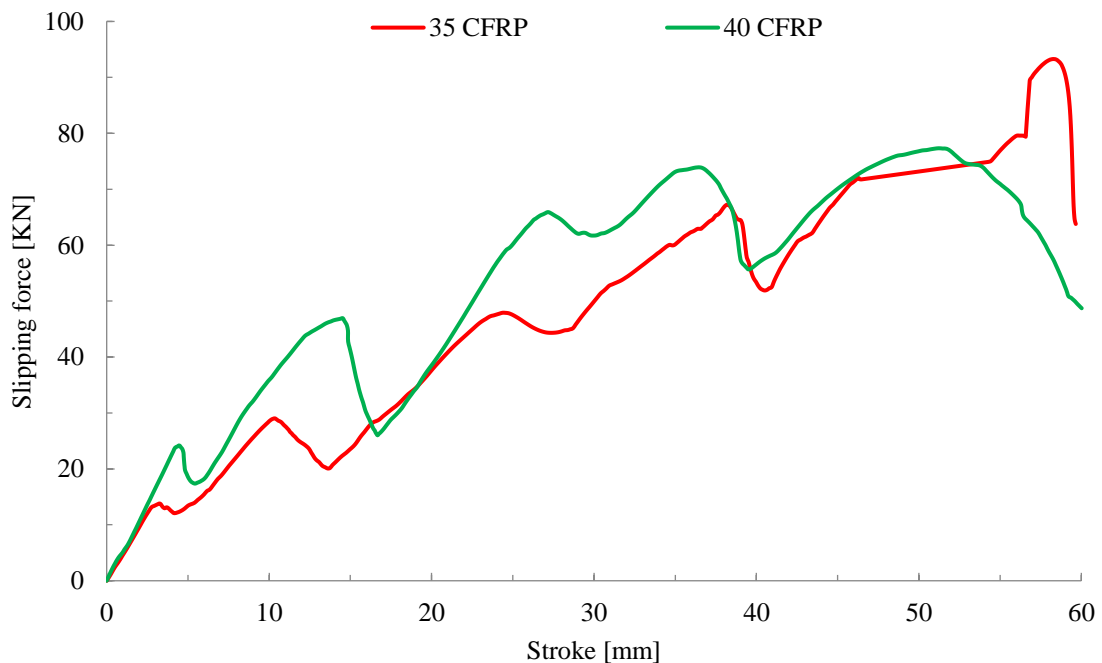

Figure 4-10: Experimental slipping force-stroke curve for SET-1 of the CFRP BGP

4.2.1.2 SET-2 (conical angle = 45°, 50° and 55°)

Figure 4-11 and Figure 4-12 show the typical slipping force-stroke curves and a representative deformation histories obtained experimentally and numerically for CFRP [cone-cylinder-cone] bullet guide pocket with conical angle of 45°. The first contact line between the tube and the impactor is at 15 mm radius of the impactor. Based on the impactor ellipse equation, one can determine the impactor head as 24.37 mm inside the geometry as shown in Figure E.3 (Appendix E). The sliding crush test starts from this point, after which, four stages were observed during the test as follows:
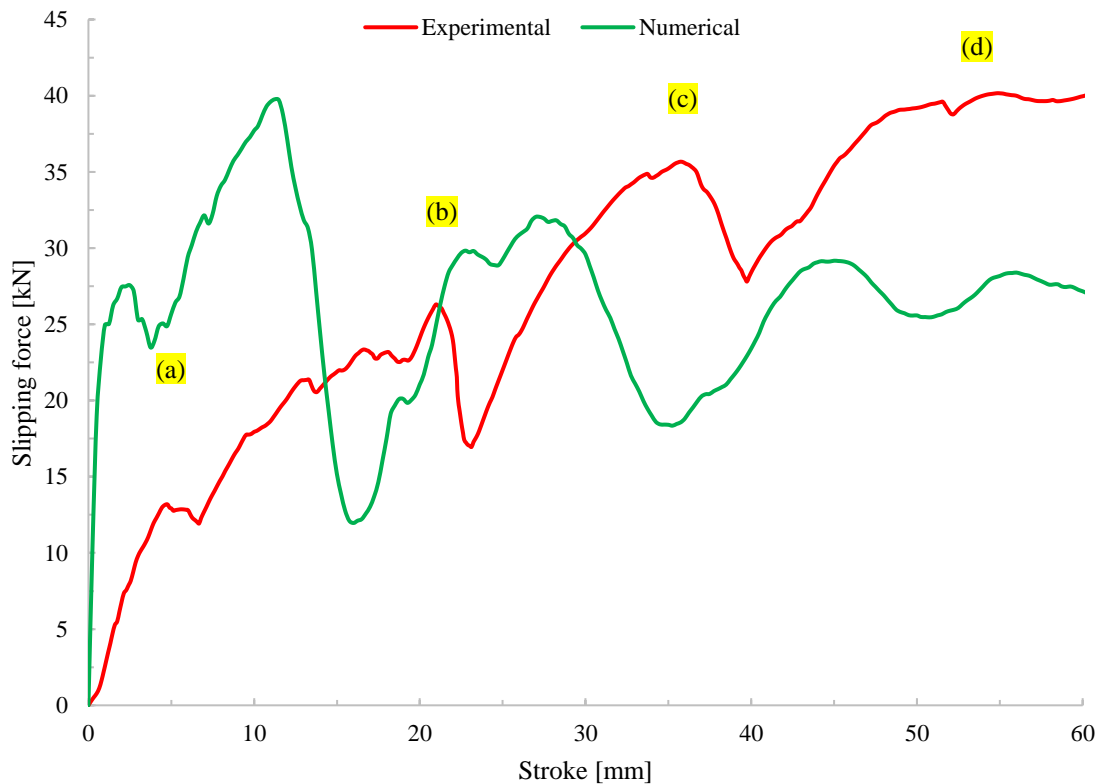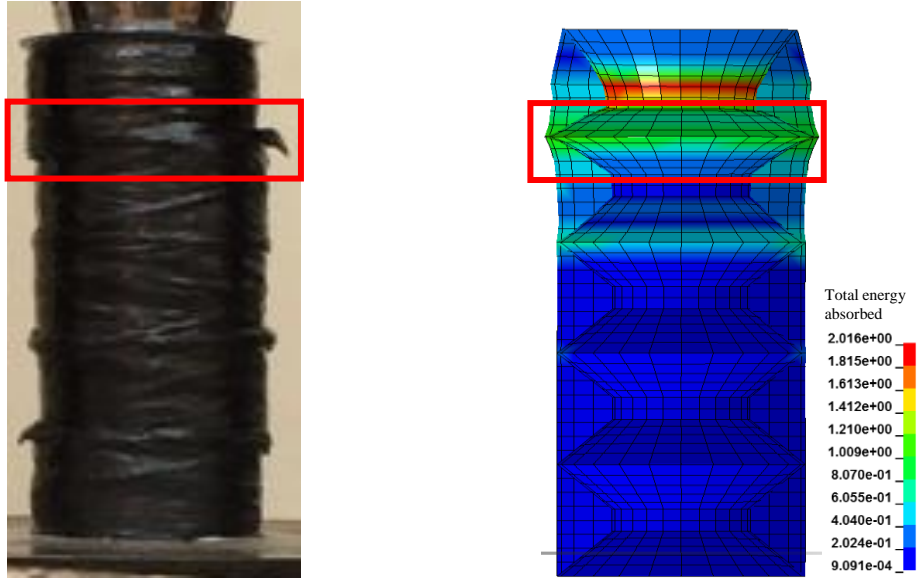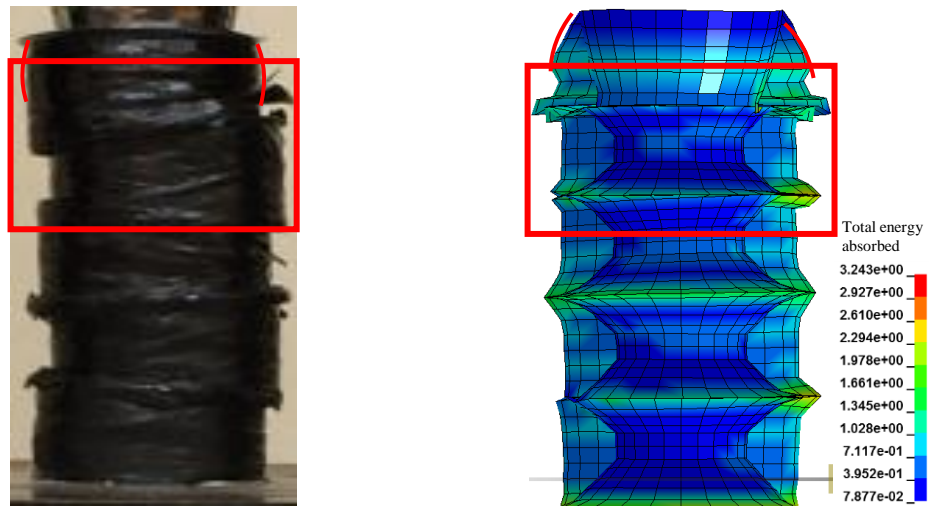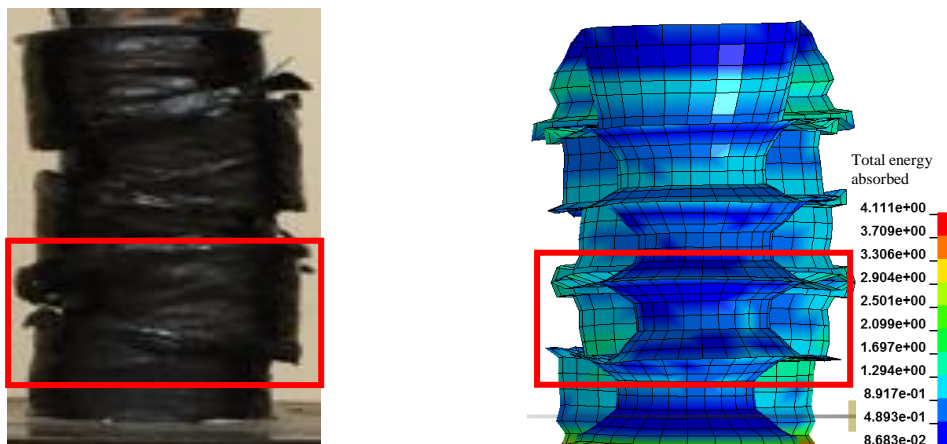

Figure 4-11: Experimental and numerical slipping force-stroke curves for 45° CFRP BGP
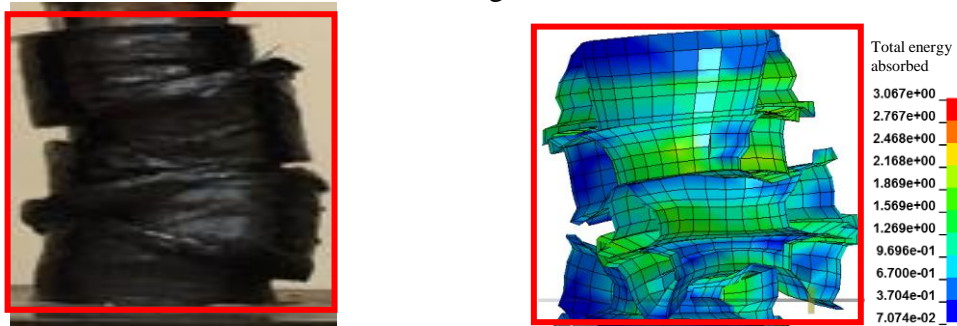
(a) 4.8 mm stroke, Initial fiber breakage in the structure with concentrated stresses at the first conical step

(b) 21.1 mm stroke, slipping in the first conical step and fiber pull-out in the second conical step

(c) 35.9 mm stroke, Slipping and cracks in the third and fourth conical steps with fiber breakage

(d) 54.9 mm stroke, Failure in the whole structure with contact loss

Figure 4-12: Representative photos during the different four stages of deformation history for the 45° CFRP BGP; experimentally and numerically.

In the first stage, the first peak was observed at 4.8 mm stroke and the slipping force measured to be 13 kN. A slight drop occurred at this point and sustained for around 2 mm stroke and the drop in the slipping force was found to be 1 kN. The slight drop in slipping force can be attributed due to the matrix cracks and fibers breakage while the impactor is sliding into CFRP [cone-cylinder-cone] bullet guide pocket (Figure 4-12-a). The fiber breakages are obvious in the first, second, third and fourth steps, where there is less content of CFRP. In the second stage, the slipping force increases gradually with some small peaks due to the local breakage of fibers till it reached 26.2 kN at 21.1 mm stroke. At this stroke, the impactor was observed to be in full contact with the face and move together as one, and the test can be considered as a crushing between solid platens. Transverse shear cracks were observed to propagate around the circumference as shown in Figure 4-12-b. Formation of these cracks lead to a significant drop of 10 kN in slipping force carrying capacity. Then after, a load recovery is noticed and the slipping force reaches 35.6 kN at 35.9 mm displacement. As the impactor progresses, more cracks were imitated and propagated in the hoop direction of the third stage. This results in another drop of 8 kN as

shown in Figure 4-12-c. In the fourth stage, another load recovery is observed and the slipping force reaches the highest value of 40 kN. All the structure is deformed with fiber breakages and contact losses in the fourth conical steps (see Figure 4-12-d).

Figure 4-13 shows the slipping force-stroke curves for SET-2 (i.e. Bullet guiding pocket with conical angles of 45°, 50° and 55°). Almost the same behavior was observed for the angles; four failure stages can be seen from the curves. Numerical results for 50° and 55° of CFRP bullet guiding pocket are presented in Appendix F.


Figure 4-13: Experimental slipping force-stroke curve for SET-2 of the CFRP BGP

4.2.2 Micro failure mechanism of CFRP BGP

Scanning electron microscopy (SEM) images of the five conical angles of the CFRP bullet guiding pockets together with their slipping force-stroke curves are shown in Figure 4-14. These SEM images were taken to analyze the energy dissipation in the structure to get further explanations of the experimental results. In 35° CFRP bullet guiding pocket, the first visual crack occurred at 24.5 mm stroke. While in 40° CFRP bullet guiding pocket, this crack occurred at 27.3 mm stroke. For CFRP bullet guiding pocket with conical angles of 45°, the first SEM images taken for a sample prepared from point A, stage 2 at 21.1 mm stroke and point B at 35.9 mm stroke. On the other hand, for CFRP bullet guiding pocket with conical angles of 50°, the first SEM images taken for a sample prepared from point A, stage 2 at 21.3 mm stroke and point B at 36.5 mm stroke. First visual crack occurred at 21.3 mm stroke (point A), and the second SEM image (point B) at 36.5 mm stroke. In 55° CFRP conical tube, point A represents a crack on 15.5 mm stroke and point B on 46.6 mm stroke. In all cases, it can be noticed that the ABS plastic has cracked and started to separate from the CFRP layers after the fibers started to break. Most of the ABS plastic cone faced a peel-off failure due to its low porosity for the epoxy, as the surface finishing of the ABS plastic is very fine, thus low adhesive bonding were created between the ABS plastic and CFRP layer. On the other hand, some micro-pieces are still stuck with the CFRP as shown in the SEM images. For all samples, matrix cracking and fiber breakage are the main failures in the structure, due to the normal stresses experienced by the CFRP composites. On the other hand, as the impactor slides, a delamination is observed between the CFRP layers.
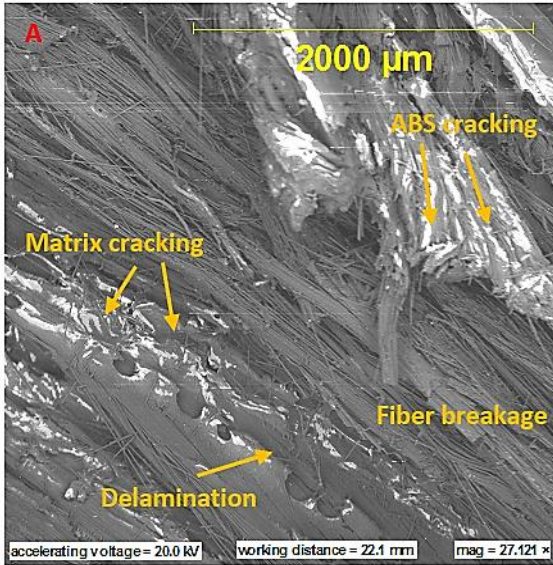
(a1) SEM for 35° CFRP BGP
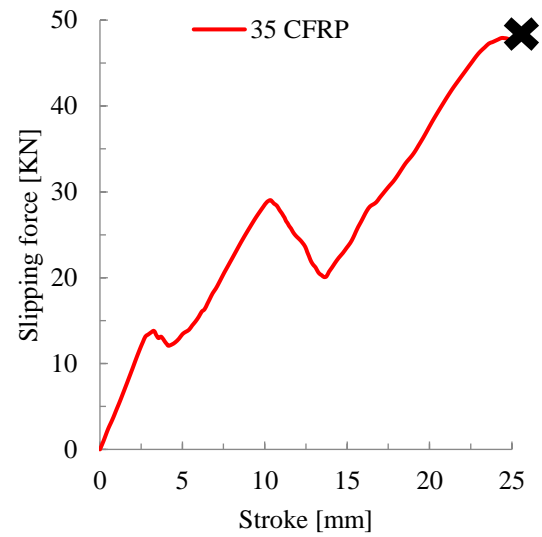
(a2) Slipping force-stroke curve for 35° CFRP BGP up to 24.5 mm stroke
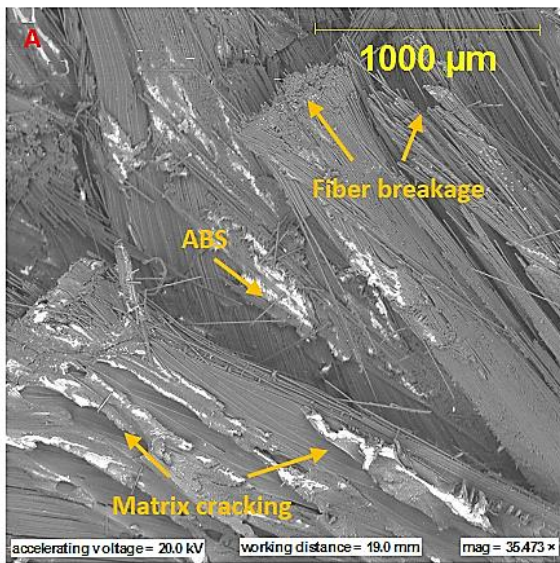
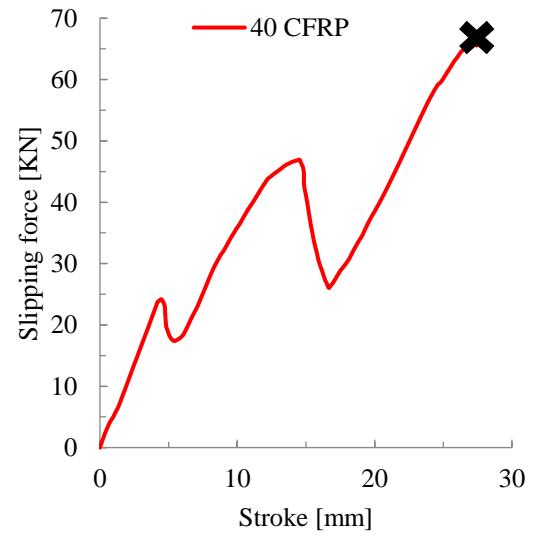(b1) SEM for 40° CFRP BGP

(b2) Slipping force-stroke curve for 40° CFRP BGP up to 27.3 mm stroke

(c1) SEM for 45° CFRP BGP at point A
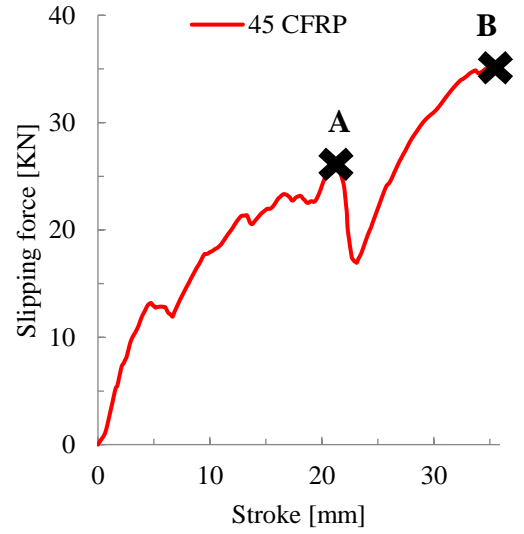
(c2) Slipping force-stroke curve for 45° CFRP BGP up to 35.9 mm stroke

(c3) SEM for 45° CFRP BGP at point B

(d1) SEM for 50° CFRP BGP at point A

(d2) Slipping force-stroke curve for 50° CFRP BGP up to 36.5 mm stroke

(d3) SEM for 50° CFRP BGP at point B
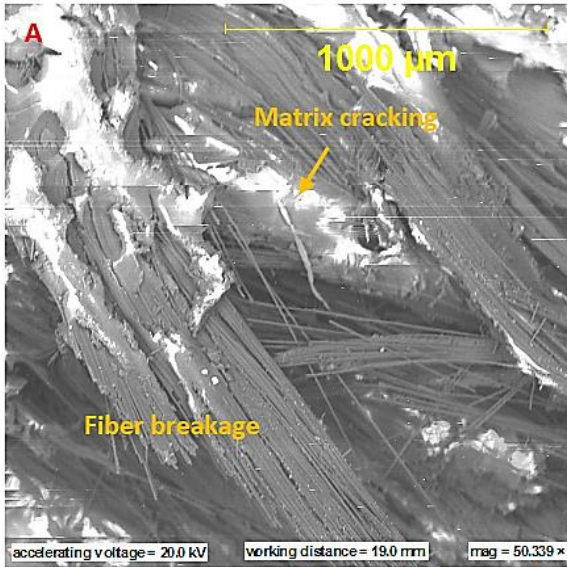
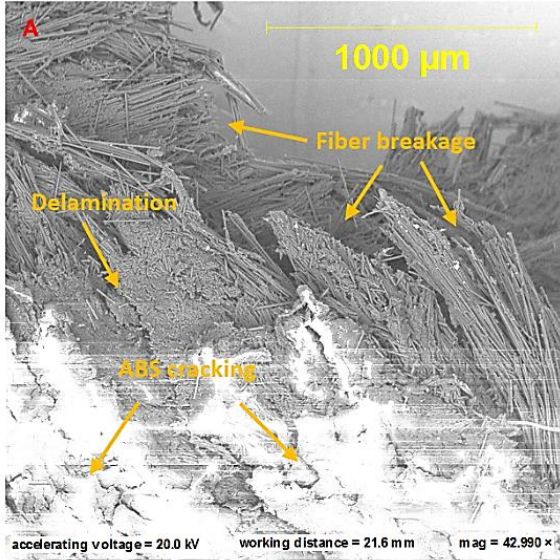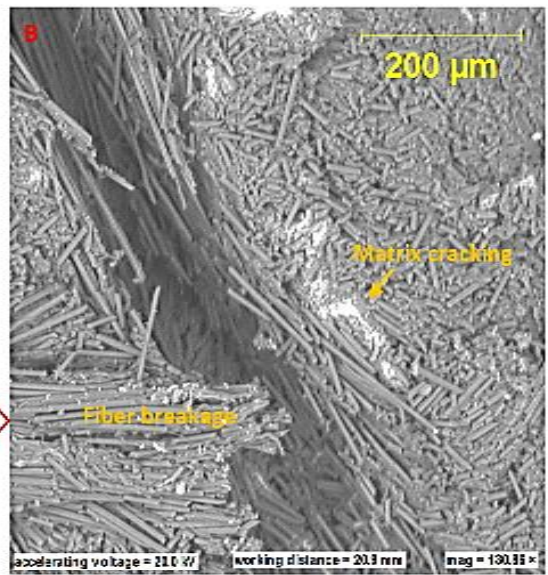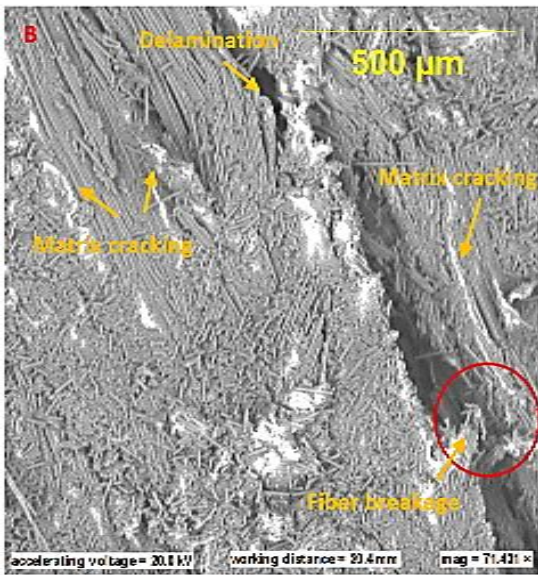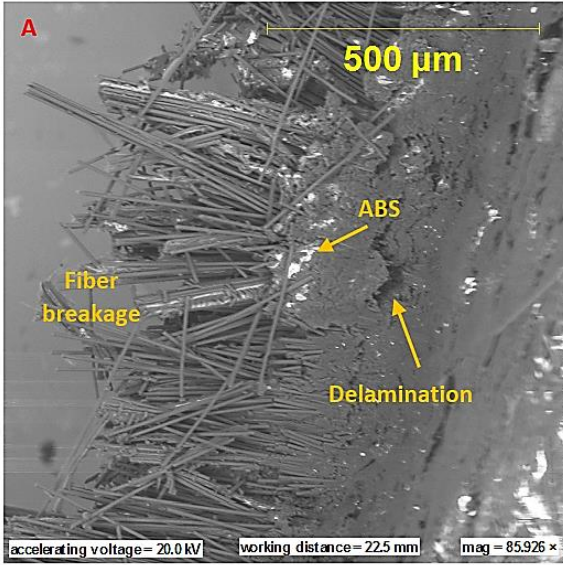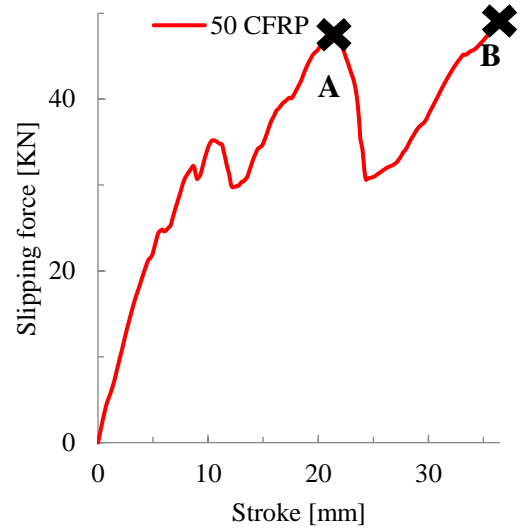(e1) SEM for 55° CFRP BGP at point A
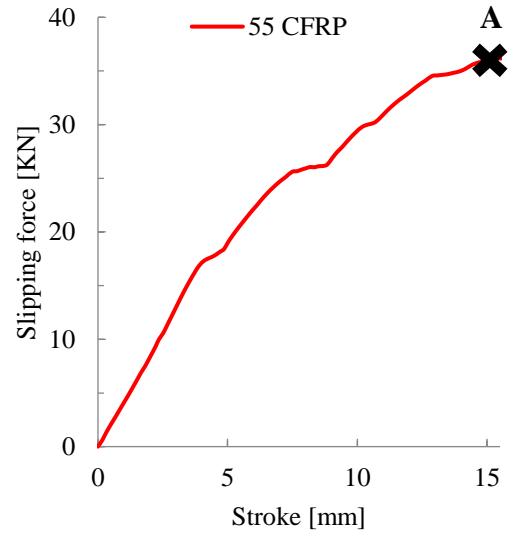
(e2) Slipping force-stroke curve for 55° CFRP BGP up to 15.5 mm stroke
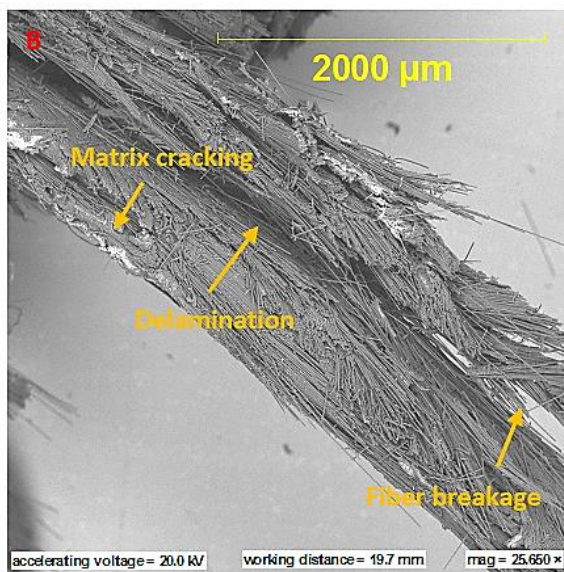
(e3) SEM for 55° CFRP BGP at point B

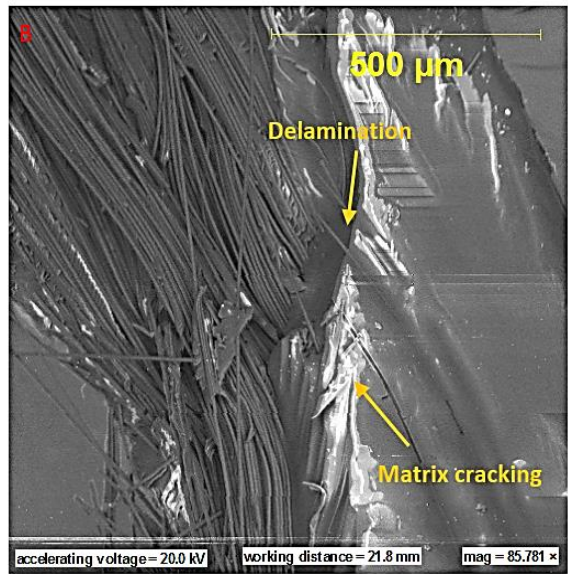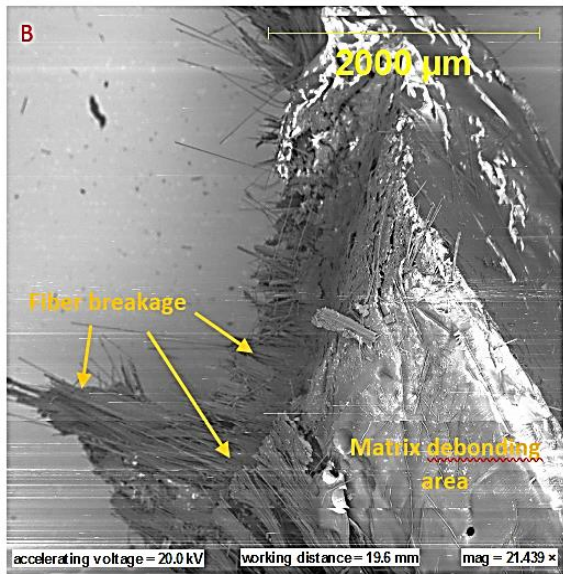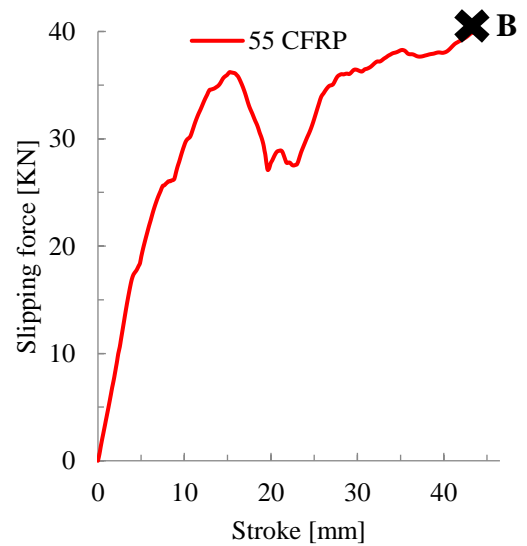(e4) Slipping force-stroke curve for 55° CFRP BGP up to 46.6 mm stroke

Figure 4-14: SEM for the five conical angles of the CFRP BGP at different many points

4.2.3   Crashworthiness parameters for CFRP BGP

Crashworthiness parameters were determined based on the quasi-static behavior from the experimental results for the CFRP bullet guiding pocket. Initial critical load ($P_{i,cri}$), mean load (P_m) and maximum load (P_{max}) were obtained directly from slipping force-stroke curves for the five conical angles, while the crashworthiness parameters such as crush force efficiency (CFE), energy absorbed (EA) and specific energy absorbed (SEA) were calculated using Equations (2.1), (2.2) and (2.3) and listed in Table 4-4. From these results, the CFRP bullet guiding pocket with conical angles of 50° exhibited to have the highest energy absorption capability. Therefore, the Bullet Guiding Pocket Armor Plate (BGPAP) will be designed with conical angle of 50°.

Table 4-4: Crashworthiness parameters for the 5 conical angles of CFRP BGP

Conical angle	$P_{i,cri}$ [kN]	P_m [kN]	P_{max} [kN]	CFE [kN/kN]	EA [kJ]	SEA [kJ/kg]
35°	13.7	49.88	93.26	0.53	2.92	9.33
40°	23.99	50.08	77.33	0.65	3.17	10.78
45°	13.18	26.89	40.16	0.67	1.65	7.21
50°	32.25	37.17	56.69	0.66	2.39	11.12
55°	36.20	31.40	42.62	0.74	1.98	9.95

4.2.4   Failure modes of CFRP BGP

To investigate the failure modes of the CFRP conical tubes, slipping force-stroke curves were analyzed for the bullet guiding pocket, SEM images were taken for the crack of the structure and crashworthiness parameters were calculated. Two distinct failure-crushing

modes were observed. These failure-crushing modes can be identified and classified as follows:

1. Catastrophic failure mode: this failure mode is observed to dominate the energy absorption mechanism of bullet guiding pockets set 1 (35° and 40°). This failure mode is characterized by sudden significant drops after each peak which is more than 50% of previous peak, this makes the energy absorption mechanism unstable.

2. Progressive failure mode: Progressive failure mode starts from the top step of bullet guiding pocket and dominates the sliding crush process of five steps bullet guiding pocket with conical angles of 45°, 50° and 55°. This mode is accompanied with crush mechanism that involves local matrix deformation and fiber micro breakage in small areas that moves progressively. The slipping force-stroke curves for this type of mode is observed to have a very stable energy absorption mechanisms. Furthermore, it is also evident from Table 4-4 that this type of progressive failure mode exhibited highest specific energy absorption.

4.2.5 Crushing response of KFRP BGP

The crushing behavior for the KFRP bullet guiding pocket was divided into two sets based on the appearance of their slipping force-stroke curves and mode of failure. SET-1 associated to the bullet guiding pocket with conical angles of 35°, 40° and 45°, while SET-2 associated to the bullet guiding pocket with conical angles of 50° and 55°. In parallel, simulation of the same has been carried out based on the parametric study that was performed in Sections (3.2.4, 3.2.5 and 3.2.6).

4.2.5.1   SET-1 (conical angle = 35°, 40° and 45°)

Figure 4-15 and Figure 4-16 show the slipping force-stroke curves and a representative

deformation history obtained experimentally and numerically from crushing the 35° KFRP

bullet guiding pocket, respectively. The first contact line between the tube and the impactor

is at 9.86 mm radius of the impactor. Based on the impactor ellipse equation, the impactor

head is 16.95 mm inside the geometry as shown in Figure E.1 (Appendix E). The sliding

penetration test starts from this point. Five stages were observed during the test which are

discussed as follows:
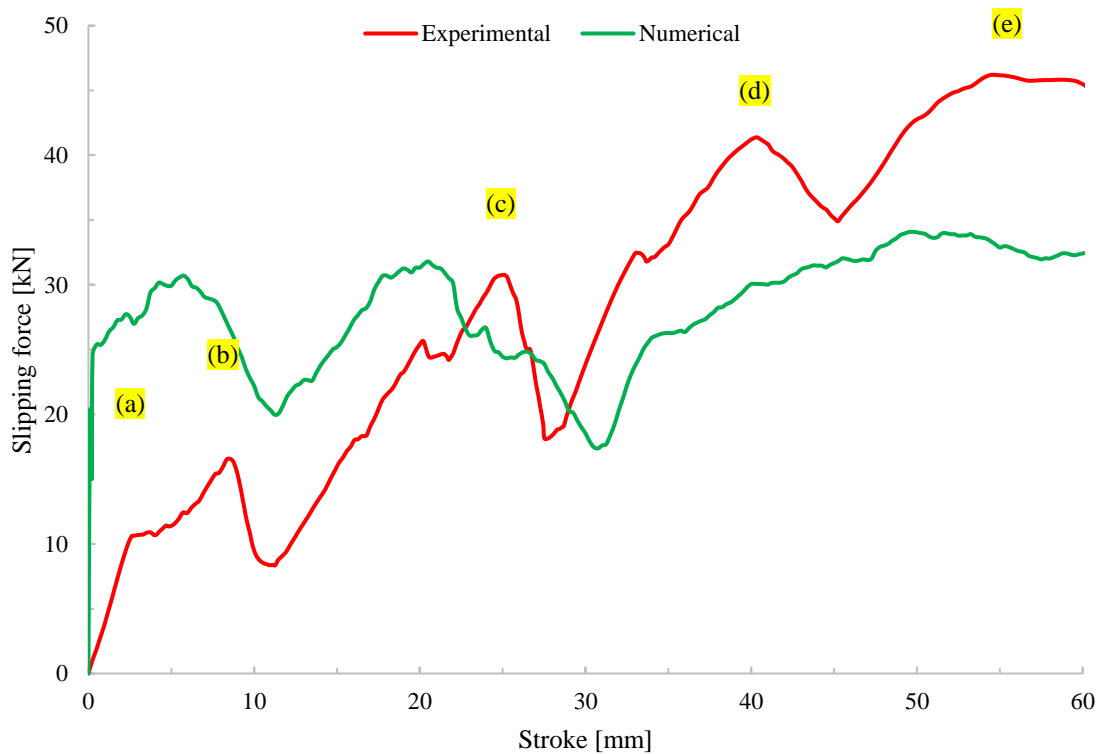
Figure 4-15: Experimental and numerical slipping force-stroke curves for 35° KFRP BGP
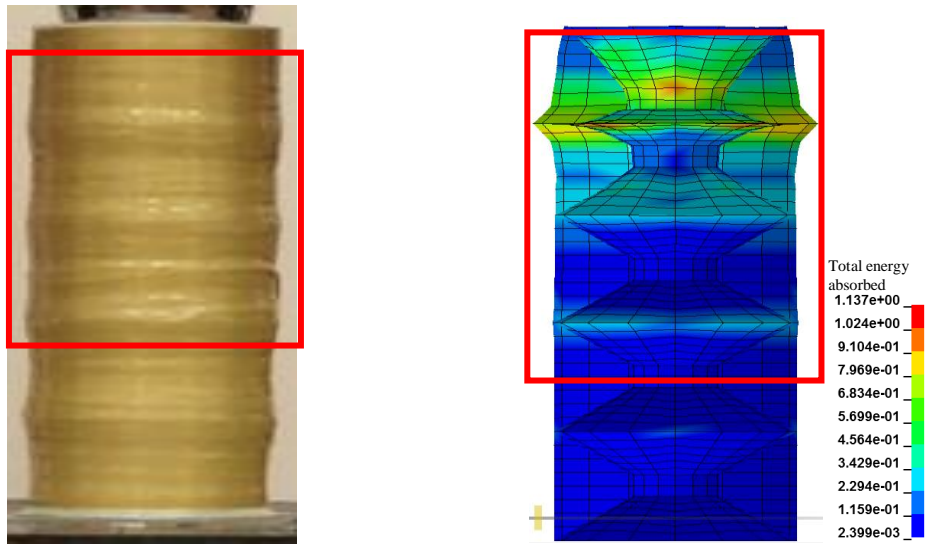
(a) 2.9 mm stroke, Linear behaviour of crushing slipping force-stroke curve
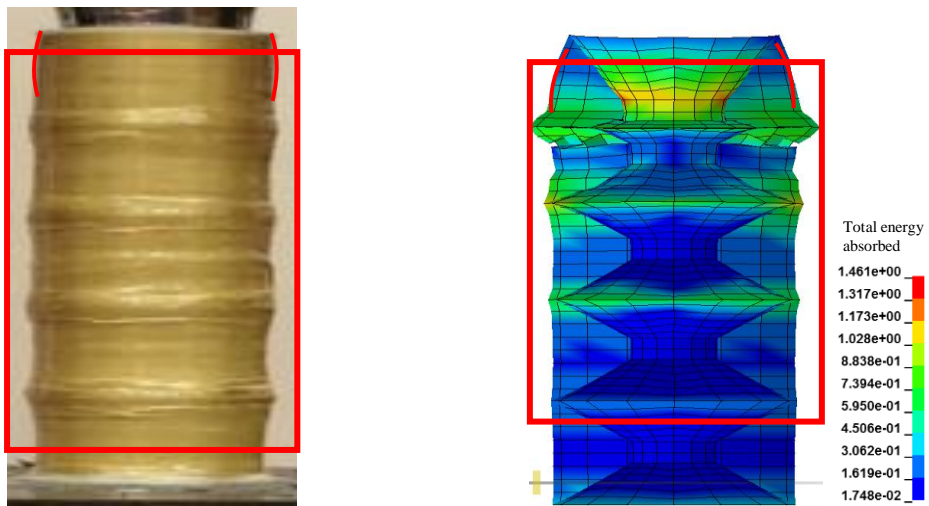
(b) 8.5 mm stroke, Fiber sheaing in all edges of the structure
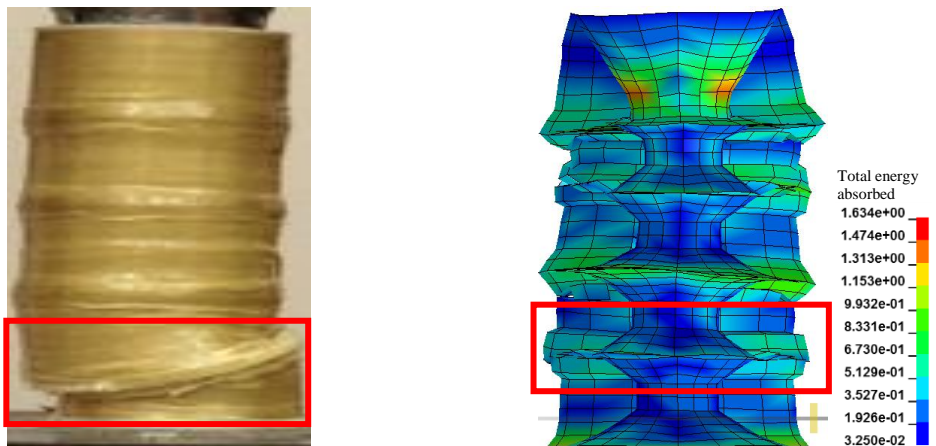
(c) 24.9 mm stroke, Tearing in the last step of the structure
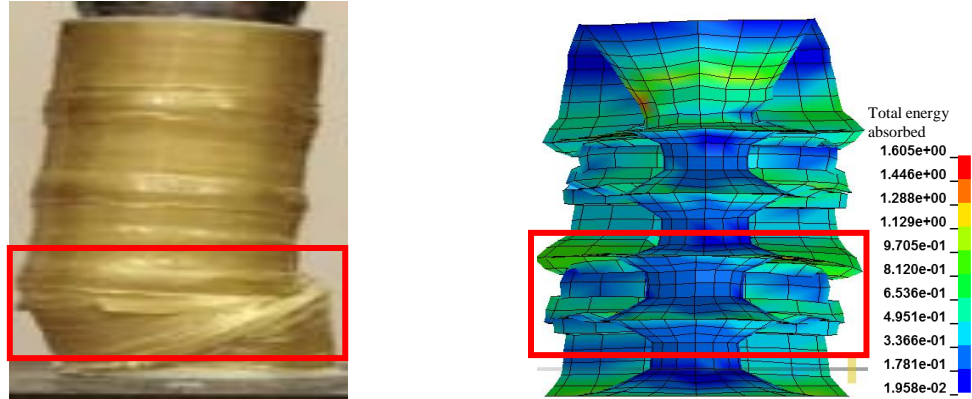
(d) 40.5 mm stroke, Slipping in the last step with fiber shearing in steps 1 and 2
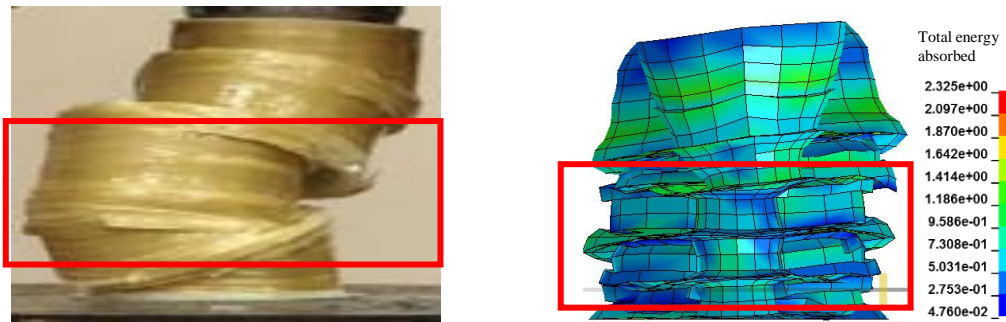
(e) 54.2 mm stroke, The whole structure has failed and tearing between fibers occured
Figure 4-16: Representative photos during the different five stages of deformation history for the 35° KFRP BGP; experimentally and numerically.

In the first stage, it can be noticed that the slipping force-stroke curve behaves linearly till it reaches the first peak load at 10.7 kN and 2.9 mm stroke (Figure 4-16-a). At this stage the bullet guiding pocket's inside wall experienced compression, while its outside wall experienced tension. After that, the sliding force increases gradually till it reaches 16.6 kN at 8.5 mm stroke, where the impactor has stuck in the cylindrical part of the first step of bullet guiding pocket and slide as one part. At this stroke, the test can be considered as an axial crushing between two platens. It is worth to mention that formation of cracks was observed to be initiated at the joints between the steps as shown in Figure 4-16-b. At this crush zone, transverse shear cracking mechanism is found to be dominating the energy absorption capability. This mechanism is accompanied by a sudden significant drop in

crushing force carrying capacity and found to be 8.4 kN. The force carrying capacity at the attained level for around 2 mm stroke. Then after, the crushing force increases gradually to reach 30.7 kN at 24.9 mm stroke. This recovery, followed by another considerable sudden drop in load was observed due to the cracks formed at the joints between the cone-cylinder-cone in the last step of the bullet guiding pocket. As the generated out of plane bending moment increases, tearing stress increases to promote delamination's between the KFRP layers (Figure 4-16-c). Another recovery in slipping crush capacity observed and found to reach 41.2 kN at 40.5 mm stroke. Then after, as the slipping crush progresses, transverse shear cracks initiates at the joints between the cone-cylinder-cone the last step of bullet guiding pocket. This results in moderate drop in the slipping crush force capacity was observed to be 35 KN and sustained for 5 mm as shown Figure 4-16-d. The end of cracks formation accompanied by a gradual increase in bullet guiding pocket's slipping force and found to reach 46 kN at 54 mm stroke. For the rest of the stroke, bullet guiding pocket's slipping force sustain around 46, in which matrix cracking and fiber breakage found to be dominated the energy absorption mechanism during this stage as shown Figure 4-16-e.

Figure 4-17 shows the slipping force-stroke curve for SET-1 (i.e. bullet guiding pocket of 35°, 40° and 45° conical angle). The ANSYS/LS-DYNA predicted the slipping force-stroke curve for the KFRP bullet guiding pocket with conical angle of 35° is correlated with the experimental results as shown in Figure 4-15. In general, the simulation predicts very well the complete slipping crush force behavior. The plots indicate wethe matching of energy dissipation with the experimental deformation history. In general, the experimental instantaneous slipping crush force is lower than that of the simulated

response. Numerical results of 40° and 45° KFRP bullet guiding pockets are presented in Appendix F.
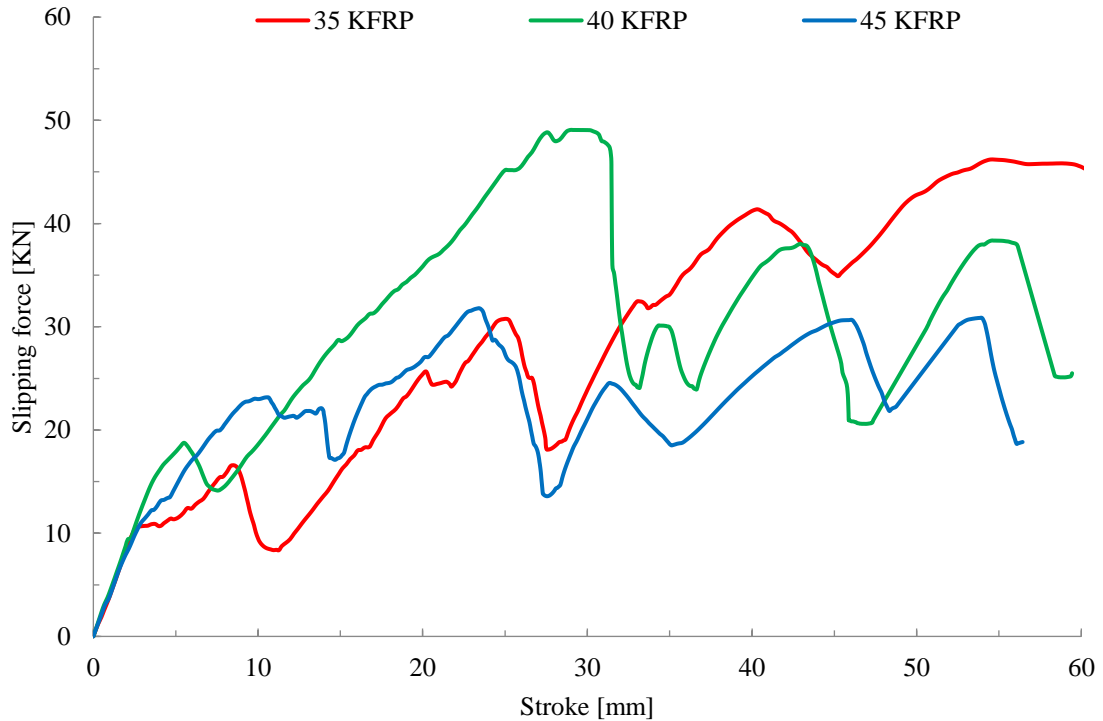
Figure 4-17: Experimental Slipping force-stroke curve for SET-1 of the KFRP BGP

4.2.5.2   Set 2 (conical angle = 50° and 55°)

Figure 4-18 and Figure 4-19 show the slipping force-stroke curves and a representative deformation history obtained experimentally from crushing the 55° KFRP bullet guiding pockets, respectively. The first contact line between the tube and the impactor is at 16.93 mm radius of the impactor which is the reference point in this conical angle. Based on the impactor ellipse equation, the impactor head is about 32.84 mm inside the geometry as shown in Figure E.5 (Appendix E). The sliding crush test starts from this point. Four stages were observed during the test which are discussed as follows:
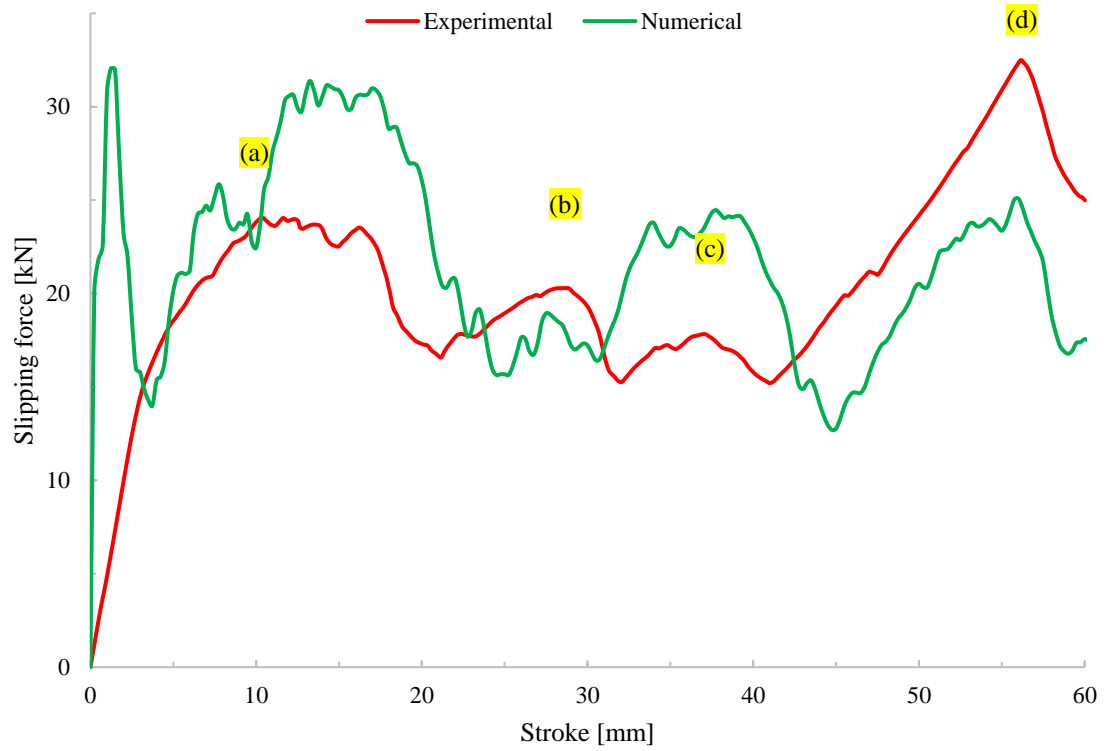
Figure 4-18: Experimental and numerical slipping force-stroke curves for 55° KFRP BGP
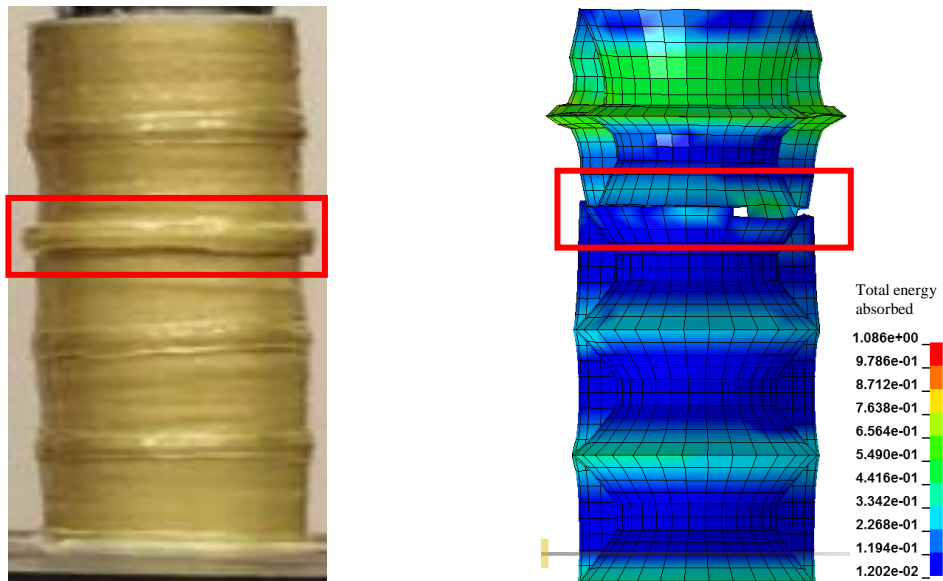
(a) 10.6 mm stroke, Fiber pull-out in the conical steps with fiber cracks in the second step
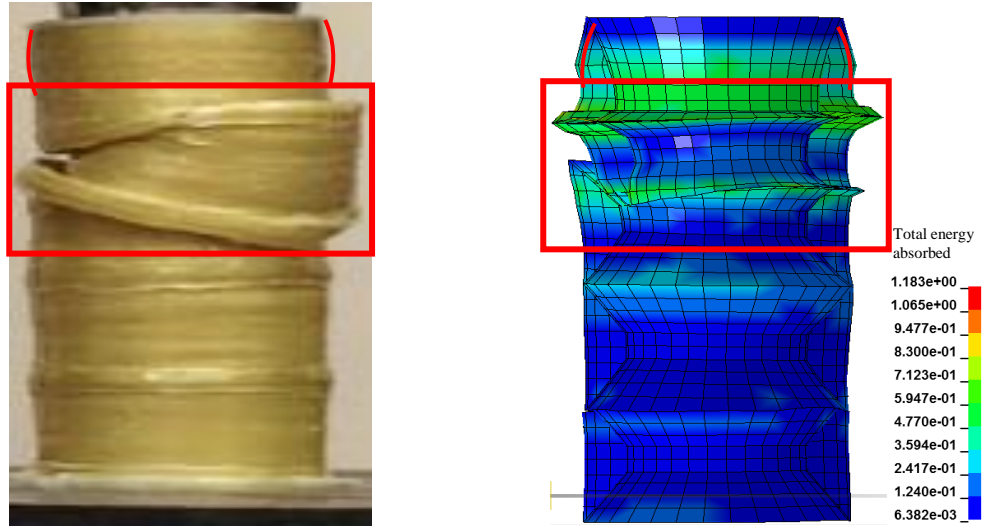
(b) 16.5 mm stroke, Failure at steps 1 and 2 with slipping and contact loss
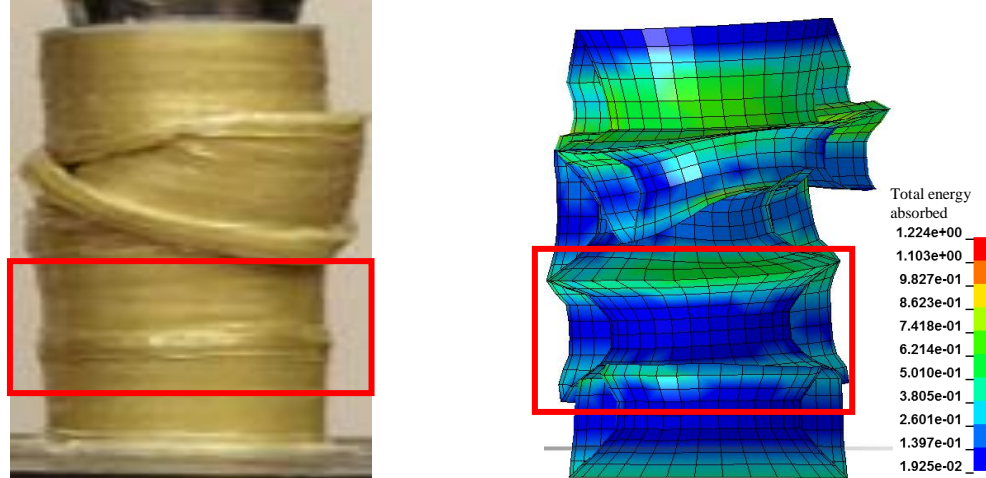
(c) 28.4 mm stroke, Matrix cracking and fiber shearing in the edges of the conical steps
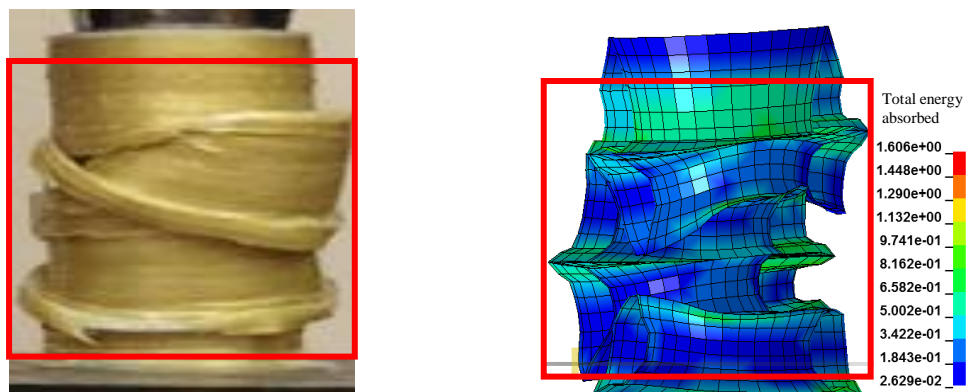
(d) 56.3 mm stroke, The whole structure has failed and tearing occured

Figure 4-19: Representative photos during the different four stages of deformation history for the 55° KFRP BGP; experimentally and numerically.

In the first stage, the slipping force-stroke curve is taking a polynomial curve shape till it reaches the first peak at 23.9 kN and 10.6 mm stroke (Figure 4-19-a). At this stage the penetrating impactor is compressing the structure by sliding itself inside the structure, at this point the impactor has stuck in the cylindrical geometry, thus they became as one part. This first crack is observed at the second conical step, fibers started to pull-out to end up with fiber breakage, while the other steps are facing fiber expansion before getting the cracks and breaks. In the second stage, the structure is under many peaks from the first stage, as many cracks are noticed in the same first and second conical steps, no increase in load through the last 6 mm stroke. Slipping was obvious in the first and second step which caused a sudden big drop in load to reach 16.8 kN within 4 mm stroke (Figure 4-19-b). The transverse shearing forces is the main forces that is responsible for this failure in fibers. In the third stage, the load has increases gradually till it reaches 20.3 kN at 28.4 mm stroke. More matrix cracks and fiber breakage are presented in the third and fourth conical steps. These failure results in a 5 kN drop in slipping crush capacity as shown in Figure 4-19-c. In the fourth stage, the slipping crush force recovered and increases gradually to reach its maximum peak value of 32.33 kN at 56.3 mm stroke. Like other angles in set-1, transverse shear cracking found to dominate the overall slipping crush force of bullet guiding pocket set-2 as shown in Figure 4-19-d.

The slipping crush force–stroke curves for Set-2 is shown in Figure 4-20. At pre-crush and post crush stage, the stability of energy dissipation mechanisms is evident, since the instantaneous slipping crush force capacity is very much close to the average slipping crush force. Four dissipation energy mechanism stages can be seen from the curves. Numerical results for the 50° KFRP bullet guiding pocket are presented in Appendix F.
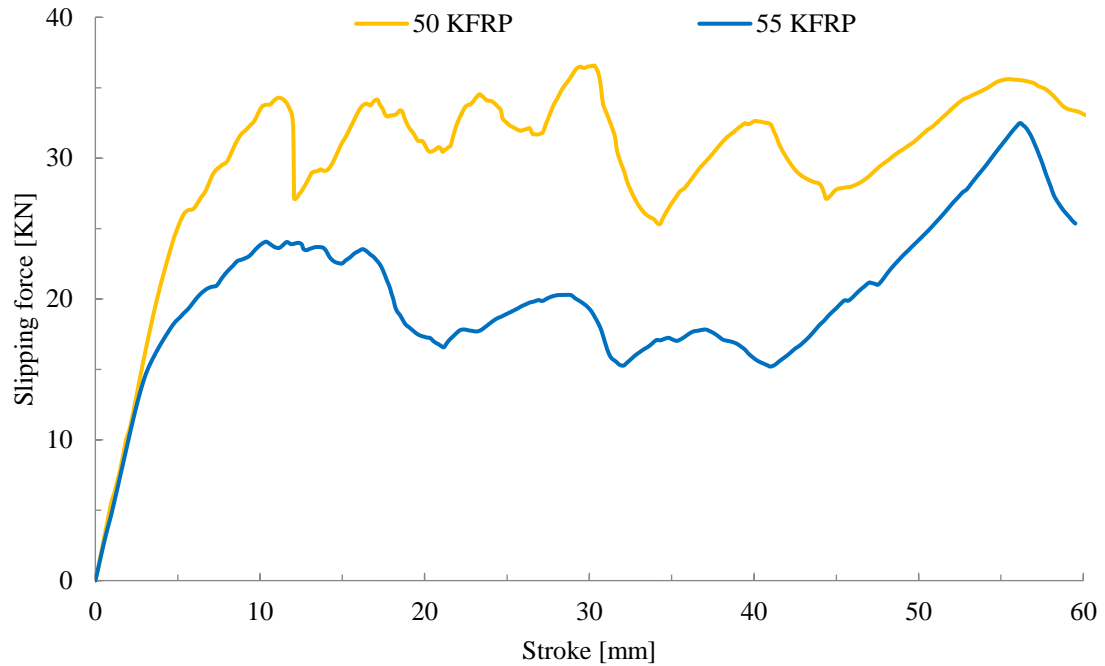
Figure 4-20: Experimental slipping force-stroke curve for SET-2 of the KFRP BGP

4.2.6 Micro failure mechanism of KFRP BGP

Figure 4-21 shows scanning electron microscopy (SEM) images for the five conical angles of the KFRP bullet guiding pockets. The SEM was performed for sample taken from crush zones at different stages. These SEM analyses were performed to allow us understand, quantify and analyze the energy dissipation mechanisms. For 35° KFRP bullet guiding pocket, SEM image of sample is taken at point A (i.e. 24.9 mm stroke). While for 40° KFRP bullet guiding pocket, the SEM image was taken at 27.34 mm stroke (point A). For 45° KFRP bullet guiding pocket, points A and B found to be at strokes 10.66 mm and 31.31 mm. On the other hand, for 50° and 55° KFRP bullet guiding pocket, the SEM images were taken for samples at points A and B at stroke 11.3 mm and 16.5 mm, respectively. While, for 50 and 55° KFRP bullet guiding pocket, points 30.5 mm and 56.3 mm stroke. SEM images indicate that matrix cracking, fiber pull-out at outer most layer due to the tearing

stress due to the internal pressure by the sliding impactor. The intensive fiber pullout and fiber breakage lead to transverse shear cracking. As the impactor sliding progresses, delamination between the KFRP layers occurs.
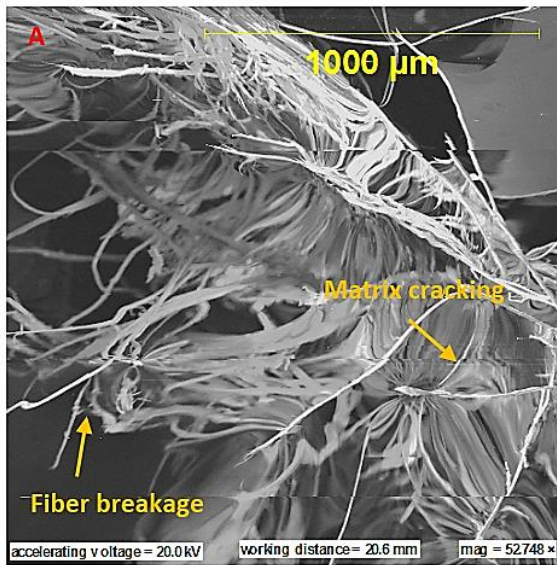
(a1) SEM for 35° KFRP BGP
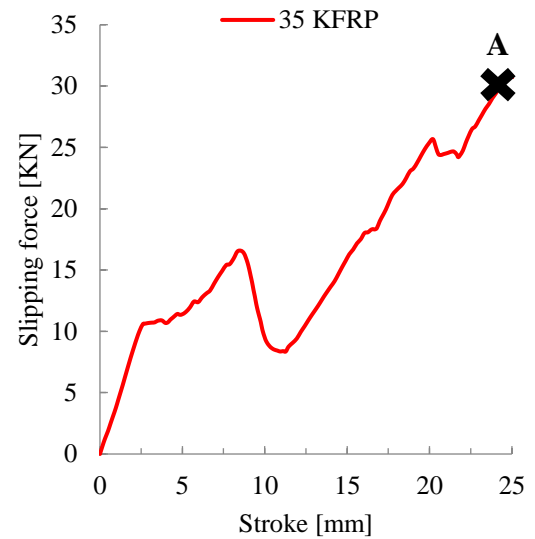
(a2) Slipping force-stroke curve for 35° KFRP BGP up to 24.9 mm stroke
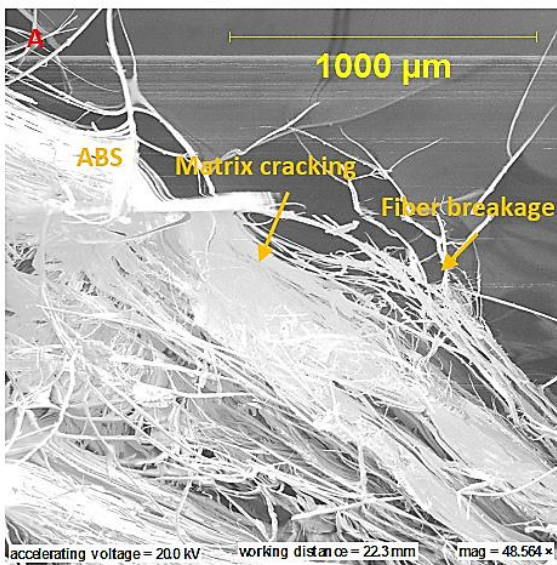
(b1) SEM for 40° KFRP BGP
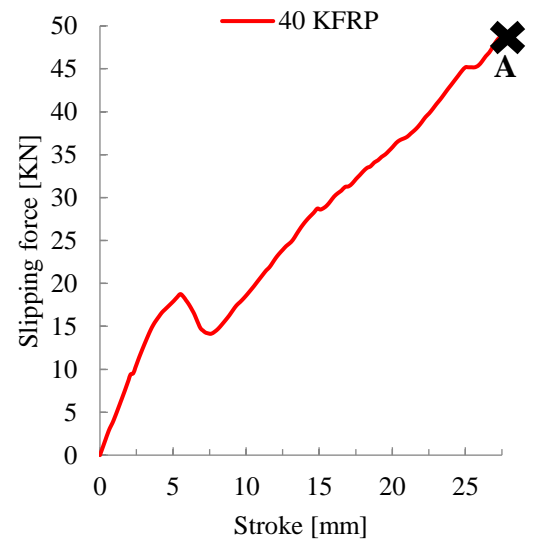
(b2) Slipping force-stroke curve for 40° KFRP BGP up to 27.34 mm stroke
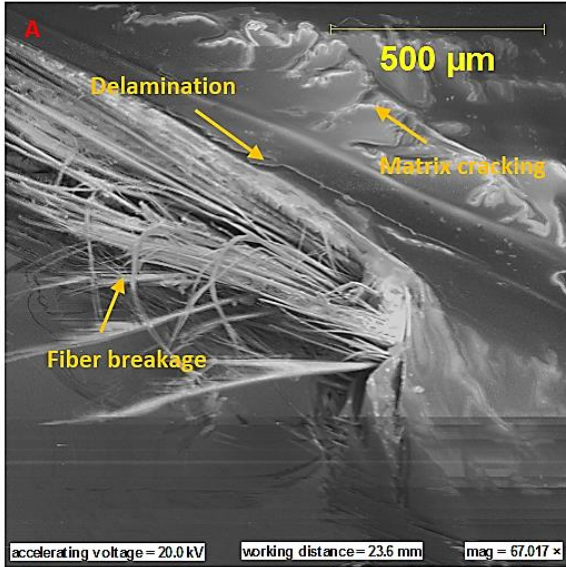
(c1) SEM for 45° KFRP BGP at point A
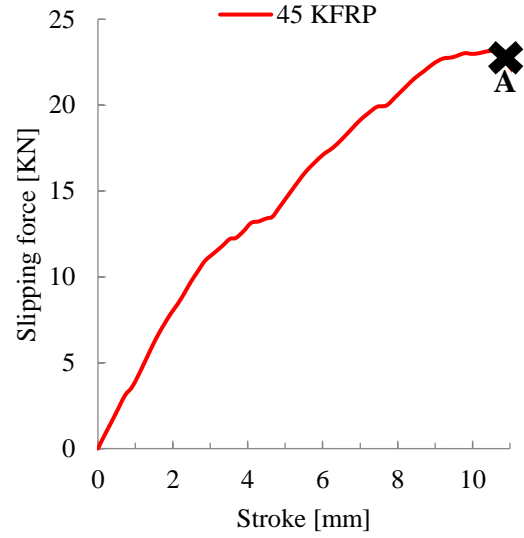
(c2) Slipping force-stroke curve for 45° KFRP BGP up to 10.66 mm stroke
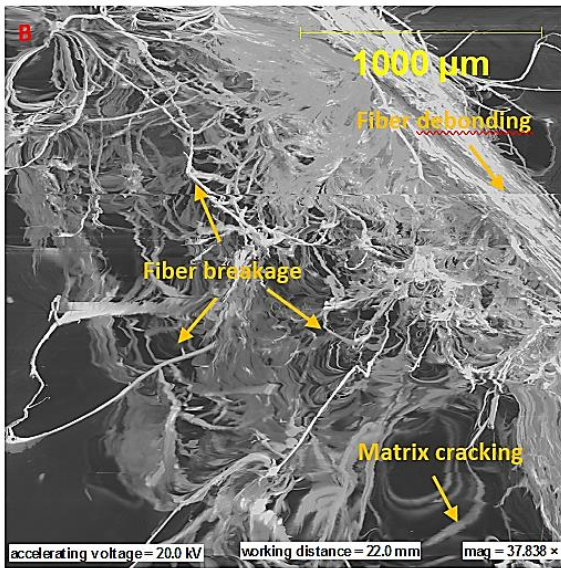
(c3) SEM for 45° KFRP BGP at point B
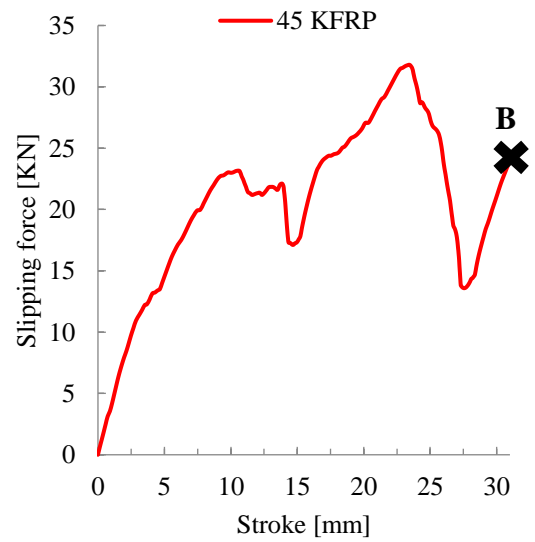
(c4) Slipping force-stroke curve for 45° KFRP BGP up to 31.31 mm stroke
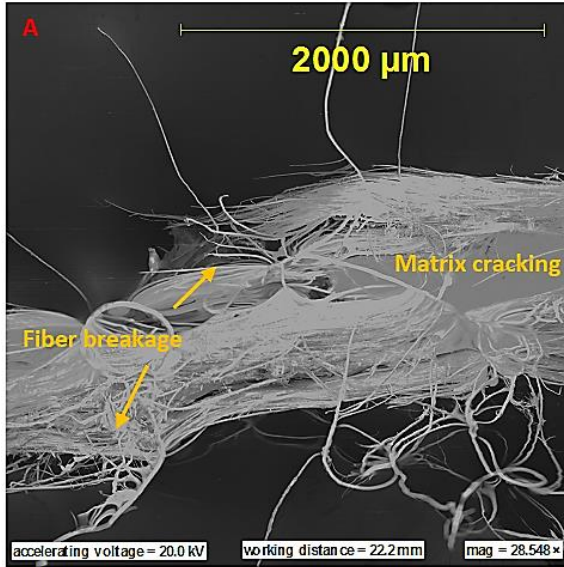
(d1) SEM for 50° KFRP BGP at point A
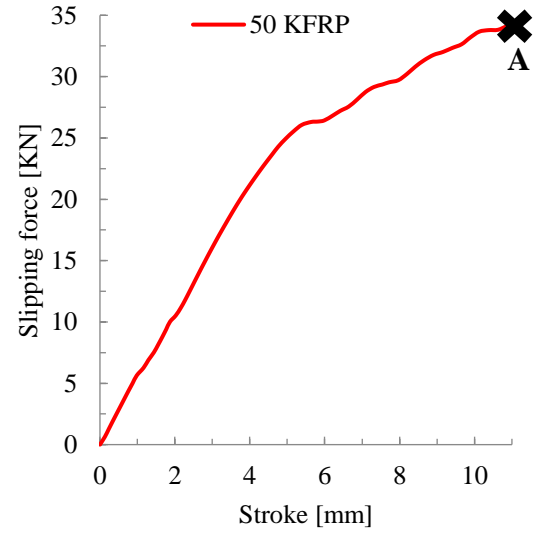
(d2) Slipping force-stroke curve for 50° KFRP BGP up to 11.3 mm stroke
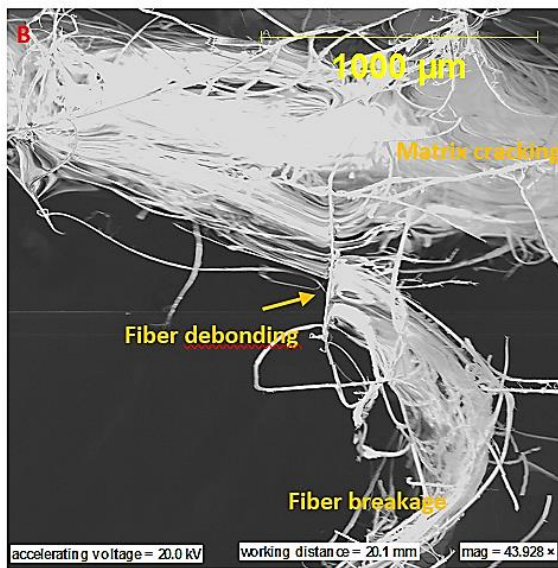
(d3) SEM for 50° KFRP BGP at point B
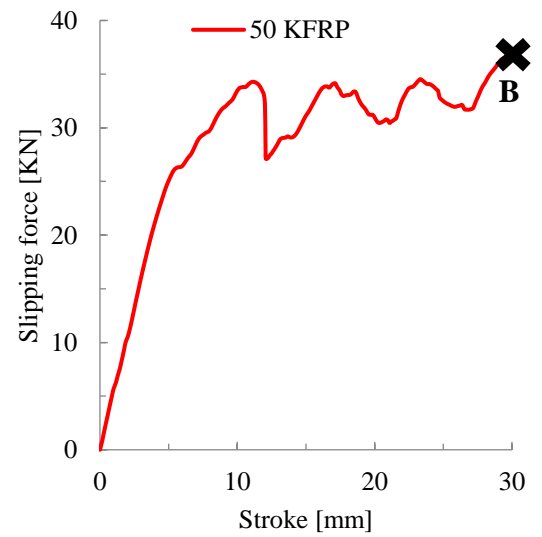
(d4) Slipping force-stroke curve for 50° KFRP BGP up to 30.5 mm stroke
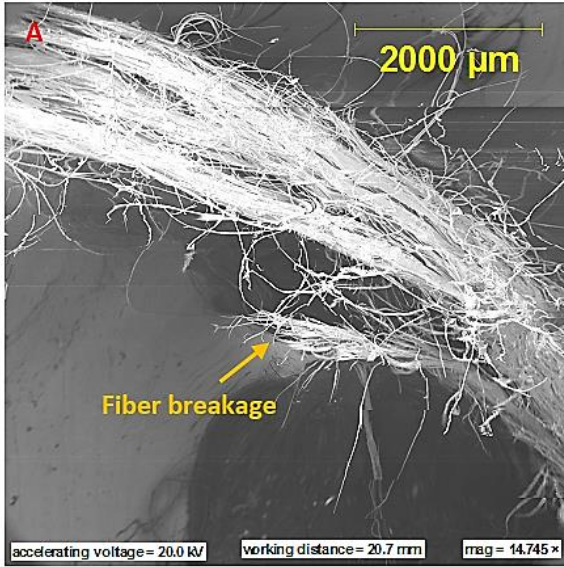
(e1) SEM for 55° KFRP BGP at point A
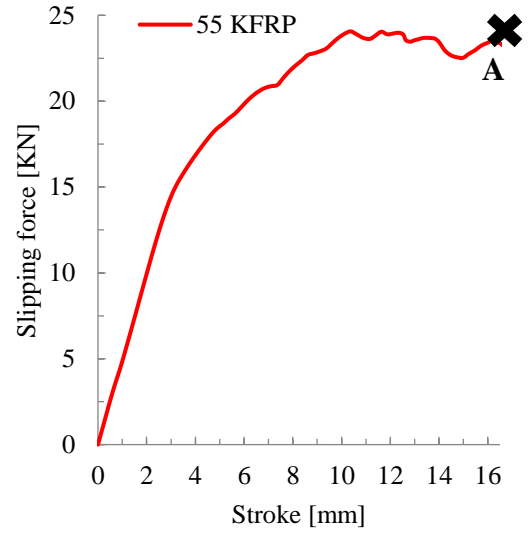
(e2) Slipping force-stroke curve for 55° KFRP BGP up to 16.5 mm stroke
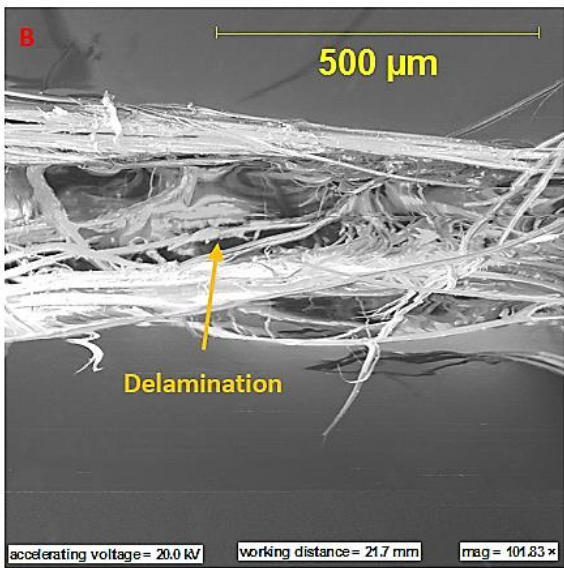
(e3) SEM for 55° KFRP BGP at point B
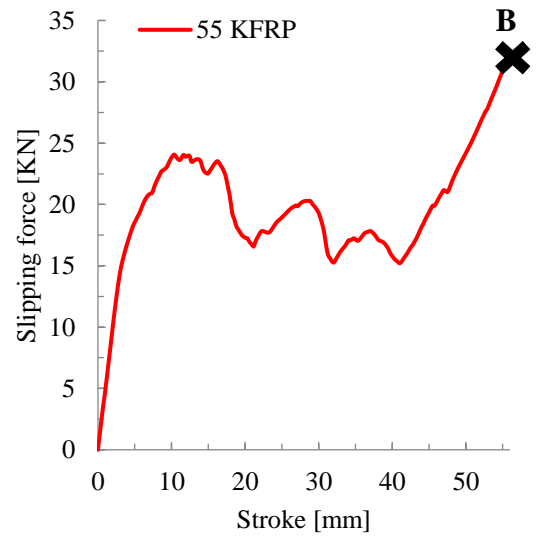
(e4) Slipping force-stroke curve for 55° KFRP BGP up to 56.3 mm stroke

Figure 4-21: SEM for the five conical angles of KFRP BGP

4.2.7 Crashworthiness parameters for KFRP BGP

Initial critical load ($P_{i,cri}$), mean load (P_m) and maximum load (P_{max}) were obtained directly from load-stroke curves for the five conical angles, while the crashworthiness parameters; crush force efficiency (CFE), energy absorbed (EA) and specific energy absorbed (SEA) were calculated using Equations (2.1), (2.2) and (2.3) and listed in Table 4-5. Therefore, 50° conical angle had the highest specific energy absorption value, which makes it a good canditate as inserts in the Bullet Guiding Pocket Based Armor Plate (BGPAP).

Table 4-5: Crashworthiness parameters for the five conical angles of KFRP BGP

Conical angle	$P_{i,cri}$ [kN]	P_m [kN]	P_{max} [kN]	CFE [kN/kN]	EA [kJ]	SEA [kJ/kg]
35°	10.67	27.46	46.20	0.59	1.74	6.99
40°	18.76	30.49	51.50	0.59	1.87	7.76
45°	23.16	21.62	31.78	0.68	1.27	6.29
50°	34.28	29.30	36.57	0.80	1.82	9.10
55°	23.93	19.82	32.49	0.61	1.22	7.39

4.2.8 Failure modes of KFRP BGP

To investigate the failure modes of the KFRP bullet guiding pockets, slipping force-stroke curves were analyzed for the five-conical angles, SEM images were taken from the crush zone of the structure and crashworthiness parameters were calculated. It can be noticed that the five conical angles were divided into two sets based on to their failure modes. SET-1 which represents 35°, 40° and 45° KFRP bullet guiding pocket, while SET-2 represents 50° and 55° KFRP bullet guiding pockets. In SET-1 a catastrophic failure mode was

observed during the test, as the peak loads faced sudden drops each time, which makes the structure unstable sometimes. In SET-2 a progressive failure mode was observed during the test with a noticeable stability in the structure while it was deformed. Overall, all the samples behaved non-linearly during the test.

4.3   Overall Discussion

Based on the ballistic behavior of the flat and curved body armor plates, it was concluded that non-hybrid [KFRP]$_{40}$ and hybrid [CFRP$_{10}$/KFRP$_{30}$] body armor plates had passed the real shooting test and numerical modelling test with an acceptable back-face signature according to NIJ standard [80]. The deformation for the bullet was higher in case of the hybrid [CFRP$_{10}$/KFRP$_{30}$] armor plate than the non-hybrid [KFRP]$_{40}$ armor plate, and this is referred to the ten layers of carbon fiber that are facing the bullet. Figure 4-22 compares the absorbed energy and specific absorbed energy by each conical angle tube for CFRP and KFRP (weights of the bullet guiding pockets are mentioned in Table 3-3). It can be noticed that CFRP have higher values of absorbed energy than KFRP, although Kevlar has better specific ballistic resistance properties than Carbon fiber. Among the tested specimens, CFRP and KFRP bullet guiding pockets with 50° have been found to display the highest energy absorption capability.

In the FEMs, in SET-1 CFRP conical tubes, it was observed that the crushing response resulted from the numerical simulation is less than obtained from numerical results, and this is because of the element erosion parameters that were defined in the failure criteria of MAT_054, as the failed elements are deleted from the model. This is based on the ultimate
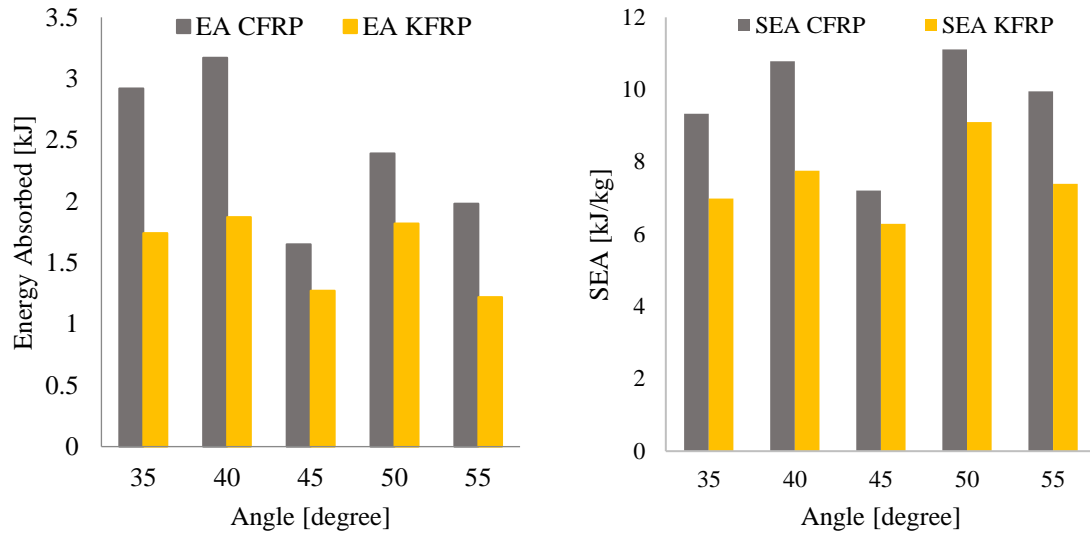
(a) Energy absorbed by CFRP and KFRP   (b) Specific energy absorbed by CFRP and KFRP

Figure 4-22: EA and SEA comparison between CFRP and KFRP.

tensile maximum strains for fiber and matrix under compression. These criteria were defined as DFAILM, DFAILC. This results in minimizing the computational time and very good correlation with results were obtained. In SET-2 CFRP bullet guiding pockets, it was noted that a higher initial peak load obtained from the numerical simulation than the one obtained from the experimental results, and this is because, a value of high friction between the lower plate and the structure that has been used as input for the numerical simulation.

In SET-1 and SET-2 in KFRP, the inner most layers experienced compressive stresses, while outer most layers experienced tearing stresses. The latter found to cause matrix cracking, fiber debonding and fiber pullout, while the earlier, causes matrix crazing and fracturing and fiber breakage. These found to be intensified at the joints between the cone-cylinder-cone of each step.

Finally, it is worth to mention a mechanism that was obvious from the numerical simulation in all bullet guiding pocket sets. An inside curvature or bending towards the impactor is noticed at the beginning of the sliding crushing test, until the impactor became as one part with the first step of the conical cylinder, this bending will be transferred into expansion or remain in the same position depending on the conical angle and the contact points between the impactor and the cylinder. This can be seen clearly from the front section view of the numerical results in Figure 4-9-b, Figure 4-12-b, Figure 4-16-b and Figure 4-19-b.

4.4   Bullet Guiding Pocket Armor Plate (BGPAP)

The main goal of this section is to develop a new body armor based on the findings of the preceding sections, where the material sequence and the conical angle of bullet guiding pocket have been optimized. Accordingly, hybrid [$CFRP_{10}$/$KFRP_{30}$] and the bullet guiding pocket with 50° conical angle were considered as base for the new body armor. It is worth to mention that introducing the bullet guiding pocket in CFRP absorbed more energy than KFRP. It is also important to mention that the validated FEM model has been used to examine the ballistic behavior of the newly developed bullet guiding pocket armor plate (BGPAP).

4.4.1   FEM simulation

A bullet guiding pocket armor plate was developed using the validated FEM model using ANSYS/LS-DYNA software. To this end, bullet guiding pocket of cone-cylinder tube was introduced through the ten layers of CFRP, which flowed by 30 layers of KFRP. The conical tubular part of BGPAP was modelled with a conical angle of 50°. Figure 4-23 shows an isometric view of the BGPAP.
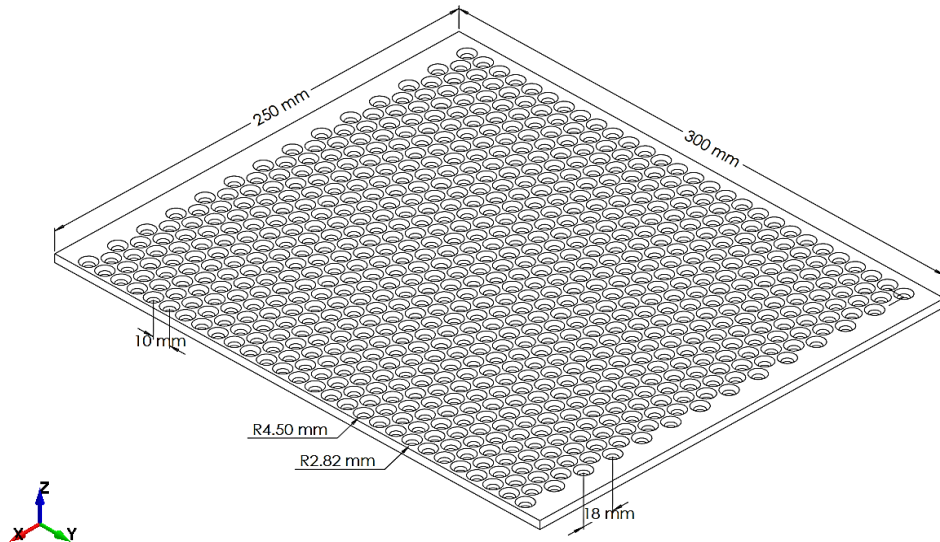
(a) Bullet guiding pocket armor plate geometry with dimensions in mm
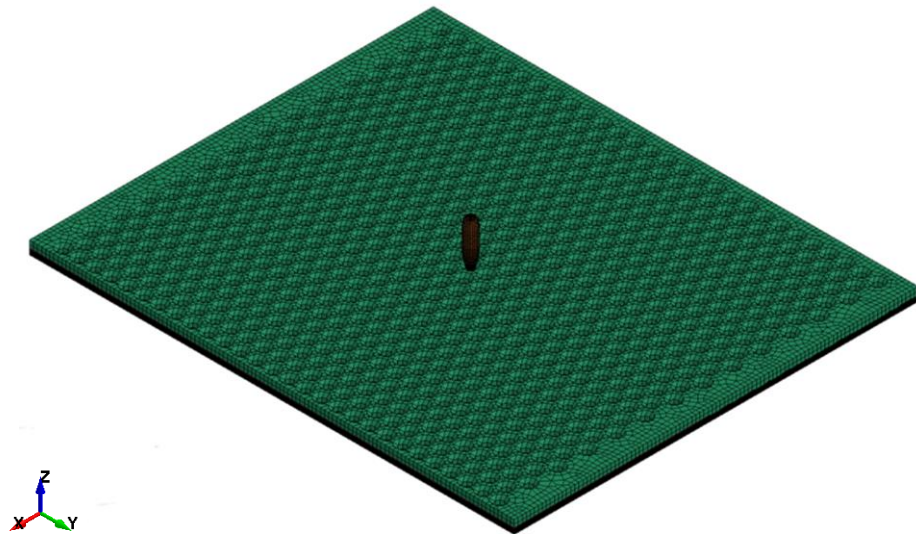
(b) Meshed bullet guiding pocket armor plate

Figure 4-23: Isometric view of the bullet guiding pocket armor plate

Table 4-6 summarizes the number of elements and nodes, section and material types used for each part in the Bullet Guiding Pocket Armor Plate. Figure 4-24 shows a section view of the final FEM. The contact formulation and boundary conditions used in this FEM were mentioned in Section (3.2.3.3). The initial velocity of the bullet was determined to be 398 m/s.
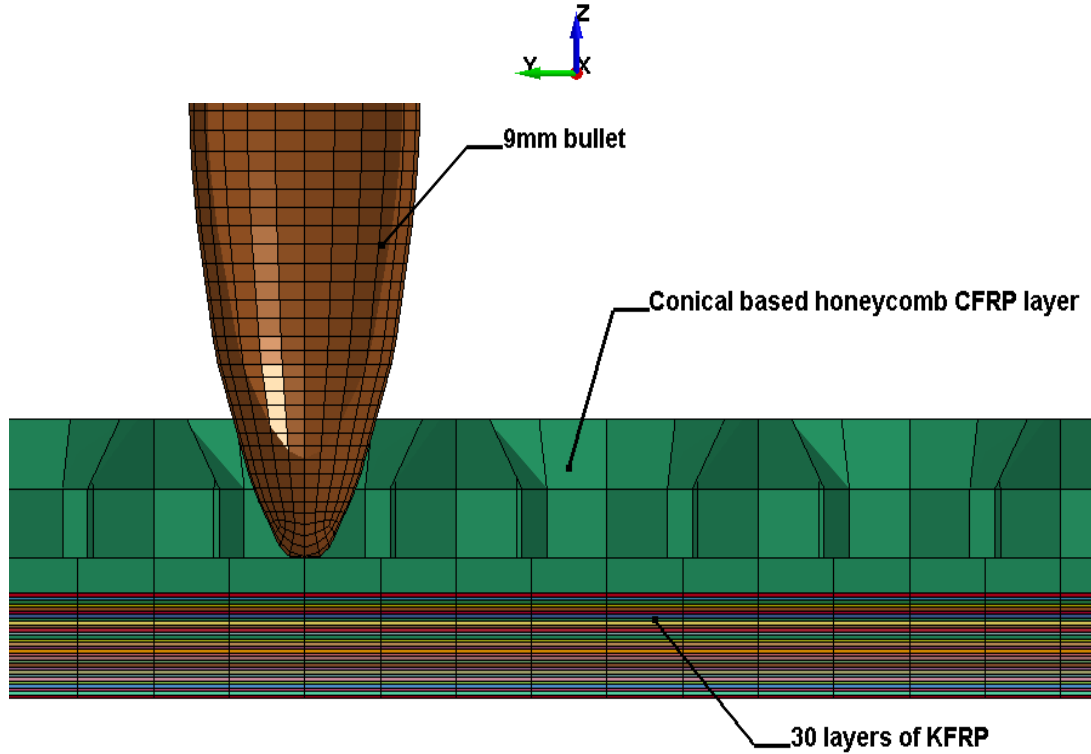
Figure 4-24: Bullet Guiding Pocket Armor Plate FEM

Table 4-6: Summary for number of elements and nodes for the FEM.

Part ID	Part name	No. of elements	No. of nodes	Section	Material
1	CFRP bullet guiding pocket layers	36267	35529	Solid	MAT_ENHANCED_COMPOSITE_DAMAGE
2-31	KFRP layers	12000×30	24442×30	Shell	MAT_LAMINATED_COMPOSITE_FABRIC
100	Bullet	34503	36564	Solid	MAT_ELASTIC_PLASTIC_HYDRO

4.4.2 Ballistic behavior of BGPAP

The simulation results for BGPAP has been analyzed and the BGPAP found to have an excellent ballistic behavior compared with others. Accordingly, the bullet guiding pocket allow the bullet to slide easily through CFRP layers guided path. The bullet guiding pocket affects significantly the performance of BGPAP. Consequently, the bullet is stopped and contained inside the KFRP layers, while experienced very large deformation. The computed BFS is found to be within the acceptable limit, as per NIJ standard [80]. The significant deformation in bullet, leads to considerable reduction in its kinetic energy as shown to Figure 4-25. The bullet had stopped at BFS of 19.6 mm stroke. Figure 4-26 shows a section front view of the deformation history together with its total energy absorption contours. Delamination between the CFRP layers and KFRP layers was observed to be a consequence of deformation, matrix cracking and fiber breakage in the CFRP layers. The bullet guiding pocket had dissipated a huge amount of the bullet's kinetic energy by deforming the bullet. KFRP layers had supported the CFRP in a good way so no complete penetration in BGPAP was observed.

4.5   Summary

In this chapter, the results of the ballistic real shooting test of the fabricated flat and curved body armor plates has been presented and discussed in details at two levels; the macro and micro levels. By comparing the experimental and numerical simulation results, a very good correlation has been achieved. Furthermore, materials stacking sequence was found to play a significant role in dissipating the bullet's kinetic energy. In addition, the ballistic behavior of the bullet guiding pockets has been presented and discussed for both CFRP and KFRP samples. Sliding crush behavior of CFRP and KFRP bullet guiding pockets has

been found to be very sensitive to the change in conical angles. Bullet guiding pockets made of CFRP absorbed more energy than KFRP based bullet guiding pockets. The newly developed bullet guiding body armor displayed an excellent ballistic behavior.
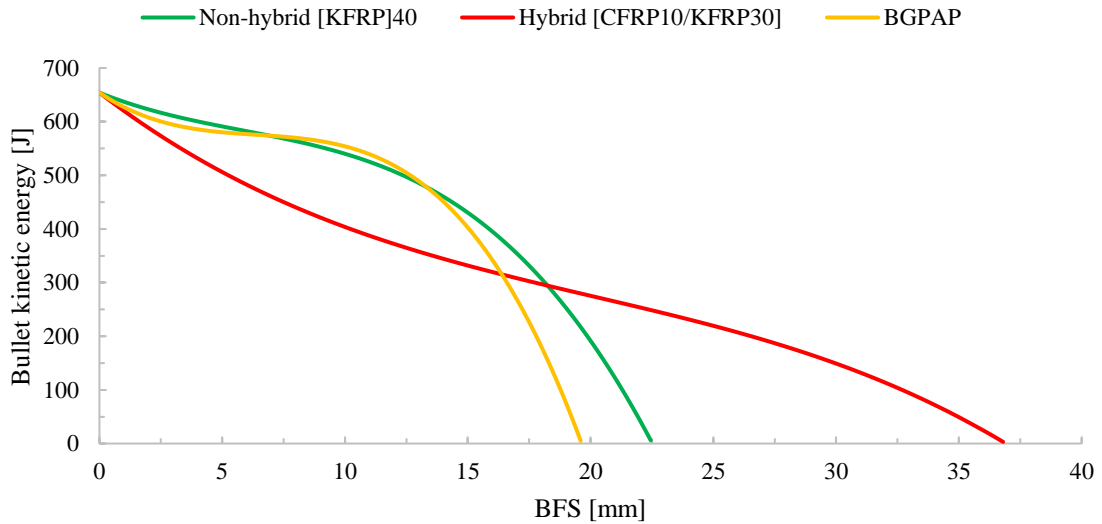
Figure 4-25: Comparison between bullet internal energy-BFS curves for simulated armor plates.
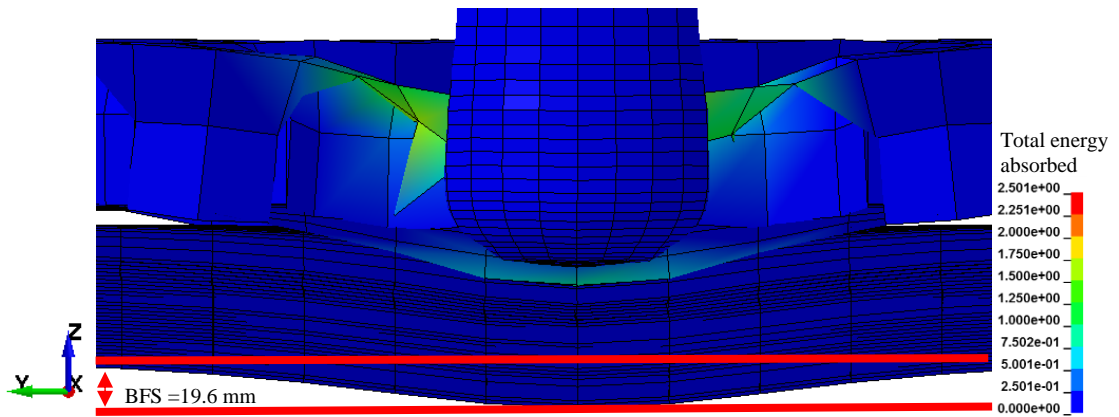
Figure 4-26: Section view of the BGPAP with respect to total energy absorption contours.

CHAPTER 5

CONCLUSION AND RECOMMENDATIONS

5.1   Conclusion

The preceding chapters highlighted and covered most of the work carried out throughout this study; namely the experimental and finite element simulation using ANSYS/LS-DYNA. There are two main contributions can be achieved from this study. First is the introduction of hybridization of composite with proper material stacking sequence as a new candidate in the field of body armor protection. Second, integrating the bullet guiding pockets in the design of hybrid body armor. Based on the results and discussion of experimental and numerical programs, the following remarks can be concluded as:

1. The ballistic behavior of flat and curved body armors has been found to be identical.

2. Material stacking sequence has affected significantly the energy dissipation mechanism, energy absorption capability of hybrid composite body armor.

3. Body armor with [$CFRP_{10}/KFRP_{30}$] material sequence displayed the highest energy absorption capability and passed the ballistic real shooting test. As the CFRP layers had reduced the bullet's kinetic energy and decelerated its speed, while the thirty layers of KFRP had stopped the bullet due to the Kevlar ballistic properties.

4. On the other hand, body armors with [$CFRP_4/KFRP_6$]$_4$ had displayed poor energy dissipation mechanism and did not pass the ballistic real shooting. Since the KFRP layers were not enough to stop the bullet and arrest it between the layers.

5. Incorporating the untreated date palm natural fiber composites in the material sequence of body armor displayed promising ballistic behavior, although did not pass all the three-trial real shooting test.

6. Introducing bullet guiding pockets in the design of body armors have a significant effect on their sliding crush behavior.

7. Similar trends have been observed for both CFRP and KFRP bullet guiding pockets.

8. Designing the bullet guiding pockets within the CFRP layers displayed the highest energy absorption capability compared with KFRP layers, due to the high weight-strength-ratio property of CFRP.

9. Bullet guiding pocket conical angles has been optimized, and specimens with 50° had the highest specific energy absorption capability in both CFRP and KFRP.

10. According to numerical results, the newly developed BGPAP showed an excellent ballistic performance against 9 mm bullet with BFS 19.6 mm.

11. The newly developed BGPAP showed 16% reduction in weight compared to the hybrid [CFRP$_{10}$/KFRP$_{30}$] armor plate.

5.2   Recommendations for Further Work

Some future recommendations can be listed as continuations to the current work:

1. Utilization of treated date palm fibers in the field of body armor protection. Since the body armor plate in which the untreated date palm fibers is integrated did not pass the real ballistic test. Because of the natural coating of the fibers, the date palm fibers could not absorb the epoxy in the fabricated plate which made the fibers weak against the impact.

2. Investigation of fiber orientation effect on ballistic behavior of hybrid and non-hybrid body armor plates.

3. Studying the effect of designed bullet path on the body armor plates.

4. Investigate the bullet striking angle on the ballistic behavior of bullet guiding pocket armor plate (BGPAP).

5. Study the effect of blunt trauma delivered to soldiers in bullet guiding pocket armor plate (BGPAP).

REFERENCES

1. Bhatnagar, A., *Lightweight ballistic composites: military and law-enforcement applications*. 2016: Woodhead Publishing.
2. Lakshmi, L. and C. Nandakumar, *Investigations on the Performance of Metallic and Composite Body Armors.* Procedia Technology, 2016. **25**: p. 170-177.
3. Brown, D., *US Troops' Injuries in Iraq Showed Body Armor's Value.* Washington Post, May, 2003. **4**: p. A28.
4. LaTourrette, T., *The life-saving effectiveness of body armor for police officers.* Journal of occupational and environmental hygiene, 2010. **7**(10): p. 557-562.
5. James, N., *Body armor for law enforcement officers: In brief.* 2016.
6. Wen, Y., et al., *Analysis of behind the armor ballistic trauma.* Journal of the mechanical behavior of biomedical materials, 2015. **45**: p. 11-21.
7. Lee, Y.S., E.D. Wetzel, and N.J. Wagner, *The ballistic impact characteristics of Kevlar® woven fabrics impregnated with a colloidal shear thickening fluid.* Journal of materials science, 2003. **38**(13): p. 2825-2833.
8. Farjo, L.A. and T. Miclau, *Ballistics and mechanisms of tissue wounding.* Injury, 1997. **28**: p. C12-C17.
9. Roberts, J.C., et al., *Modeling nonpenetrating ballistic impact on a human torso.* Johns Hopkins APL Technical Digest, 2005. **26**(1): p. 84-92.
10. *DEFSTAN 05-101(PT2)/1:2005* in *Proof of ordnance, munitions, armour and explosives: Part 2. Guidance*. 2005, UK Ministry of Defence Standards.
11. Thomas, E.L., *Opportunities in protection materials science and technology for future Army applications*. 2011: Wiley Online Library.
12. Montgomery, J.S. and E.S. Chin, *Protecting the Future Force-Towards A New Generation Of Metallic Structural Armour.* Military Technology, 2008. **32**(2): p. 110.
13. Vargas-Gonzalez, L.R. and J.C. Gurganus, *Hybridized composite architecture for mitigation of non-penetrating ballistic trauma.* International Journal of Impact Engineering, 2015. **86**: p. 295-306.
14. Scott, B., *New Ballistic Products and Technologies, Lighweight Ballistic Composites–Military and Law--enforcement Applications, ed. A. Bhatnager*. 2006, Woodhead Publishing Ltd., Cambrigde England.
15. Liu, W., et al., *Influence of different back laminate layers on ballistic performance of ceramic composite armor.* Materials & Design, 2015. **87**: p. 421-427.
16. Yuen, S.C.K. and G. Nurick, *The Use of Tubular Structures as Cores for Sandwich Panels Subjected to Dynamic and Blast Loading: A Current "State of the Art"*, in *Blast Mitigation*. 2014, Springer. p. 229-248.
17. Yuen, S.C. and G. Nurick, *The energy-absorbing characteristics of tubular structures with geometric and material modifications: an overview.* Applied Mechanics Reviews, 2008. **61**(2): p. 020802.
18. Xu, J., et al., *Crashworthiness of carbon fiber hybrid composite tubes molded by filament winding.* Composite Structures, 2016. **139**: p. 130-140.

19. Esnaola, A., et al., *Quasi-static crush energy absorption capability of E-glass/polyester and hybrid E-glass–basalt/polyester composite structures.* Materials & Design, 2015. **76**: p. 18-25.

20. Esnaola, A., et al., *Design, manufacturing and evaluation of glass/polyester composite crash structures for lightweight vehicles.* International Journal of Automotive Technology, 2016. **17**(6): p. 1013-1022.

21. Liu, Q., et al., *Quasi-static axial crushing and transverse bending of double hat shaped CFRP tubes.* Composite Structures, 2014. **117**: p. 1-11.

22. Fu, Y., J. Zhou, and X. Gao, *Design and numerical simulation of a new sandwiched sphere structure for ballistic protection.* International Journal of Impact Engineering, 2013. **58**: p. 66-75.

23. Carr, D., *Ballistic-protective clothing and body armour.* Protective Clothing: Managing Thermal Stress, 2014: p. 146.

24. Mountford, R., *Modern Body Armour and Helmets: An Introduction [Book Review].* Journal of Battlefield Technology, 2006. **9**(3): p. 40.

25. Williams, A.R., *The knight and the blast furnace: a history of the metallurgy of armour in the Middle Ages & the early modern period*. Vol. 12. 2003: Brill.

26. Scott, R.A., *Textiles for protection*. 2005: Elsevier.

27. Ma, Z.-D., et al., *Designing an innovative composite armor system for affordable ballistic protection*. 2006, DTIC Document.

28. Dean, B., *Helmets and body armor in modern warfare*. 1920: Metropolitan Museum of Art.

29. Restle, S., *Ballistische Schutzwesten und Stichschutzoptionen*. 2004: Kabinett Verlag.

30. Agrawal, B.J. *High performance textiles for ballistic protection*. in *Defense Science Research Conference and Expo (DSR), 2011*. 2011. IEEE.

31. Estes, K., *US Army Soldier: Baghdad 2003-04*. 2012: Bloomsbury Publishing.

32. Horrocks, A.R. and S.C. Anand, *Handbook of technical textiles*. 2000: Elsevier.

33. Bajaj, P. and Sriram, *Ballistic protective clothing-An overview*. INDIAN JOURNAL OF FIBRE AND TEXTILE RESEARCH, 1997. **22**: p. 274-291.

34. Scott, R.A., *Textiles in defence*. 2000: Woodhead Publishing, Cambridge, UK.

35. Ogin, S.L. and P. Potluri, *Textile-reinforced composite materials.* Handbook of Technical Textiles: Technical Textile Applications, 2016. **2**: p. 1.

36. Bautista, L., *Ballistic and impact protection finishes for textiles*, in *Functional Finishes for Textiles*. 2015, Woodhead Publishing: Barcelona. p. 579-606.

37. Brayley, M., *Modern body armour*. 2011: Crowood.

38. Gotts, P.L., *Development of a lightweight combat explosive ordnance disposal suit*, in *Personal Armour Systems Symposium*. 2000, Defence Clothing and Textiles Agency, Science and Technology Division, MoD: Colchester.

39. Marsden, A., *UK body armour and helmets*, in *Personal Armour Systems Symposium*. 1994: Colchester. p. 21-25.

40. C. Roberson, P.L.G., *Review of hard armour materials and their use in future personal armour applications*, in *Personal armour systems symposium*. 2004, TNO Prins Maurits Laboratory: The Hague, The Netherlands.

41. Lewis, E. *Between Iraq and a hard plate: recent developments in UK military personal armour*. in *Personal armour systems symposium*. 2006.

42.   Department of Defense Inspector General, *DoD Testing Requirements for Body Armor*. 2009.

43.   Hou, S., et al., *Experimental and numerical studies on multi-layered corrugated sandwich panels under crushing loading.* Composite Structures, 2015. **126**: p. 371-385.

44.   Palanivelu, S., et al., *Crushing and energy absorption performance of different geometrical shapes of small-scale glass/polyester composite tubes under quasi-static loading conditions.* Composite structures, 2011. **93**(2): p. 992-1007.

45.   Yuen, S.C.K., et al., *Sandwich panels subjected to blast loading*, in *Dynamic failure of materials and structures*. 2009, Springer. p. 297-325.

46.   Yuen, S.C.K., G. Nurick, and H. Witbeen, *The response of sandwich panels made of thin-walled tubes subjected to axial load.* International Journal of Protective Structures, 2011. **2**(4): p. 477-498.

47.   Alghamdi, A., *Collapsible impact energy absorbers: an overview.* Thin-walled structures, 2001. **39**(2): p. 189-213.

48.   Mahdi, E. and A. Hamouda, *Energy absorption capability of composite hexagonal ring systems.* Materials & Design, 2012. **34**: p. 201-210.

49.   Johnson, W. and S. Reid, *Metallic energy dissipating systems.* Appl. Mech. Rev, 1978. **31**(3): p. 277-288.

50.   Khanchehzar, P., A. Niknejad, and S.G. Amirhosseini, *Influences of different internal stiffeners on energy absorption behavior of square sections during the flattening process.* Thin-Walled Structures, 2016. **107**: p. 462-472.

51.   Gupta, N. and A. Khullar, *Lateral collapse of orthogonal and non-orthogonal cross-layered arrays of square and rectangular tubes.* International journal of mechanical sciences, 1994. **36**(5): p. 449-467.

52.   Gupta, N. and A. Khullar, *Collapse load analysis of square and rectangular tubes subjected to transverse in-plane loading.* Thin-walled structures, 1995. **21**(4): p. 345-358.

53.   Gupta, N., G. Sekhon, and P. Gupta, *A study of lateral collapse of square and rectangular metallic tubes.* Thin-walled structures, 2001. **39**(9): p. 745-772.

54.   Sun, G., et al., *Experimental study on crashworthiness of empty/aluminum foam/honeycomb–filled CFRP tubes.* Composite Structures, 2016.

55.   Alexander, J., *An approximate analysis of the collapse of thin cylindrical shells under axial loading.* The Quarterly Journal of Mechanics and Applied Mathematics, 1960. **13**(1): p. 10-15.

56.   Gupta, N., G. Sekhon, and P. Gupta, *Study of lateral compression of round metallic tubes.* Thin-walled structures, 2005. **43**(6): p. 895-922.

57.   Mahdi, E. and T. Sebaey, *Crushing behavior of hybrid hexagonal/octagonal cellular composite system: Aramid/carbon hybrid composite.* Materials & Design, 2014. **63**: p. 6-13.

58.   Sebaey, T., et al., *Crushing behavior of hybrid hexagonal/octagonal cellular composite system: All made of carbon fiber reinforced epoxy.* Materials & Design, 2014. **60**: p. 556-562.

59.   Alkbir, M., et al., *Effect of geometry on crashworthiness parameters of natural kenaf fibre reinforced composite hexagonal tubes.* Materials & Design, 2014. **60**: p. 85-93.

60. Lin, J., X. Wang, and G. Lu, *Crushing characteristics of fiber reinforced conical tubes with foam-filler.* Composite Structures, 2014. **116**: p. 18-28.

61. Mahdi, E., et al., *An experimental investigation into crushing behaviour of filament-wound laminated cone–cone intersection composite shell.* Composite structures, 2001. **51**(3): p. 211-219.

62. Gao, Q., et al., *Optimization of foam-filled double ellipse tubes under multiple loading cases.* Advances in Engineering Software, 2016. **99**: p. 27-35.

63. Yu, B., et al., *Graded square honeycomb as sandwich core for enhanced mechanical performance.* Materials & Design, 2016. **89**: p. 642-652.

64. Menna, C., et al., *Numerical assessment of the impact behavior of honeycomb sandwich structures.* Composite Structures, 2013. **106**: p. 326-339.

65. Palanivelu, S., et al., *Comparison of the crushing performance of hollow and foam-filled small-scale composite tubes with different geometrical shapes for use in sacrificial cladding structures.* Composites Part B: Engineering, 2010. **41**(6): p. 434-445.

66. Palanivelu, S., et al., *Comparative study of the quasi-static energy absorption of small-scale composite tubes with different geometrical shapes for use in sacrificial cladding structures.* Polymer Testing, 2010. **29**(3): p. 381-396.

67. Palanivelu, S., et al., *Parametric study of crushing parameters and failure patterns of pultruded composite tubes using cohesive elements and seam, Part I: Central delamination and triggering modelling.* Polymer Testing, 2010. **29**(6): p. 729-741.

68. Palanivelu, S., et al., *Experimental study on the axial crushing behaviour of pultruded composite tubes.* Polymer testing, 2010. **29**(2): p. 224-234.

69. Palanivelu, S., et al., *Close-range blast loading on empty recyclable metal beverage cans for use in sacrificial cladding structure.* Engineering Structures, 2011. **33**(6): p. 1966-1987.

70. Palanivelu, S., et al., *Parametric study of crushing parameters and failure patterns of pultruded composite tubes using cohesive elements and seam, Part II: Multiple delaminations and initial geometric imperfections.* Polymer Testing, 2010. **29**(7): p. 803-814.

71. Guruprasad, S. and A. Mukherjee, *Layered sacrificial claddings under blast loading Part II—experimental studies.* International Journal of Impact Engineering, 2000. **24**(9): p. 975-984.

72. Guruprasad, S. and A. Mukherjee, *Layered sacrificial claddings under blast loading Part I—analytical studies.* International Journal of Impact Engineering, 2000. **24**(9): p. 957-973.

73. Hanssen, A., L. Enstock, and M. Langseth, *Close-range blast loading of aluminium foam panels.* International Journal of Impact Engineering, 2002. **27**(6): p. 593-618.

74. Shockey, D.A., D.C. Erlich, and J.W. Simons, *Improved barriers to turbine engine fragments: interim report III.* 2001, DTIC Document.

75. Kocer, H., *Laminated and Hybrid Soft Body Armor for Ballistic Applications.* 2007.

76. Shim, V., C. Lim, and K. Foo, *Dynamic mechanical properties of fabric armour.* International Journal of Impact Engineering, 2001. **25**(1): p. 1-15.

77. Wilde, A.F., D.K. Roylance, and J.P.M. Rogers, *Photographic Investigation of High-Speed Missile Impact upon Nylon Fabric Part I: Energy Absorption and Cone Radial Velocity in Fabric.* Textile Research Journal, 1973. **43**(12): p. 753-761.

78. Standard, M., *V50 Ballistic Test for Armor*. 1984, MIL-STD-662E. Department of Defense.

79. Figucia, F., *Energy absorption of Kevlar fabrics under ballistic impact.* US Army Natick Research and Development Command, 1980.

80. NIJ Standards, U.S.D.o.J., *Ballistic Resistance of Personal Body Armor NIJ Standard-0101.06*. July 2008.

81. Roberts, J.C., et al., *Assessing behind armor blunt trauma in accordance with the National Institute of Justice Standard for Personal Body Armor Protection using finite element modeling.* Journal of Trauma and Acute Care Surgery, 2007. **62**(5): p. 1127-1133.

82. Cheeseman, B.A. and T.A. Bogetti, *Ballistic impact into fabric and compliant composite laminates.* Composite structures, 2003. **61**(1): p. 161-173.

83. Shahkarami, A., et al., *Material responses to ballistic impact.* Lightweight ballistic composites, Woodhead Publishing, 2006: p. 72-100.

84. Prosser, R.A., S.H. Cohen, and R.A. Segars, *Heat as a factor in the penetration of cloth ballistic panels by 0.22 caliber projectiles.* Textile Research Journal, 2000. **70**(8): p. 709-722.

85. Cunniff, P.M. *Dimensionless parameters for optimization of textile-based body armor systems*. in *Proceedings of the 18th International and Symposium on Ballistics*. 1999.

86. Roylance, D. and S.-S. Wang, *Influence of fibre properties on ballistic penetration of textile panels.* Fibre Science and Technology, 1981. **14**(3): p. 183-190.

87. Song, W.J., *Fabrics and Composites for the Ballistic Protection of Personnel*, in *Lightweight Ballistic Composite*, A. Bhatnagar, Editor. 2006, Woodhead publishing and Maney publishing limited.

88. Lee, B., J. Song, and J. Ward, *Failure of Spectra® polyethylene fiber-reinforced composites under ballistic impact loading.* Journal of Composite Materials, 1994. **28**(13): p. 1202-1226.

89. Lee, B., et al., *Penetration failure mechanisms of armor-grade fiber composites under impact.* Journal of Composite Materials, 2001. **35**(18): p. 1605-1633.

90. Zeng, X., V. Tan, and V. Shim, *Modelling inter-yarn friction in woven fabric armour.* International Journal for Numerical Methods in Engineering, 2006. **66**(8): p. 1309-1330.

91. Briscoe, B. and F. Motamedi, *The ballistic impact characteristics of aramid fabrics: the influence of interface friction.* Wear, 1992. **158**(1-2): p. 229-247.

92. Tan, V., T. Tay, and W. Teo, *Strengthening fabric armour with silica colloidal suspensions.* International journal of solids and structures, 2005. **42**(5): p. 1561-1576.

93. Lee, B.-W., I.-J. Kim, and C.-G. Kim, *The influence of the particle size of silica on the ballistic performance of fabrics impregnated with silica colloidal suspension.* Journal of composite materials, 2009.

94. Barnes, H., *Shear-thickening ("Dilatancy") in suspensions of nonaggregating solid particles dispersed in Newtonian liquids.* Journal of Rheology (1978-present), 1989. **33**(2): p. 329-366.

95. Tan, V., C. Lim, and C. Cheong, *Perforation of high-strength fabric by projectiles of different geometry.* International Journal of Impact Engineering, 2003. **28**(2): p. 207-222.

96. Beckwith, S.W. and C.R. Hyland, *Resin transfer molding: a decade of technology advances.* Sampe Journal, 1998. **34**(6): p. 7-19.

97. Summerscales, J. and T. Searle, *Low-pressure (vacuum infusion) techniques for moulding large composite structures.* Proceedings of the Institution of Mechanical Engineers, Part L: Journal of Materials Design and Applications, 2005. **219**(1): p. 45-58.

98. Bader, S., *Crystic composites handbook.* Wollaston: Scott Bader Company, 2005: p. 45.

99. Mallick, P.K., *Fiber-reinforced composites: materials, manufacturing, and design.* 2007: CRC press.

100. Dons, K., *Filament winding of composite tubes.* 2013.

101. Campbell Jr, F.C., *Manufacturing processes for advanced composites.* 2003: Elsevier.

102. Kaw, A.K., *Mechanics of composite materials.* 2005: CRC press.

103. Matzenmiller, A., J. Lubliner, and R. Taylor, *A constitutive model for anisotropic damage in fiber-composites.* Mechanics of materials, 1995. **20**(2): p. 125-152.

104. Manual, L.-D.K.U.s., *Version 971.* Livermore Software Technology Corporation, 2007. **7374**.

105. Chang, F.-K. and K.-Y. Chang, *Post-failure analysis of bolted composite joints in tension or shear-out mode failure.* Journal of Composite Materials, 1987. **21**(9): p. 809-833.

106. Pinho, S.T., et al., *Failure models and criteria for FRP under in-plane or three-dimensional stress states including shear non-linearity.* 2005.

107. Andersson, M. and P. Liedberg, *Crash behavior of composite structures.* A CAE benchmarking study [Master's thesis in Applied Mechanics]. Chalmers University of Technology. Göteborg, Sweden, 2014.

108. Agarwal, B.D., L.J. Broutman, and K. Chandrashekhara, *Analysis and performance of fiber composites.* 2006: John Wiley & Sons.

109. Geubelle, P.H. and J.S. Baylor, *Impact-induced delamination of composites: a 2D simulation.* Composites Part B: Engineering, 1998. **29**(5): p. 589-602.

110. Hashin, Z., *Failure criteria for unidirectional fiber composites.* Journal of applied mechanics, 1980. **47**(2): p. 329-334.

111. Lee, S.M., *Handbook of composite reinforcements.* 1992: John Wiley & Sons.

112. Lubin, G., *Handbook of composites.* 2013: Springer Science & Business Media.

APPENDIX A

MECHANICAL PROPERTIES

Mechanical properties of used woven carbon-fiber/epoxy and Kevlar/epoxy in the body armor plates.

Table A.1: Woven CFRP and woven KFRP mechanical properties [111, 112]

Mechanical property	Woven CFRP	Woven KFRP	Unit
Mass density (ρ)	1.6e-6	1.44e-6	kg/mm^3
Young's Modulus in a-direction and b-direction ($E_{11}= E_{22}$)	175	18.5	GPa
Young's Modulus in c-direction (E_{33})	8.8	6	GPa
Shear modulus in ab-direction (G_{12})	5.5	1	GPa
Shear modulus ($G_{23}=G_{31}$)	2.5	5.43	GPa
Major Poisson's ratio (v_{12})	0.3	0.25	-
Minor Poisson's ratio ($v_{31}= v_{32}$)	0.02545	0.33	-
Longitudinal compressive strength	850	190	MPa
Longitudinal tensile strength	1000	480	MPa
Transverse compressive strength	850	190	MPa
Transverse tensile strength	1000	480	MPa
In-plane Shear strength	670	50	MPa
Longitudinal compressive strain	0.8	0.6	%
Longitudinal tensile strain	0.85	1.6	%
Transverse compressive strain	0.8	0.6	%
Transverse tensile strain	0.85	1.6	%
In-plane shear strain	1.8	1	%
Thermal expansion coefficient 0°	2.1	7.4	strain/K
Thermal expansion coefficient 90°	2.1	7.4	strain/K

Mechanical properties of used ABS (Acrylonitrile butadiene styrene) plastic for the 3D printed cones.

Table A.2: ABS plastic mechanical properties

Mechanical property	ABS plastic	Unit
Mass density (ρ)	1.04e-6	kg/mm^3
Young's Modulus (E)	2.2	GPa
Shear modulus (G)	0.9	GPa
Poisson's ratio (ν)	0.36	-
Yield stress	43	MPa
Ultimate tensile strength (UTS)	35	MPa
Fracture toughness (KIC)	2.3	MPa*m ^ (1/2)
Bulk modulus	3.8	GPa
Compressive strength	55	MPa
Elongation	1.5	%

Mechanical properties of used UD carbon-fiber/epoxy and UD Kevlar/epoxy in the bullet guiding pockets.

Table A.3: UD Carbon fiber/epoxy and UD Kevlar®/epoxy mechanical properties [111, 112]

Mechanical property	UD CFRP/epoxy	UD KFRP/epoxy	Unit
Mass density (ρ)	1.6e-6	1.3e-6	kg/mm^3
Young's Modulus in a-direction (E_{11})	135	75	GPa
Young's Modulus in b-direction (E_{22})	10	6	GPa
Shear modulus ($G_{12}=G_{23}=G_{31}$)	5	1.055	GPa
Major Poisson's ratio (v_{12})	0.309	0.34	-
Minor Poisson's ratio ($v_{31}=v_{32}$)	0.02049	0.0193	-
Longitudinal compressive strength	1200	300	MPa
Longitudinal tensile strength	1500	1300	MPa
Transverse compressive strength	250	140	MPa
Transverse tensile strength	50	30	MPa
In-plane shear strength	90	60	MPa
Inter-laminar shear strength	128	60	MPa
Longitudinal compressive strain	0.9	0.35	%
Longitudinal tensile strain	1.4	1.7	%
Transverse compressive strain	1.6	2.3	%
Transverse tensile strain	0.67	0.5	%
In-plane shear strain	2	3	%

APPENDIX B

INPUT PARAMETERS IN ANSYS/LS-DYNA MATERIAL MODELS

Table B.1: Description of input parameters in MAT_010

Variable	Definition
MID	Material identification number
RO	Mass density, ρ
G	Shear modulus
SIGY	Yield stress
EH	Plastic hardening modulus
PC	Pressure cutoff (≤ 0.0), if zero a cutoff of $-\infty$ is assumed
FS	Failure strain for erosion
CHARL	Characteristic element thickness for deletion
A1	Linear pressure hardening coefficient
A2	Quadratic pressure hardening coefficient
SPALL	Spall type: EQ.0.0: default set to "1.0", EQ.1.0: $p \geq p_{min}$ EQ.2.0: if $\sigma_{max} \geq -p_{min}$ element spalls and tension, $p < 0$ is never allowed. EQ.3.0: if $\sigma_{max} < -p_{min}$ element spalls and tension, $p < 0$ is never allowed.
EPS	Effective plastic strain, up to 16 values
ES	Effective stress, up to 16 values

Table B.2: Description of input parameters in MAT_20

Variable	Definition
MID	Material identification number
RO	Mass density, ρ
E	Young's modulus, E
PR	Poisson's ratio, v
N	MADYMO3D 5.4 coupling flag, n: EQ.0: use normal LS-DYNA rigid body updates, GT.0: the rigid body is coupled to MADYMO 5.4 ellipsoid number n, LT.0: the rigid body is coupled to MADYMO 5.4 plane number n. Coupling option if applicable: EQ.-1: attach VDA surface in ALIAS (defined in the eight field) and automatically generate a mesh for viewing the surface in LS-PREPOST.
COUPLE	MADYMO 5.4 /CAL3D coupling option: EQ.0: the undeformed geometry input to LS-DYNA corresponds to the local system for MADYMO 5.4 /CAL3D. the finite element mesh is input. EQ.1: the undeformed geometry input to LS-DYNA corresponds to the global system for MADYMO 5.4 /CAL3D. EQ.2: generate a mesh for the ellipsoids and planes internally in LS-DYNA.
M	MADYMO3D 5.4 coupling flag, m: EQ.0: use normal LS-DYNA rigid body updates, EQ.m: the rigid body corresponds to MADYMO rigid body number m. rigid body updates are performed by MADYMO, LT.0: the rigid body is coupled to MADYMO 5.4 plane number n.
ALIAS	VDA surface alias name.
CMO	Center of mass constraint option, CMO: EQ.+1: constraints applied in global direction, EQ.0.0: no constraints, EQ.-1: constraints applied in local directions.
CON1	First constraint parameter: If CMO=+1, then specify global translational constraint: EQ.0: no constraints, EQ.1: constrained x displacement, EQ.2: constrained y displacement, EQ.3: constrained z displacement, EQ.4: constrained x and y displacements, EQ.5: constrained y and z displacements, EQ.6: constrained z and x displacements, EQ.7: constrained x, y, and z displacements, If CMO=-1, then specify local coordinate system ID.

CON2	Second constraint parameter:
	 <u>If CMO=+1, then specify global rotational constraint:</u>
	     EQ.0: no constraints,
	     EQ.1: constrained x rotation,
	     EQ.2: constrained y rotation,
	     EQ.3: constrained z rotation,
	     EQ.4: constrained x and y rotations,
	     EQ.5: constrained y and z rotations,
	     EQ.6: constrained z and x rotations,
	     EQ.7: constrained x, y, and z rotations,
	 <u>If CMO=-1, then specify local (SPC) constraint.</u>
	     EQ.000000: no constraints,
	     EQ.100000: constrained x translation,
	     EQ.010000: constrained y translation,
	     EQ.001000: constrained z translation,
	     EQ.000100: constrained x rotation,
	     EQ.000010: constrained y rotation,
	     EQ.000001: constrained z rotation.

LCO	Local coordinate system number for output
A1-V3	Define two vectors $\mathbf{a}$ and $\mathbf{v}$, fixed in the rigid body which are used for output. The output parameters are in the direction $\mathbf{a}$, $\mathbf{b}$ and $\mathbf{c}$ where the latter are given by the cross products $\mathbf{c}=\mathbf{a}\times\mathbf{v}$ and $\mathbf{b}=\mathbf{c}\times\mathbf{a}$.

Table B.3: Description of input parameters in MAT_024

Variable	Definition
MID	Material identification number
RO	Mass density, ρ
E	Young's modulus, E
PR	Poisson's ratio, v
SIGY	Yield stress
ETAN	Tangent modulus

FAIL	Failure flag:
	    LT.0.0: user defined failure subroutine is called to determine failure.
	    EQ.0.0: failure is considered.
	    GT.0.0: plastic strain to failure.

TDEL	Minimum time step size for automatic element deletion.
C	Strain rate parameter C.
P	Strain rate parameter P.
LCSS	Load curve ID or Table ID.
LCSR	Load curve ID defining strain rate scaling effect on yield stress.

VP	Formulation for rate effects:
	    EQ.-1.0: Cowper-Symonds with deviatoric strain rate rather than total.
	    EQ.0.0: scale yield stress.
	    EQ.1.0: viscoplastic formulation.

EPS1-EPS8	Effective plastic strain values.
ES1-ES8	Corresponding yield stress values to EPS1-EPS8.

Table B.4: Description of input parameters in MAT_054/055

Variable	Definition
MID	Material identification number
RO	Mass density, ρ
EA	Young's modulus in longitudinal direction, E_a
EB	Young's modulus in transverse direction, E_b
(EC)	Young's modulus in normal direction, E_c
PRBA	Minor Poisson's ratio in ba-direction, v_{ba}
PRBC	Minor Poisson's ratio in bc-direction, v_{bc}
(PRCB)	Minor Poisson's ratio in cb-direction, v_{cb}
GAB	Shear modulus in ab-direction, G_{ab}
GBC	Shear modulus in bc-direction, G_{bc}
GCA	Shear modulus in ca-direction, G_{ca}
(KF)	Bulk modulus of failed material
AOPT	Material axes option EQ.0.0: locally orthotropic with material axes determined by element nodes 1,2, and 4, as with *DEFINE_COORDINATE_NODES. EQ.2.0: globally orthotropic with material axes determined by vectors defined below as with *DEFINE_COORDINATE_VECTOR. EQ.3.0: locally orthotropic with material axes determined by rotating the material axes about the element normal by an angle (MANGLE) from a line in the plane of the element defined by the cross product of the vector v with the element normal. LT.0.0: the absolute value of AOPT is a coordinate system ID number (CID on *DEFINE_COORDINATE_NODES, *DEFINE_COORDINATE_SYSTEM, or *DEFINE_COORDINATE_VECTOR).
A1, A2, A3	Components of vector A, for AOPT=2.
V1, V2, V3	Components of vector V, for AOPT=3.
D1, D2, D3	Components of vector D, for AOPT=2.

MANGLE	Material angle in degrees, for AOPT=3.
DFAILM	Maximum strain for matrix straining in both tension and compression
DFAILS	Maximum tensorial shear strain
TFAIL	Time step size for element deletion
ALPH	Shear stress parameter for non-linear term, α
SOFT	Softening reduction factor for material strength in crashfront elements

FBRT	Softening parameter for fiber tensile strength:
	  EQ.0.0: tensile strength = X_t
	  GT.0.0: tensile strength = X_t, reduced to $X_t \times FBRT$ after failure has occurred in compressive matrix mode.

YCFAC	Reduction factor for compressive fiber strength after failure has occurred in compressive matrix mode
DFAILT	Maximum strain for fiber tension
DFAILC	Maximum strain for fiber compression
EFS	Effective failure strain
XC	Longitudinal compressive strength, X_c
XT	Longitudinal tensile strength, X_t
YC	Transverse compressive strength, Y_c
YT	Transverse tensile strength, Y_t
SC	Shear strength, S_c

CRIT	Failure criteria (material number) to use:
	  EQ.54.0: Chang matrix criterion.
	  EQ.55.0: Tsai-Wu criterion for matrix failure.

BETA	Weighing factor for shear term in tensile fiber mode, β
PEL	Percentage of layer needed to fail until crashfront is initiated and strength is reduced in neighboring elements
EPSF	Damage initiation transverse shear strain

EPSR	Final rapture transverse shear strain
TSMD	Transverse shear maximum damage
SOFT2	Optional orthogonal softening reduction factor. When active, SOFT becomes parallel reduction factor
SLIMT1	Factor to determine minimum stress limit after maximum stress occurred for fiber tension
SLIMC1	Factor to determine minimum stress limit after maximum stress occurred for fiber compression
SLIMT2	Factor to determine minimum stress limit after maximum stress occurred for matrix tension
SLIMC2	Factor to determine minimum stress limit after maximum stress occurred for matrix compression
SLIMS	Factor to determine minimum stress limit after maximum stress occurred for shear
NCYRED	Number of cycles for stress reduction from maximum to minimum stress
SOFTG	Softening reduction factor for transverse shear stiffness for crashfront elements
LCXC	Load curve ID for XC vs strain rate. Will override parameter XC
LCXT	Load curve ID for XT vs strain rate. Will override parameter XT
LCYC	Load curve ID for YC vs strain rate. Will override parameter YC
LCYT	Load curve ID for YT vs strain rate. Will override parameter YT
LCSC	Load curve ID for SC vs strain rate. Will override parameter SC
DT	Strain rate averaging option

Table B.5: Description of input parameters in MAT_058

Variable	Definition
MID	Material identification number
RO	Mass density, ρ
EA	Young's modulus in longitudinal direction, E_a
EB	Young's modulus in transverse direction, E_b
(EC)	Young's modulus in normal direction, E_c
PRBA	Minor Poisson's ratio in ba-direction, v_{ba}
TAU1	$\tau1$, stress limit of the first slightly non-linear part of the shear stress versus shear strain curve
GAMMA1	$\gamma1$, strain limit of the first slightly non-linear part of the shear stress versus shear strain curve
GAB	Shear modulus in ab-direction, G_{ab}
GBC	Shear modulus in bc-direction, G_{bc}
GCA	Shear modulus in ca-direction, G_{ca}
SLIMT1	Factor to determine minimum stress limit after maximum stress occurred for fiber tension
SLIMC1	Factor to determine minimum stress limit after maximum stress occurred for fiber compression
SLIMT2	Factor to determine minimum stress limit after maximum stress occurred for matrix tension
SLIMC2	Factor to determine minimum stress limit after maximum stress occurred for matrix compression
SLIMS	Factor to determine minimum stress limit after maximum stress occurred for shear
AOPT	Material axes option EQ.0.0: locally orthotropic with material axes determined by element nodes 1,2, and 4, as with *DEFINE_COORDINATE_NODES. EQ.2.0: globally orthotropic with material axes determined by vectors defined below as with *DEFINE_COORDINATE_VECTOR. EQ.3.0: locally orthotropic with material axes determined by rotating the material axes about the element normal by an angle (BETA) from a line in the plane of the element defined by the cross product of the vector v with the element normal. LT.0.0: the absolute value of AOPT is a coordinate system ID number

TSIZE	Time step for automatic element deletion
ERODS	Maximum effective strain for element layer failure. A value of $1 = 100\%$ strain
SOFT	Softening reduction factor for strength in the crashfront
FS	Failure surface type
XP, YP, ZP	Define coordinate of point p for AOPT=1.
A1, A2, A3	Define Components of vector a, for AOPT=2.
V1, V2, V3	Define Components of vector v, for AOPT=3.
D1, D2, D3	Define Components of vector d, for AOPT=2.
MANGLE	Material angle in degrees, for AOPT=3.
E11C	Strain at longitudinal compressive strength, a-axis (positive)
E11T	Strain at longitudinal tensile strength, a-axis
E22C	Strain at transverse compressive strength, b-axis
E22T	Strain at transverse tensile strength, b-axis
GMS	Strain at shear strength, ab plane
XC	Longitudinal compressive strength, X_c
XT	Longitudinal tensile strength, X_t
YC	Transverse compressive strength, Y_c
YT	Transverse tensile strength, Y_t
SC	Shear strength, ab plane, S_c

APPENDIX C

MODELLING MATERIAL CARDS

Table C.1.a: MAT_054 values in material card for UD CFRP

Card 1	MID	RO	EA	EB	(EC)	PRBA	(PRCA)	(PRCB)
	1	1.6e-6	135	10	10	0.02049	0.02049	0.02049
Card 2	GAB	GBC	GCA	(KF)	AOPT			
	5	5	5	-	1			
Card 3	XP	YP	ZP	A1	A2	A3	MANGLE	
	-	-	-	-	-	-	-	
Card 4	V1	V2	V3	D1	D2	D3	DFAILM	DFAILS
	-	-	-	-	-	-	0	0
Card 5	TFAIL	ALPH	SOFT	FBRT	YCFAC	DFAILT	DFAILC	EPS
	8e-9	0.1	1	0.9	7	0.1	-0.1	-
Card 6	XC	XT	YC	YT	SC	CRIT	BETA	
	2.2	2.25	0.25	0.05	0.09	MAT54	0.1	
Card 7	PEL	EPSF	EPSR	TSMD	SOFT2			
	0	-	-	-	1			
Card 8	SLIMT1	SLIMC1	SLIMT2	SLIMC2	SLIMS	NCYRED	SOFTG	
	1	1	1	1	1	-	-	
Card 9	LCXC	LCXT	LCYX	LCYC	LCSC	DT		
	-	-	-	-	-	-		

Table C.1.b: MAT_054 values in material card for UD KFRP

Card 1	MID	RO	EA	EB	(EC)	PRBA	(PRCA)	(PRCB)
	1	1.3e-6	75	6	6	0.0193	0.0193	0.0193
Card 2	GAB	GBC	GCA	(KF)	AOPT			
	1	1	1	-	1			
Card 3	XP	YP	ZP	A1	A2	A3	MANGLE	
	-	-	-	-	-	-	-	
Card 4	V1	V2	V3	D1	D2	D3	DFAILM	DFAILS
	-	-	-	-	-	-	0	0
Card 5	TFAIL	ALPH	SOFT	FBRT	YCFAC	DFAILT	DFAILC	EPS
	8e-9	0.1	1	1	7	0.1	-0.2	-
Card 6	XC	XT	YC	YT	SC	CRIT	BETA	
	0.3	1.3	0.14	0.03	0.06	MAT54	0.1	
Card 7	PEL	EPSF	EPSR	TSMD	SOFT2			
	0	-	-	-	1			
Card 8	SLIMT1	SLIMC1	SLIMT2	SLIMC2	SLIMS	NCYRED	SOFTG	
	1	1	1	1	1	-	-	
Card 9	LCXC	LCXT	LCYX	LCYC	LCSC	DT		
	-	-	-	-	-	-		

Material cards used in modelling the woven CFRP and woven KFRP using MAT_058

Table C.2.a: MAT_058 values in material card for woven CFRP

Card 1	MID	RO	EA	EB	(EC)	PRBA	TAU1	GAMMA1
	1	1.6e-6	100	100	10	0.296	0	0
Card 2	GAB	GBC	GCA	SLIMT1	SLIMC1	SLIMT2	SLIMC2	SLIMS
	4.25	1.7	1.7	0.5	1	0.5	1	0.5
Card 3	AOPT	TSIZE	ERODS	SOFT	FS			
	0	0	0.95	0	1			
Card 4	XP	YP	ZP	A1	A2	A3		
	0	0	0	0	0	0		
Card 5	V1	V2	V3	D1	D2	D3	BETA	
	0	0	0	0	0	0	0	
Card 6	E11C	E11T	E22C	E22T	GMS			
	0.021	0.015	0.024	0.015	0.02			
Card 7	XC	XT	YC	YT	SC			
	0.22	0.015	0.22	0.015	0.087			

Table C.2.b: MAT_058 values in material card for woven KFRP

Card 1	MID	RO	EA	EB	(EC)	PRBA	TAU1	GAMMA1
	1	1.4e-6	18.5	18.5	6	0.343	0.0387	1.42e-7
Card 2	GAB	GBC	GCA	SLIMT1	SLIMC1	SLIMT2	SLIMC2	SLIMS
	1.055	1.055	1.055	0.815	0.749	0.612	0.772	0.326
Card 3	AOPT	TSIZE	ERODS	SOFT	FS			
	0	0	0	0	1			
Card 4	XP	YP	ZP	A1	A2	A3		
	0	0	0	0	0	0		
Card 5	V1	V2	V3	D1	D2	D3	BETA	
	0	0	0	0	0	0	0	
Card 6	E11C	E11T	E22C	E22T	GMS			
	0.051	0.047	0.051	0.047	0.11			
Card 7	XC	XT	YC	YT	SC			
	0.55	1.85	0.55	1.8	0.087			

APPENDIX D

OPTIMIZATION PARAMETRIC STUDY

Table D.1: Slipping force-stroke curves and eroded internal energy-time curves obtained from ELFORM parametric study
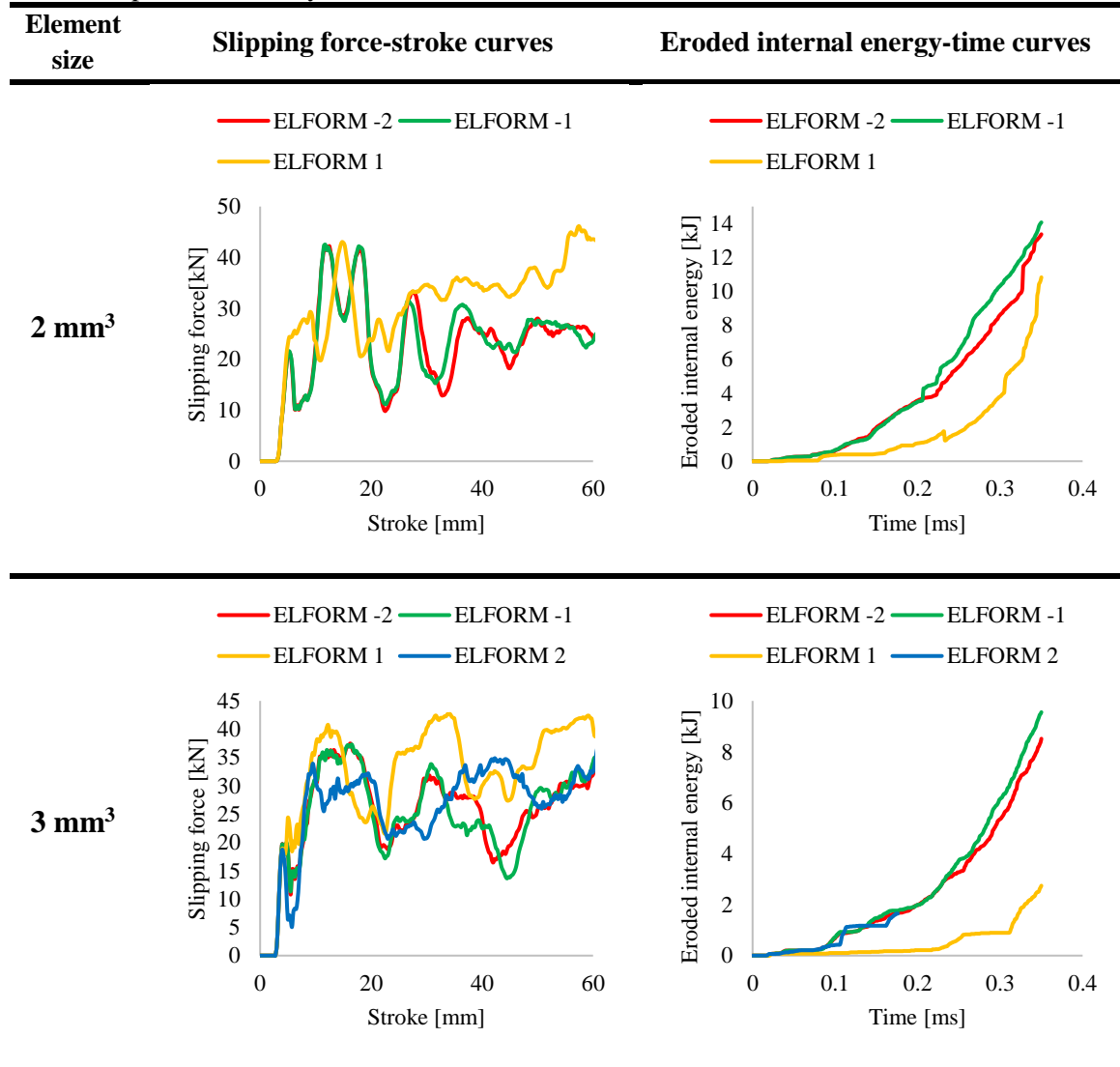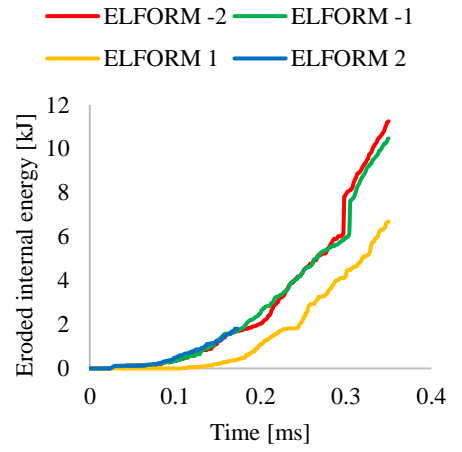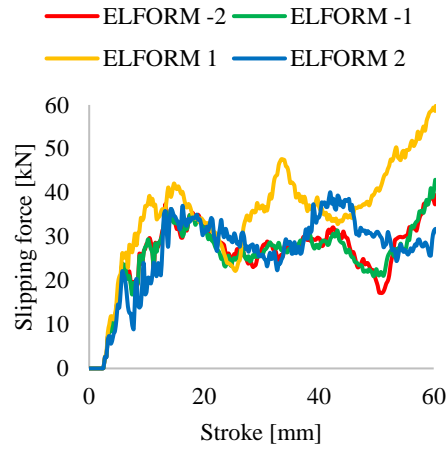
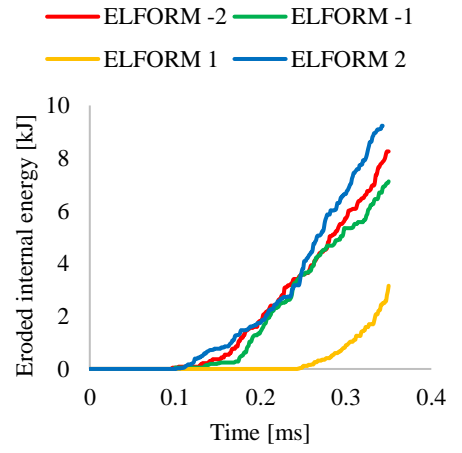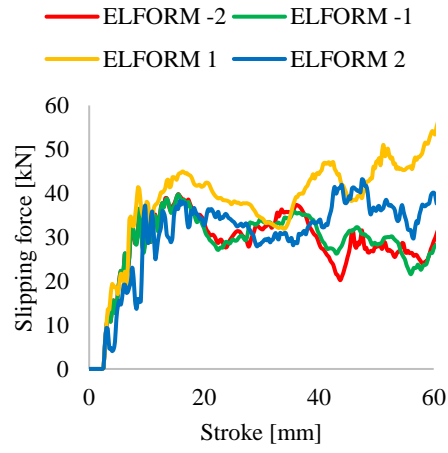| Element size	Slipping force-stroke curves	Eroded internal energy-time curves
2 mm³		
3 mm³		

Table D.2: Representative pictures under total energy absorbed during three different deformation history for the five element sizes that were studied.
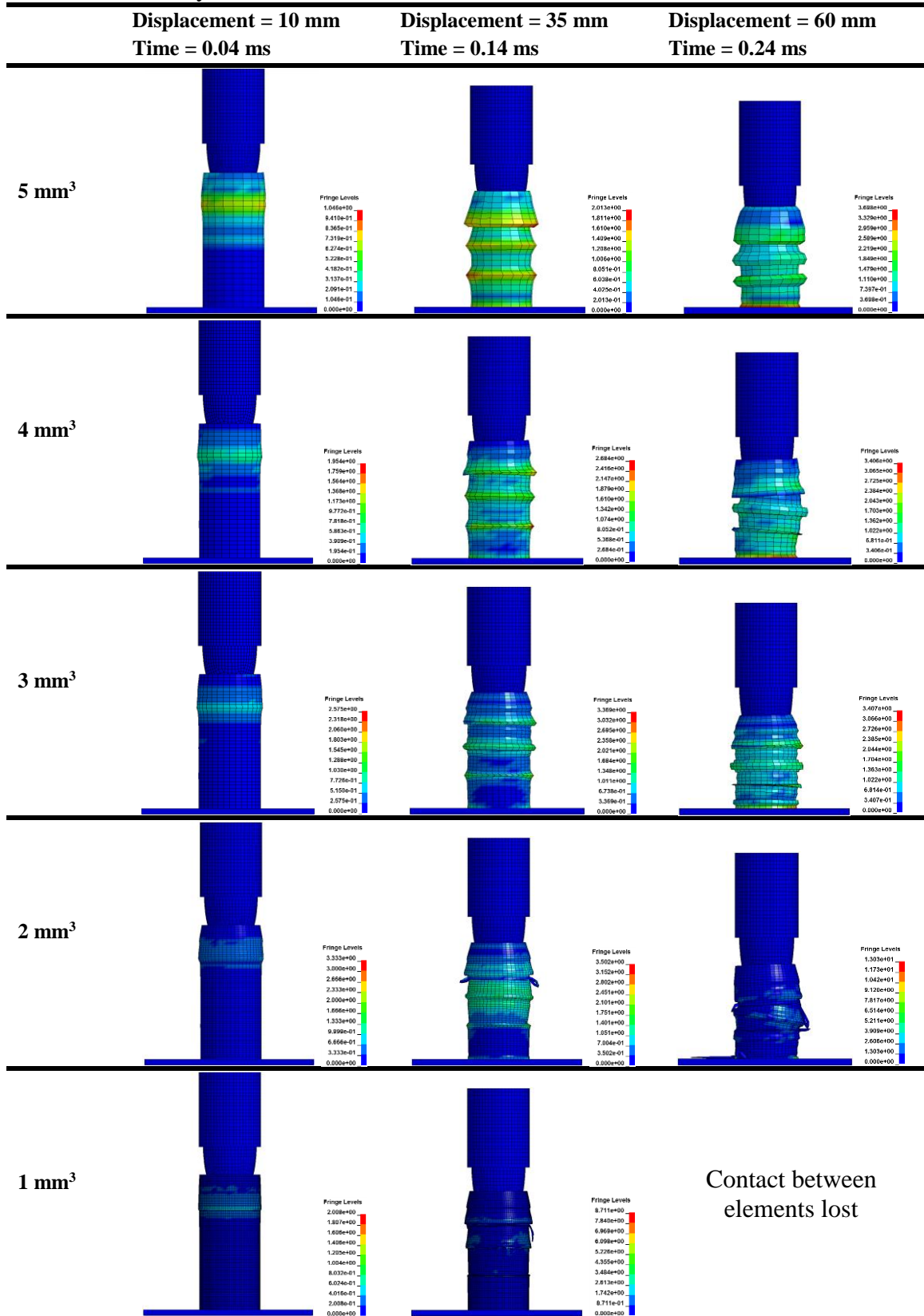
	Displacement = 10 mm Time = 0.04 ms	Displacement = 35 mm Time = 0.14 ms	Displacement = 60 mm Time = 0.24 ms
5 mm³			
4 mm³			
3 mm³			
2 mm³			
1 mm³			Contact between elements lost

Table D.3: Parametric study for the failure modelling parameters in MAT_054

Parameter	Baseline value	Parametric variation
SOFT	0.95	0.5, 0.7, 0.9, 0.95, 1
FBRT	0.9	0.5, 0.8, 0.9, 1
YCFAC	6	0, 2, 4, 6, 7
SLIM (T1, T2, C1, C2, S)	1	0.1, 0.5, 0.9, 0.95, 1
PEL	0	0, 0.5, 1
DFAILT	0.10	0, 0.01, 0.05, 0.10, 0.20
DFAILC	-0.10	0, -0.01, -0.05, -0.10, -0.20
DFAILM	0	0, 0.01, 0.05, 0.10, 0.20
DFAILS	0	0, 0.01, 0.05, 0.10, 0.20
ALPH	0.1	0, 0.10, 0.50, 1
BETA	0.5	0, 0.10, 0.50, 1

SOFT

SOFT is a strength reduction parameter used in crushing simulations. The strength reduction of the material follows Equation (3.10). SOFT ranges between 0 and 1. In MAT_054 SOFT has a default value = 1, that means no reduction in strength values. In this parametric study 5 values for SOFT have been studied; 0.5, 0.7, 0.9, 0.95, 1. Results showed that there are no big differences between the curves especially at the begging of loading, as shown in Figure D.1, thus SOFT will be turned off for both CFRP and KFRP, by setting the value = 1, so there is no strength reduction.

(a) CFRP BGP   (b) KFRP BGP
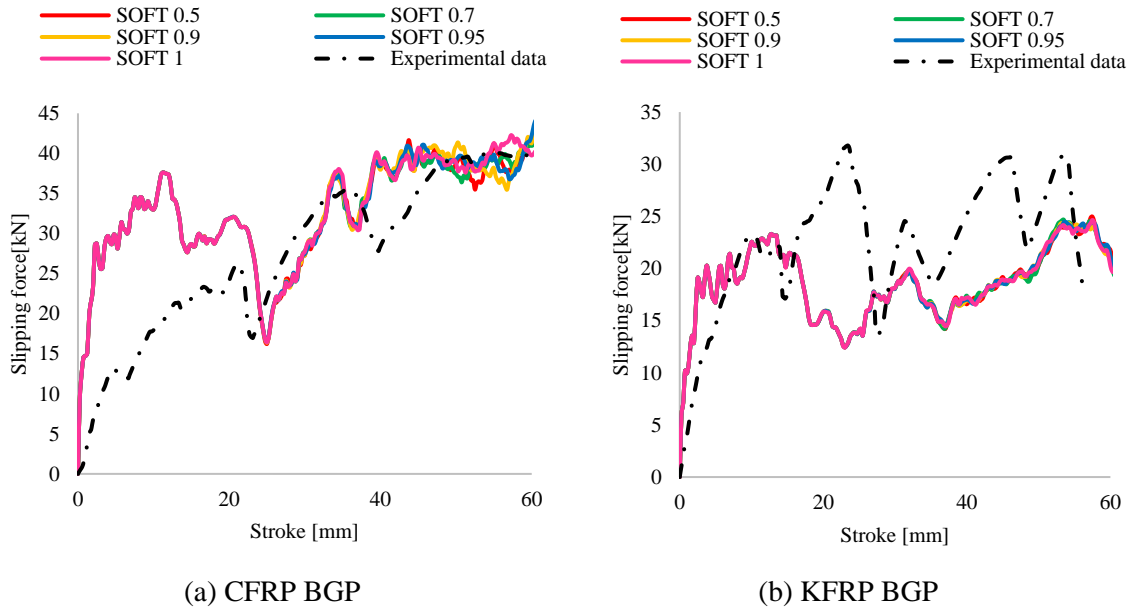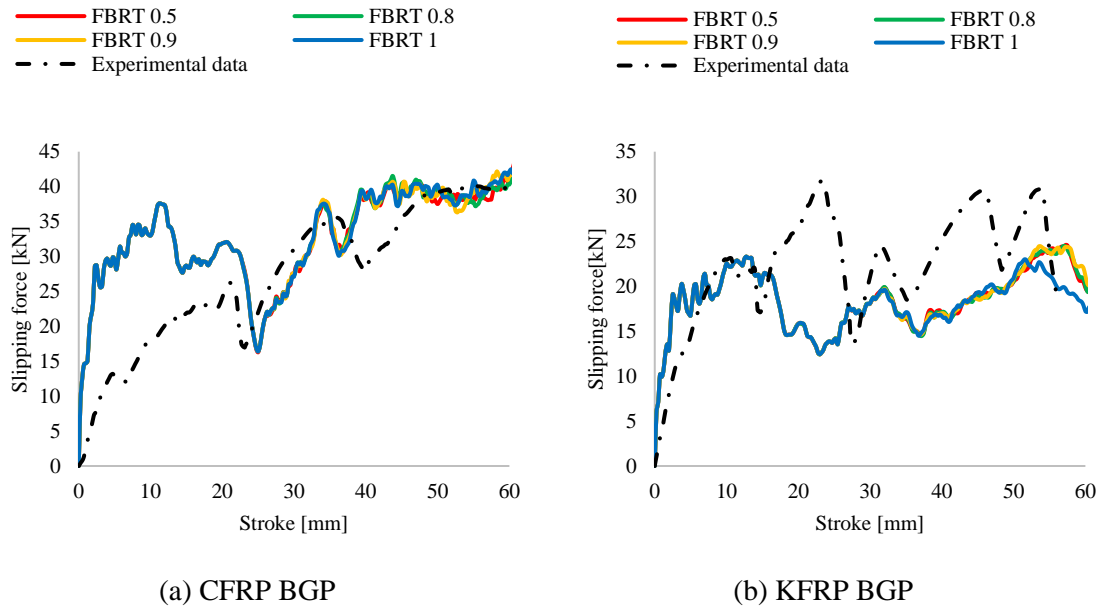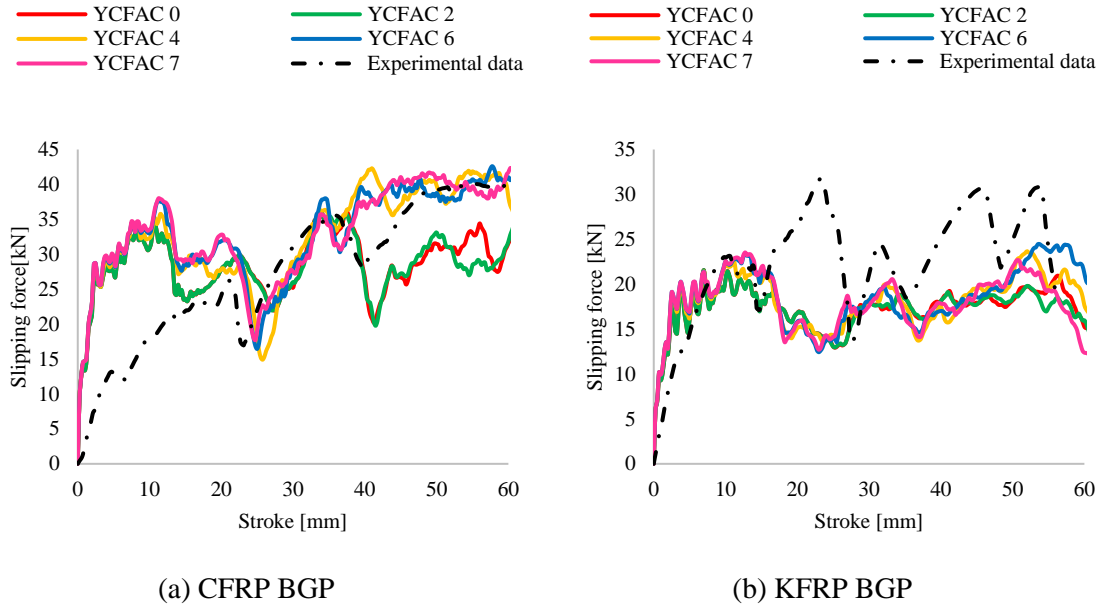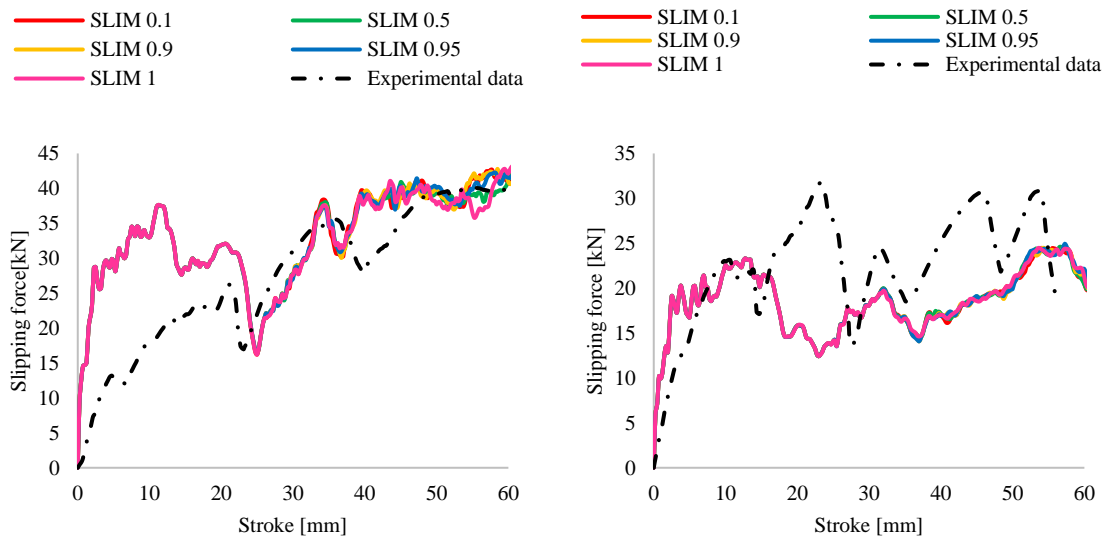
Figure D.1: Parametric study for different SOFT values by comparing Slipping force-stroke curves with the experimental data for the BGP.

FBRT

FBRT is a tension fiber strength reduction parameter used in crushing simulations, after failure occurs in compressive matrix mode, to degrade the original fiber strength. FBRT follows Equation (3.8) and ranges between 0 and 1 with a default value = 0. In this parametric study 4 values for FBRT have been studied; 0.5, 0.8, 0.9, 1. Results showed that there are no big differences between the curves, as shown in Figure D.2, thus a 0.9 value of FBRT will be considered in the CFRP FEM and a 1 value of FBRT for KFRP bullet guiding pockets.
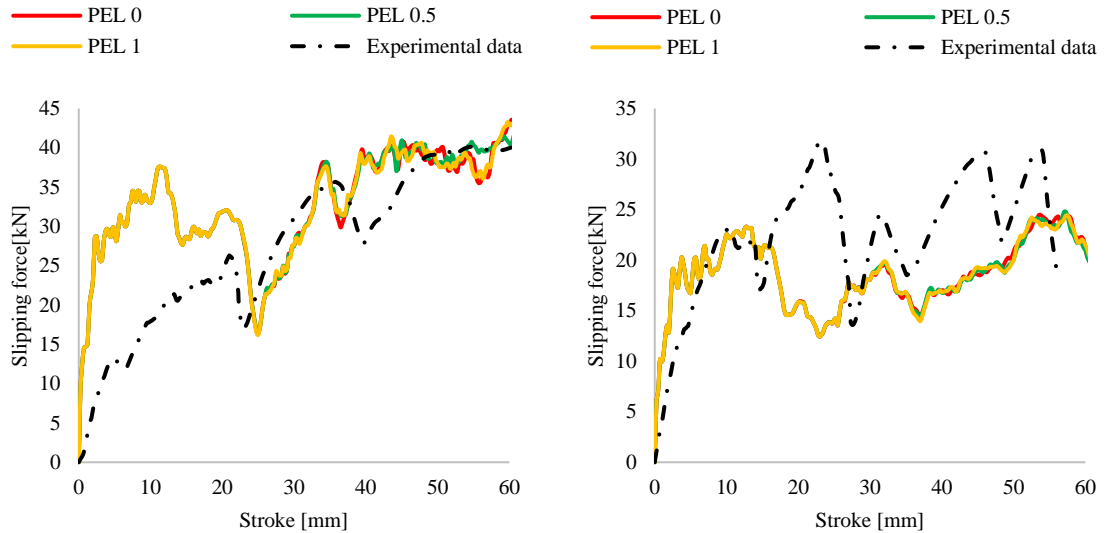

(a) CFRP BGP   (b) KFRP BGP

Figure D.2: Parametric study for different FBRT values by comparing Slipping force-stroke curves with the experimental data for the BGP.

YCFAC

YCFAC is a compressive fiber strength reduction parameter used in crushing simulations, after failure occurs in compressive matrix mode, to degrade the original fiber strength. YCFAC follows Equation (3.9) and has a default value = 2. In this parametric study 5 values for YCFAC have been studied; 0, 2, 4, 6, 7. Results showed that YCFAC plays a big role on the system as shown in Figure D.3. A 70% of fiber compression strength reduction showed a good agreement with the experimental data in CFRP and KFRP bullet guiding pockets.

| (a) CFRP BGP | (b) KFRP BGP |

Figure D.3: Parametric study for different YCFAC values by comparing slipping force-stroke curves with the experimental data for the BGP.

Residual stresses (SLIMC1, SLIMC2, SLIMT1, SLIMT2, SLIMS)

SLIMC1, SLIMC2, SLIMT1, SLIMT2, SLIMS are the residual stresses for different directions. These parameters are active after the maximum stress occurred in fiber or matrix compression and tension. In this parametric study, these parameters were changed all at once using 5 different values; 0.1, 0.5, 0.9, 0.95, 1. Results are shown in Figure D.4. A value of 0.95 SLIM will be considered for the CFRP FEM and 1 for KFRP FEM.
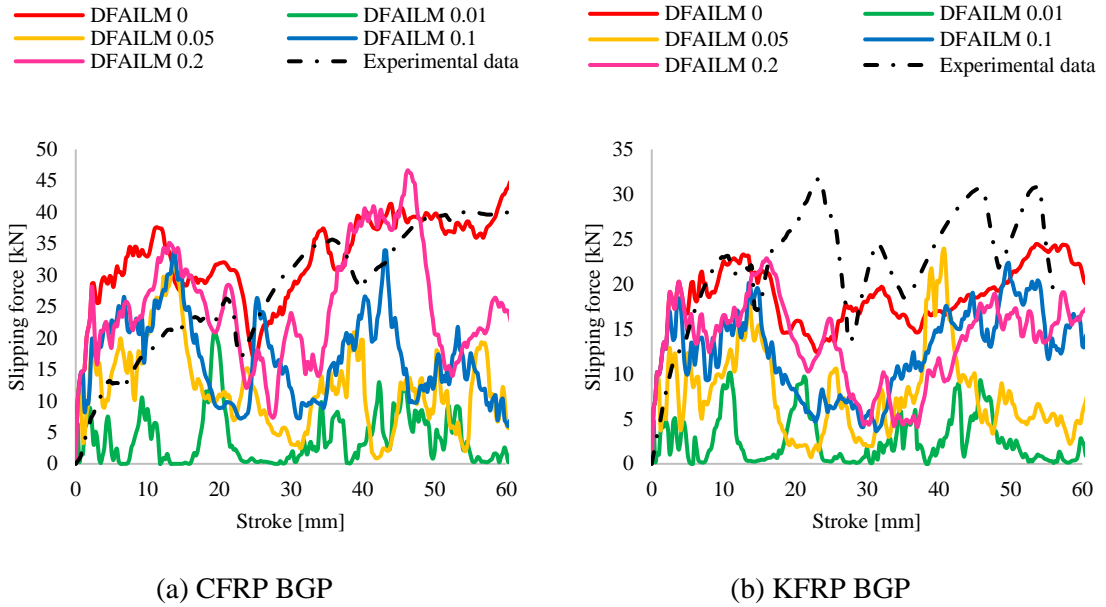
Figure D.4: Parametric study for different residual stresses values by comparing slipping force-stroke curves with the experimental data for the BGP.

PEL

PEL parameter is used to determine the layers needed to fail until the crushing is initiated. It ranges between 0 and 1. A value of 1 means that there is no reduction in the strength of the neighboring elements, thus no plies deletion. Results in Figure D.5 show no big effect in layers' deletion, this may refer to the continuous filament of the wound carbon fiber or Kevlar. A value of 0 will be used in both CFRP and KFRP FEMs.

(a) CFRP BGP   (b) KFRP BGP

Figure D.5: Parametric study for different PEL values by comparing slipping force-stroke curves with the experimental data for the BGP.

DFAILM

DFAILM is the maximum strain for matrix straining in both tension and compression. A low strain value will give low energy in the system, while by increasing the strain value will increase the energy response also. For DFAILM parameter, five different values were studied; 0, 0.01, 0.05, 0.1, 0.2 as shown in Figure D.6. Results showed that any non-zero value for DFAILM gives a catastrophic failure. This may refer to the low matrix ratio in both systems. A value of 0 was set to both CFRP and KFRP FEMs.

(a) CFRP BGP   (b) KFRP BGP

Figure D.6: Parametric study for different DFAILM values by comparing Slipping force-stroke curves with the experimental data for the BGP.

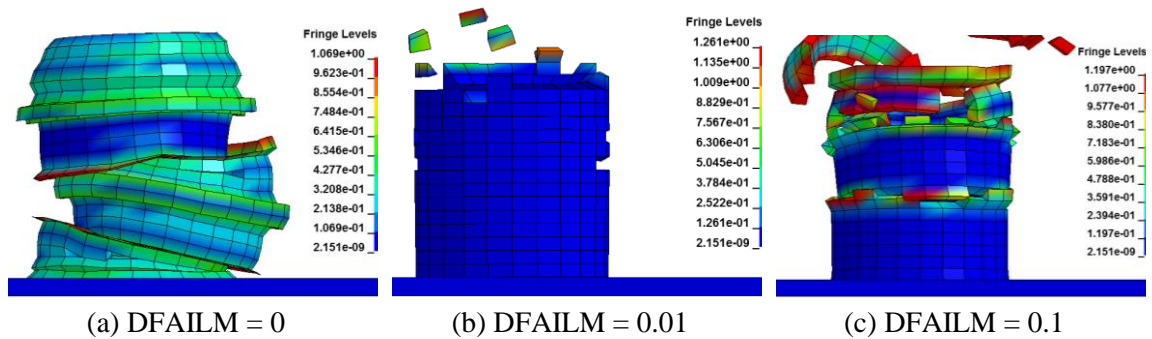(a) DFAILM = 0   (b) DFAILM = 0.01   (c) DFAILM = 0.1

Figure D.7: DFAILM effect on the crushing behavior of the CFRP BGP.

DFAILS

DFAILM is the maximum tensorial shear strain. A low strain value will give low energy in the system, while by increasing the strain value will increase the energy response also. For DFAILS 5 different values were studied; 0, 0.01, 0.05, 0.1, 0.2 as shown in Figure D.8. Results showed that any non-zero value for DFAILS gives a catastrophic failure. A value of 0 was set to both CFRP and KFRP FEMs.

(a) CFRP BGP   (b) KFRP BGP
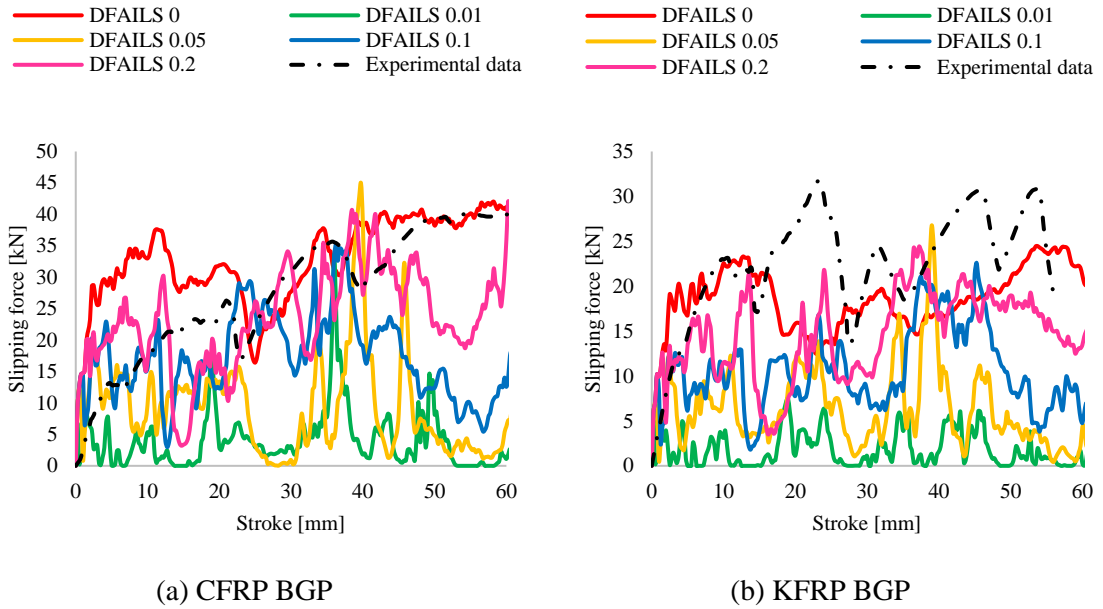
Figure D.8: Parametric study for different DFAILS values by comparing slipping force-stroke curves with the experimental data for BGP.


(a) DFAILS = 0   (b) DFAILS = 0.01   (c) DFAILS = 0.1
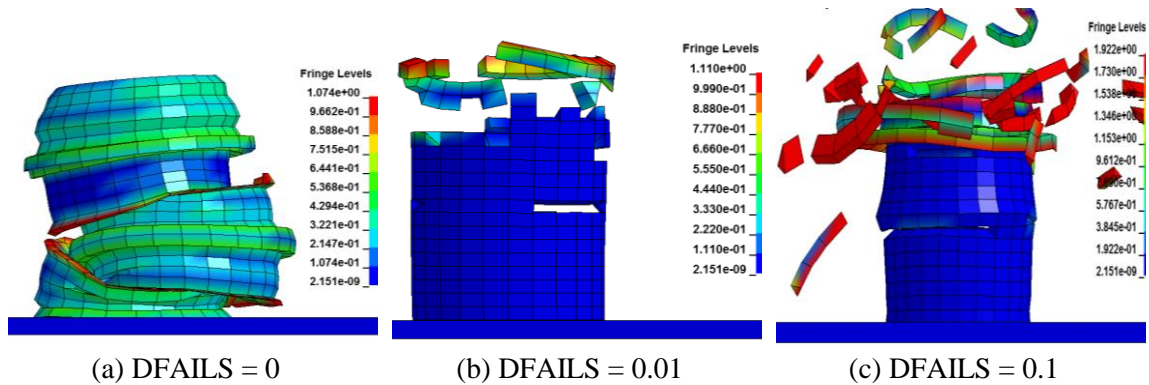
Figure D.9: DFAILS effect on the crushing behavior of the CFRP BGP.

DFAILT

DFAILT is the maximum strain for fiber tension. DFAILT ranges between 0 and 1. In this parametric study, 5 different values were studied; 0, 0.01, 0.05, 0.1, 0.2 as shown in Figure D.10. Results showed that there is no big difference between the values. A value of 0.1 was set to both CFRP and KFRP FEMs.
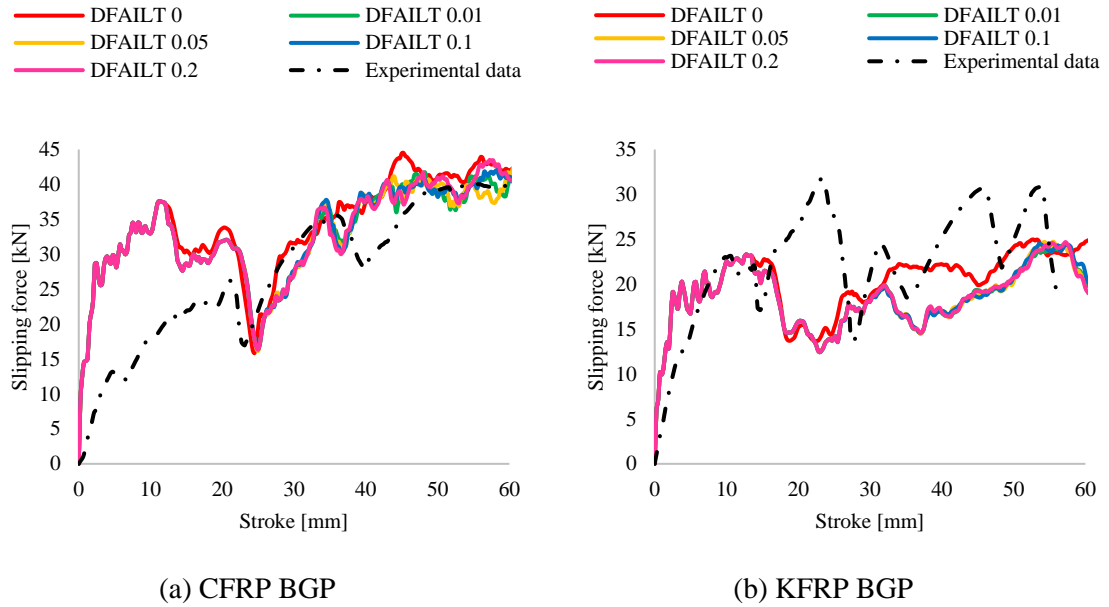
(a) CFRP BGP

(b) KFRP BGP

Figure D.10: Parametric study for different DFAILT values by comparing slipping force-stroke curves with the experimental data for the BGP.


(a) DFAILT =0

(b) DFAILT =0.1
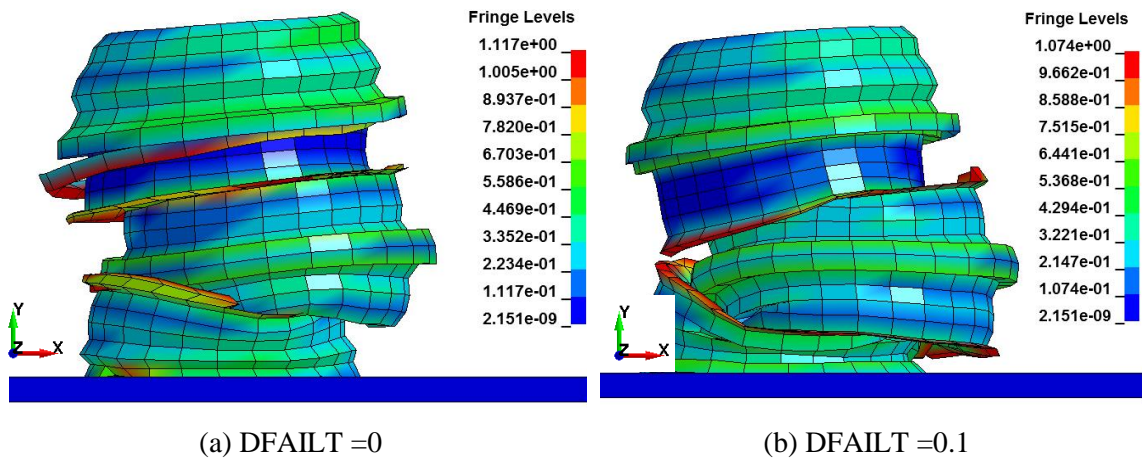
Figure D.11: DFAILT effect on the crushing behavior of CFRP BGP.

DFAILC

DFAILC is the maximum strain for fiber compression. DFAILC ranges between 0 and 1. In this parametric study, 5 different values were studied; 0, -0.01, -0.05, -0.1, -0.2. By setting DFAILC = 0, this parameter will be turned off and the whole model will be failed as shown in Figure D.12. A value of -0.1 was set to the CFRP FEM, and -0.2 to the KFRP FEM.
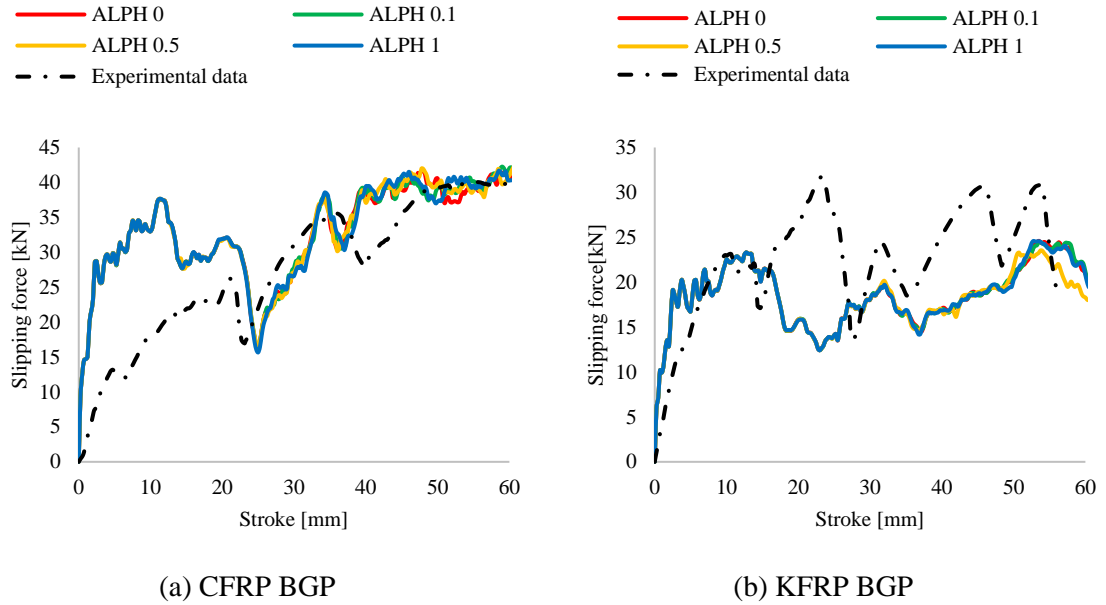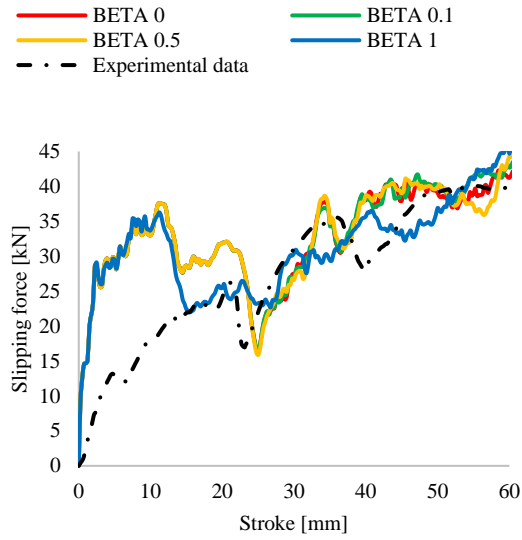
159
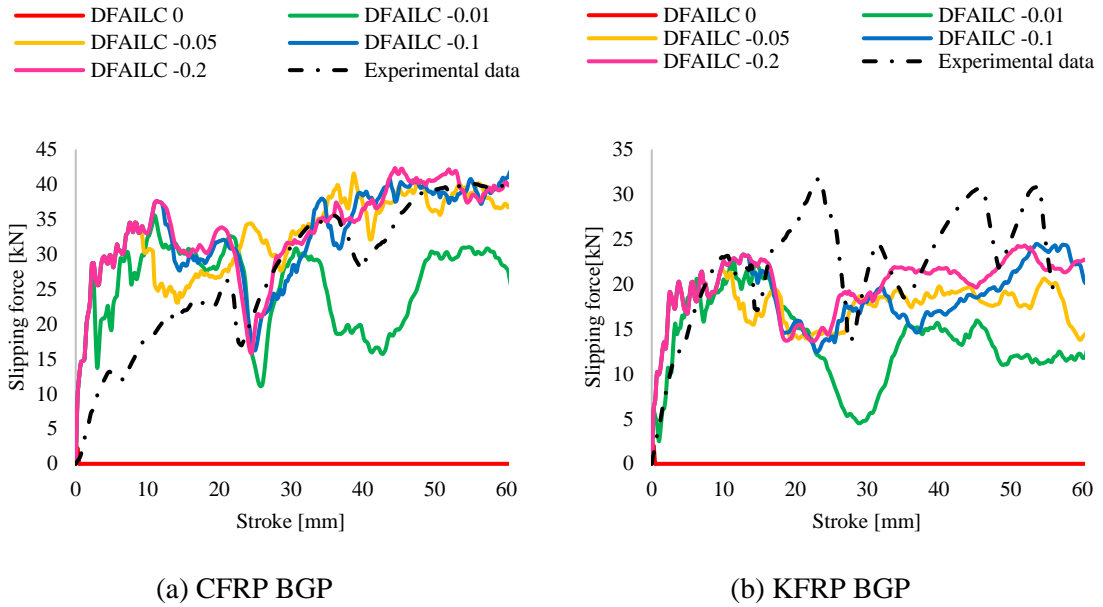
(a) CFRP BGP

(b) KFRP BGP

Figure D.12: Parametric study for different DFAILC values by comparing slipping force-stroke curves with the experimental data for the BGP.

(a) DFAILC = 0

(b) DFAILC = -0.01

(c) DFAILC = -0.1
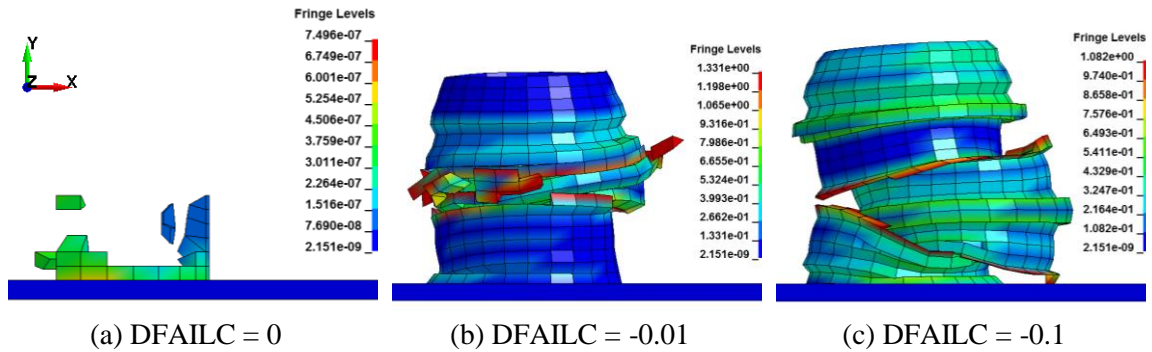
Figure D.13: DFAILC effect on the crushing behavior of CFRP BGP; most of the elements are deleted.

ALPH

ALPH is a weighting factor for non-linear shear stress terms. ALPH follows Equation 3.7) and ranges between 0 and 1. In this parametric study, 4 different values were studied; 0, 0.1, 0.5, 1 as shown in Figure D.14. Results showed that ALPH has no big effect in the model as shearing does not play a big role in this system. A value of 0.1 will be set for both CFRP and KFRP ALPH parameters.
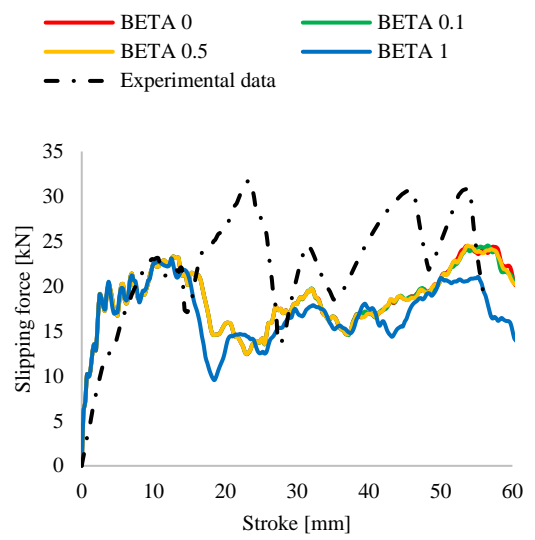
(a) CFRP BGP   (b) KFRP BGP

Figure D.14: Parametric study for different ALPH values by comparing Slipping force- stroke curves with the experimental data for BGP.

BETA

BETA is a weighing factor for shear term in tensile fiber mode. BETA follows Equation (2.14) and ranges between 0 and 1. If BETA = 1, Hashin failure criteria [110] will be activated. If BETA = 0, Equation (2.14) will be reduced to the Maximum Stress failure criteria. In this parametric study, 4 different values were studied; 0, 0.1, 0.5, 1 as shown in Figure D.15. Results showed that when BETA = 1, the behavior of the model differs from the other values, otherwise BETA has no big effect on the model, as the tensile stresses have less effect on the results than the compressive stresses in this FEM. A value of 0.1 will be set for both CFRP and KFRP BETA parameters.

(a) CFRP BGP   (b) KFRP BGP

Figure D.15: Parametric study for different BETA values by comparing Slipping force- stroke curves with the experimental data for BGP.

APPENDIX E

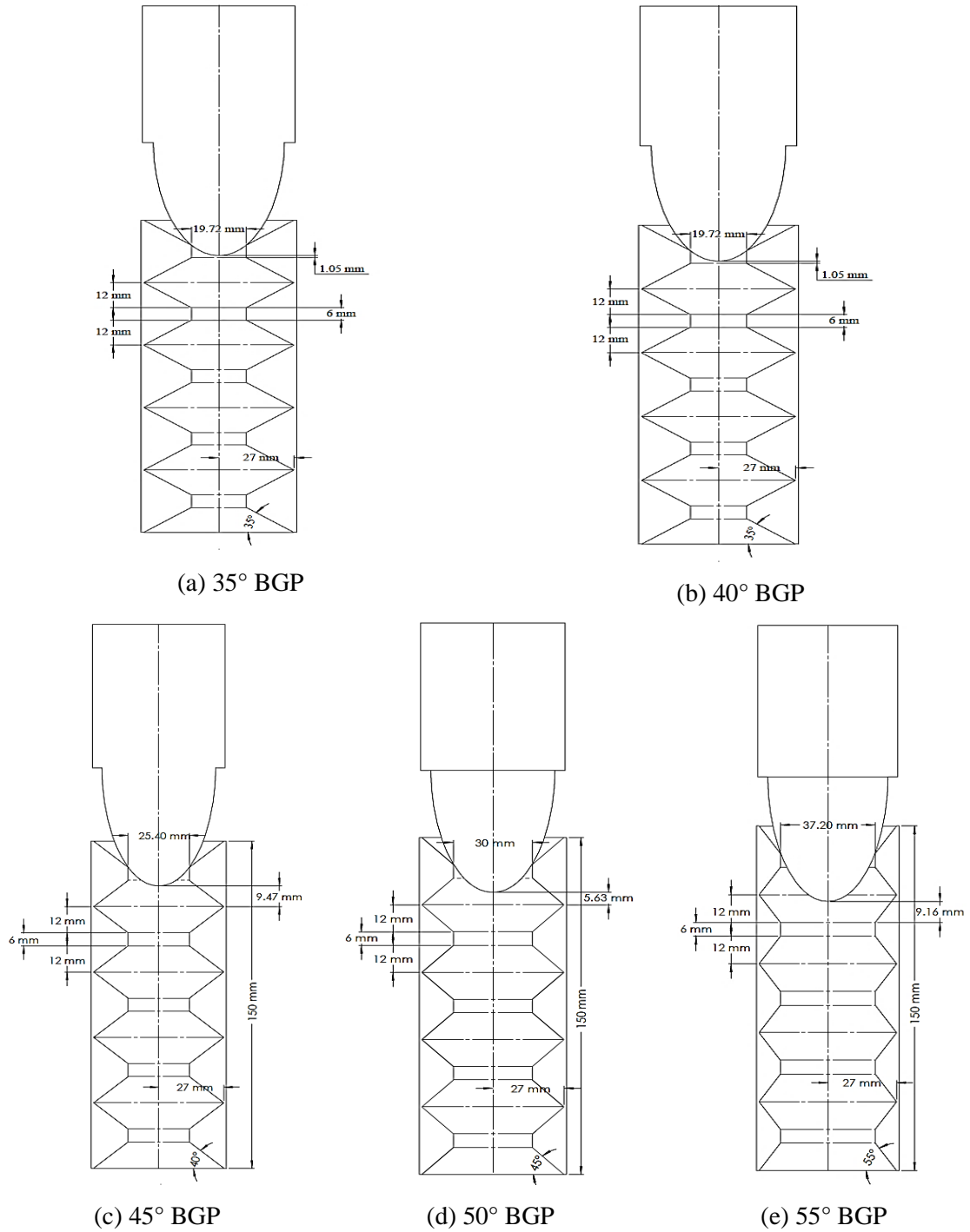# DIMENSIONS OF THE BULLET GUIDING POCKETS

(a) 35° BGP

(b) 40° BGP

(c) 45° BGP

(d) 50° BGP

(e) 55° BGP

Figure E.1: Dimensions for the bullet guiding pockets penetrated by the impactor, front section view
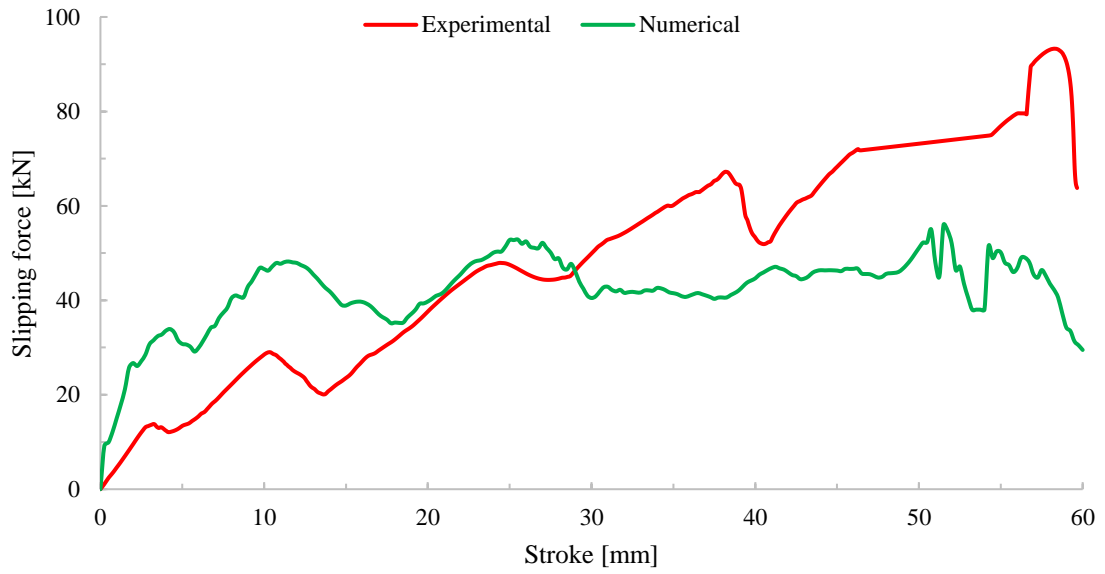
APPENDIX F

SLIPPING FORCE-STROKE CURVES

Figure F.1: Experimental and numerical slipping force-stroke curves of 35° CFRP BGP
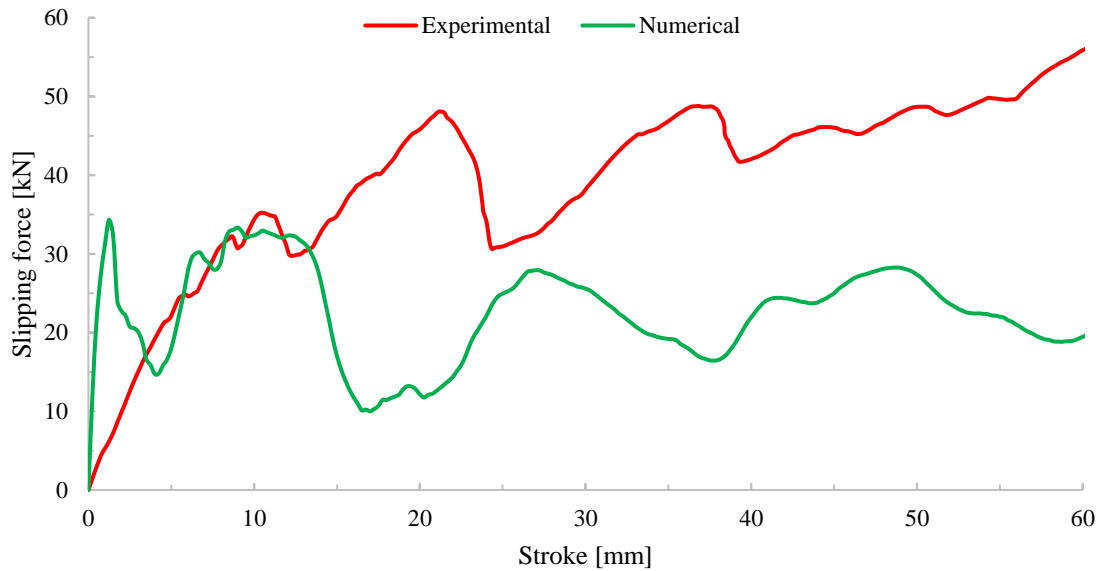

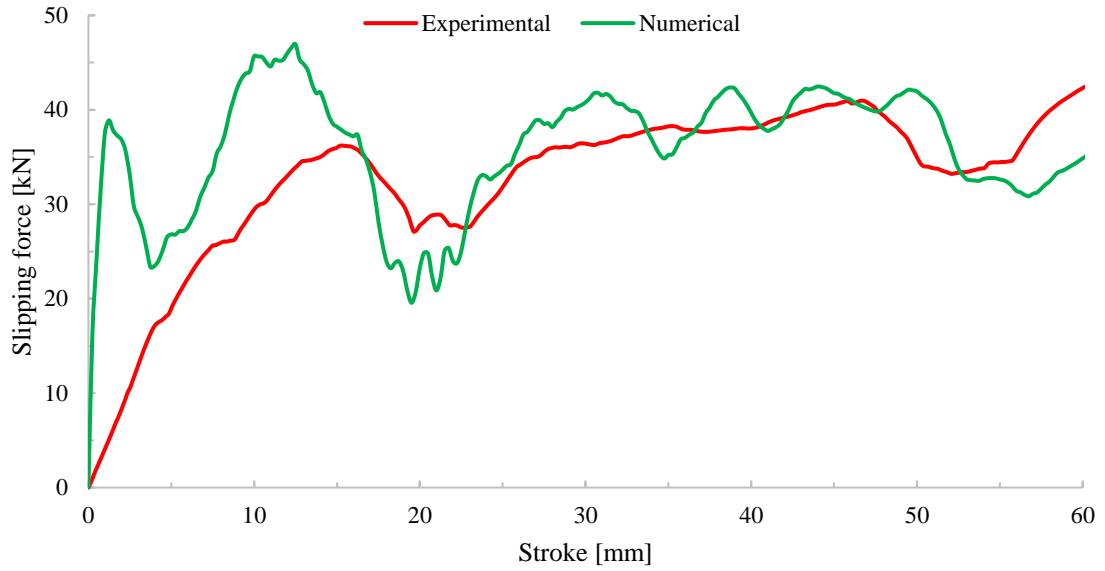Figure F.2: Experimental and numerical slipping force-stroke curves of 50° CFRP BGP

Figure F.3: Experimental and numerical slipping force-stroke curves of 55° CFRP BGP
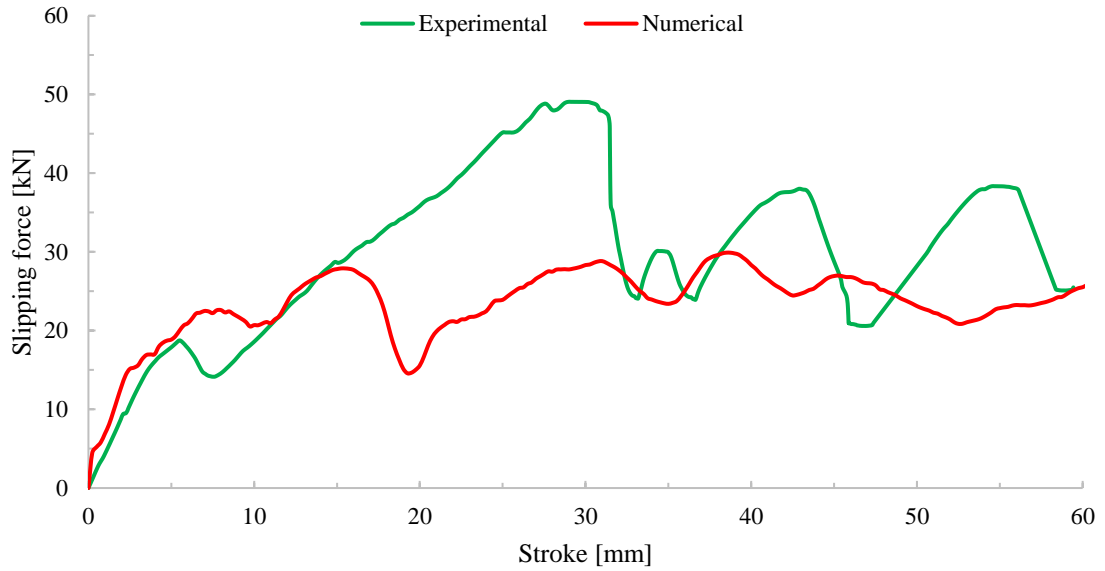

Figure F.4: Experimental and numerical slipping force-stroke curves of 40° KFRP BGP
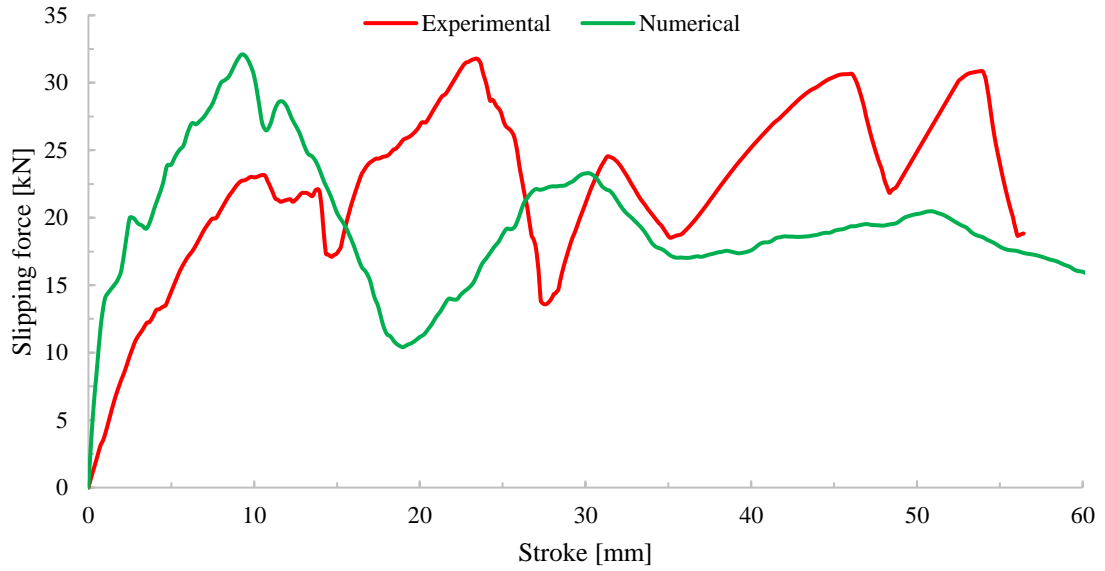
Figure F.5: Experimental and numerical slipping force-stroke curves of 45° KFRP BGP
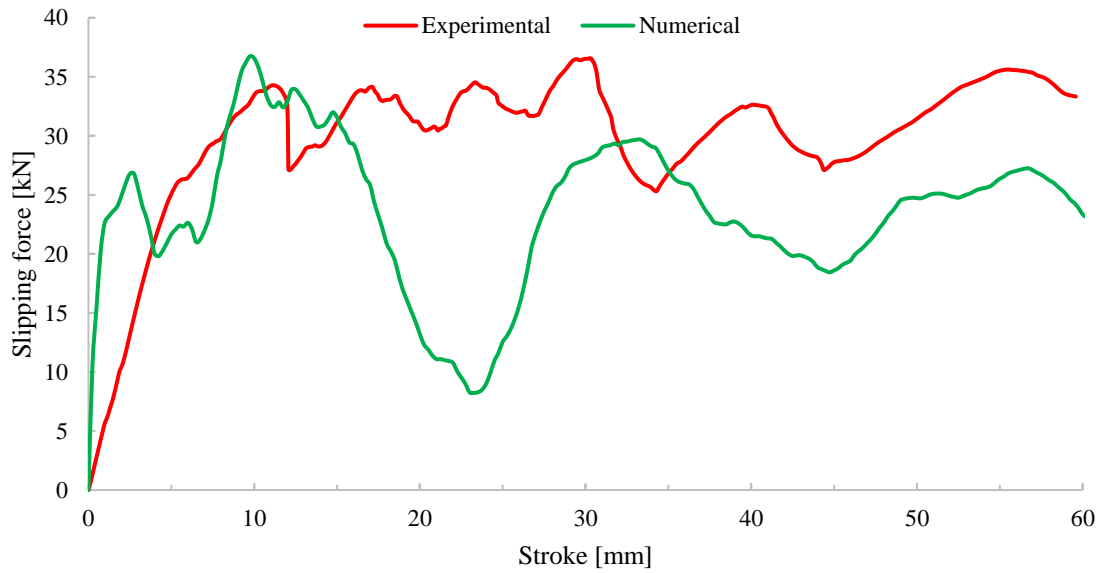

Figure F.6: Experimental and numerical slipping force-stroke curves of 50° KFRP BGP

APPENDIX G
NIJ STANDARD

Armor Type	Test Round	Test Bullet	Bullet Mass	Conditioned Armor Test Velocity	New Armor Test Velocity	Hits per Panel at 0°	BFS Depth Maximum	Hits per Panel at 30° or 45°	Shots per Panel	Panel Size	Panel Condition	Panels Req'd	Shots Req'd	Total Shots Req'd
IIA	1	9 mm FMJ RN	8.0g (124gr)	355m/s (1165ft/s)	373 m/s (1225 ft/s)	4	44 mm (1.73 in)	2	6	Large Small	New Condition	4 2 4 2	24 12 24 12	144
	2	.40 S&W FMJ	11.7g (180gr)	325m/s (1056ft/s)	352 m/s (1155 ft/s)	4	44 mm (1.73 in)	2	6	Large Small	New Condition	4 2 4 2	24 12 24 12	
II	1	9 mm FMJ RN	8.0g (124gr)	379m/s (1245ft/s)	398 m/s (1305 ft/s)	4	44 mm (1.73 in)	2	6	Large Small	New Condition	4 2 4 2	24 12 24 12	144
	2	.357 Mag JSP	10.2g (158gr)	408m/s (1340ft/s)	436 m/s (1430 ft/s)	4	44 mm (1.73 in)	2	6	Large Small	New Condition	4 2 4 2	24 12 24 12	
IIIA	1	.357 SIG FMJ FN	8.1g (124gr)	430m/s (1410ft/s)	448 m/s (1470 ft/s)	4	44 mm (1.73 in)	2	6	Large Small	New Condition	4 2 4 2	24 12 24 12	144
	2	.44 Mag SJHP	15.6g (240gr)	408m/s (1340ft/s)	436 m/s (1430 ft/s)	4	44 mm (1.73 in)	2	6	Large Small	New Condition	4 2 4 2	24 12 24 12	
III	1	7.62 mm NATO FMJ	9.6g (147gr)	847m/s (2780ft/s)	-	6	44 mm (1.73 in)	0	6	All	Conditioned	4	24	24
IV	1	.30 caliber M2 AP	10.8g (166gr)	878m/s (2880ft/s)	-	1	44 mm (1.73 in)	0	1 to 6	All	Conditioned	4 to 24	24	24
Special	*	Each test threat to be specified by armor manufacturer or procuring organization				Armor performance and shot requirements shall depend on armor type								